A Novel 3D Printed Brace Manufacturing Process for the Treatment of Adolescent Idiopathic Scoliosis

by

Kenwick Jiu Lam Ng

A thesis submitted in partial fulfillment of the requirements for the degree of

Master of Science

in

Biomedical Engineering

Department of Biomedical Engineering
University of Alberta

Abstract

Adolescent Idiopathic Scoliosis (AIS) is a three-dimensional spinal deformity with lateral curvature and axial vertebral rotation affecting 1-3% of adolescents. Bracing is a proven non-surgical treatment aiming to stop curve progression. Literature has shown that brace wear time affects brace effectiveness. However, the current structure of a brace can be bulky, lack ventilation, and cumbersome to manufacture which affects patients' compliance. The motivation of this research is that a more comfortable, and effective brace can be manufactured with 3D printing and scanning technologies at reduced cost and labour effort. The objectives of this research are to investigate appropriate 3D printing parameters, to design and evaluate dynamic brace pads and brace casting frame, to investigate the 3D scanned torso accuracy and precision, to design a new brace manufacturing process and to evaluate the 3D printed brace effectiveness and manufacturing process.

To determine the appropriate parameters for printing a brace, experiments were conducted to compare the mechanical properties of 31 test specimens that were 2.5 mm, 3.25 mm, and 4 mm thick with ULTEM1010, Nylon12, and polypropylene material. Fused deposition modelling (FDM) method, Nylon12 material, and 2.5-3.25 mm thickness were found to be the appropriate printing parameters with high flexibility, as well as adequate strength and ductility. To validate durability of a brace with the recommended printing parameters, manual simulation of prototype brace wear with donning and doffing was conducted. The FDM, Nylon12, 2.5 mm thick, and upright printed prototype brace showed retention of structural integrity with 2 years brace wear simulation.

To understand the pressures applied by orthotists to obtain the satisfactory simulated in-brace body contour, airtight dynamic brace pads were designed. The dynamic brace pads

were integrated with a brace casting frame so that 3D corrective forces could be applied to patients' torso during brace design clinic. The completed system was evaluated with a healthy volunteer to ensure both the dynamic brace pads and the brace casting frame met design specifications before using it at the clinic.

Patient's torso was captured while standing in the casting frame. As a specific 3D scanner was chosen, its accuracy and precision in capturing torso contour were investigated prior to application in clinics. Experiments were conducted by scanning different body mold dimensions at different scan ranges. Furthermore, the 3D reconstruction accuracy at pad covered torso regions were evaluated based on deviation between scan without pads applied and scan with reconstructed pad regions. The results showed that the scanned torso accuracy and precision were within 1 cm clinical accepted range, but the reconstruction accuracy slightly exceeded 1 cm. A subjective modification on the pad covered regions might be needed by the orthotist. To construct a 3D printed spinal brace based on the results described above, a new 3D printed brace manufacturing process was developed. This process began with the orthotist adjusting the brace frame pad placement and applied pressure on patient torso to obtain satisfactory in-brace pad configuration based on real-time ultrasound and pressure measurements. Patient's torso was then scanned, modified and sent for 3D printing.

Lastly, to investigate the 3D printed brace effectiveness, a randomized controlled trial (RCT) was conducted to compare the immediate in-brace corrections at the first follow-up clinic of patients with the traditional and 3D printed brace. Currently, four patients were recruited with two patients at each study arm. For the 3D printed brace group, the in-brace Cobb angle correction of 3/4 treated curves reached clinical aimed threshold of 50%

correction. The 3D printed brace was also 30% thinner, 26% lighter, and requiring 4.5 times less labour time than the traditional brace. However, it is 27% more expensive in cost because the 3D printed brace was printed from external source while the traditional brace was built in-house.

In conclusion, this thesis reports a new design of dynamic brace pads which were implemented into a novel 3D printed brace manufacturing process to create thinner, lighter, lower labor cost and at least similar in-brace effectiveness 3D printed braces for the future generation of brace treatment for children with AIS.

Preface

The research described in this thesis had received ethics approval from the Health Research Ethics Board from the University of Alberta. The project name is "A New Spinal Brace Design Concept for the Treatment of Adolescents Idiopathic Scoliosis (AIS)", reference number: Pro00054113.

Portions of the material in this thesis have been submitted or published in the following papers:

- K. Ng, K. Duke, and E. Lou, "Evaluation of Mechanical Properties on Potential 3D Printed Materials for Spinal Braces," *Addit. Manuf.*, 2018 (Submitted).
  Some materials from this paper is reported in chapter 3. I conducted the literature review demonstrating a gap in the literature in the subject matter. Dr. Lou and Dr. Duke conceived the work described and provided technical advice. I performed the experiment and analysis of the data in this paper. I composed the manuscript with the assistance of Dr. Lou.

- K. Ng, E. Lou, and K. Duke, "Evaluation of accuracy, precision and optimal parameters of a 3D scanner in acquiring body contour of patients with adolescent idiopathic scoliosis," in *Scoliosis and Spinal Disorders*, 2018, vol. 13, p. 8.
  Some materials from this conference abstract is reported in chapter 5. I conceived and executed the work described in this abstract which included designing and performing the experiment as well as analyzing the data. I composed the manuscript with the assistance of Dr. Lou and Dr. Duke.

- An additional paper is expected to be composed from chapter 6. References of the above papers are reported as footnotes at the corresponding sections.

Acknowledgements

I would like to thank my supervisor, Dr. Lou for the opportunity to participate in this interesting field of research. Thank you for his patience and understanding throughout the two and a half years especially at the initial learning phase. I have learned valuable lessons from Dr. Lou not only academically but also with character and interaction with others. I would also like to thank my co-supervisor, Dr. Duke for her guidance, advice and support throughout the research work.

My mom and dad deserve much recognition and appreciation for their moral support and encouragement. They are always available when I need to chat, and they have been there for me in the ups and downs in research.

I am grateful for the friendships and fruitful discussions with my labmates Dr. Chan, Mahdieh Khodaei, Fraaz Kamal and others. I would like to acknowledge my labmates Dr. Chan, and Susanna Trac with their help in the design of the brace casting frame and especially thanking Dr. Chan for his insightful advices. I would also like to thank the researchers and staffs from the Glenrose Rehabilitation Hospital including Jim Raso, Doug Hill, Dr. Faulkner, and others for their support. As well, many thanks to the Edmonton Scoliosis Research Group for supporting the research work and patient recruitment including Andreas Donauer, Melissa Tilburn, and Kathleen Shearer just to name a few.

I would like to thank my cell group, church community for their prayers and support, my friend Dr. Chan, and Barnabus Wu for introducing me to the research work, and fellow graduate students including Anyeld Ubeda and McNiel-Inyani Keri for pushing each other in completing the thesis. I acknowledge and appreciate the funding support from the Women and Children's Health Research Institute (WCHRI), Queen Elizabeth II and Alberta Graduate Student Scholarship without which my research would not be possible.

Lastly, I acknowledge and thank the God of the Bible who created nature, which we observe in wonder for carrying me through the challenges in research.

Table of Contents

List of Tables

List of Figures

List of Abbreviations

AFO	Ankle Foot Orthosis
AIS	Adolescent Idiopathic Scoliosis
ANOVA	Analysis of Variance
ART	Asymmetric, Rigid, Torsion
ASIS	Anterior Superior Iliac Spine
ASTM	American Society of Testing and Materials
AVR	Axial Vertebral Rotation
CAD/CAM	Computer-Aided Design/Computer-Aided Manufacturing
CDC	Centers for Disease Control and Prevention
CFRP	Carbon Fiber Reinforced Plastic
COL	Center of Lamina Method
CT	Computed Tomography
CTLSO	Cervical-Thoracic-Lumbar-Sacral-Orthosis
EMCC	Estimate Maximum Curve Correction
FDM	Fused Deposition Modeling
FEA	Finite Element Analysis
GPS	Global Positioning System
MAD	Mean Absolute Difference
MIAS	Medical Image Analysis Software
MRI	Magnetic Resonance Imaging

IS	Idiopathic Scoliosis
LED	Light Emitting Diode
PA	Posterior-Anterior
PC	Polycarbonate
PE	Polyethylene
PLA	Polylactic Acid
PP	Polypropylene
PPMA	Poly (Methyl Methacrylate), Plexiglass
RCT	Randomized Controlled Trial
SLA	Stereo-Lithography
SLS	Selective Laser Sintering
SOSORT	Society on Scoliosis Orthopedic and Rehabilitation Treatment
SRS	Scoliosis Research Society
STL	Stereolithography
TLSO	Thoracic-Lumbar-Sacral-Orthosis
U/S	Ultrasound
UV	Ultraviolet
3D-P	Three-Dimensional Printing
3D	Three Dimensional

Chapter 1: Introduction

Scoliosis is a three dimensional spinal deformity consists of a lateral curvature and axial vertebral rotation of the spine [1], [2]. Often, it can be identified as an S-shape curvature from radiography in the coronal plane. Cobb angle is the gold standard to measure and determine severity of scoliosis. Scoliosis is diagnosed when a Cobb angle of greater than 10 degrees is measured. Adolescent Idiopathic Scoliosis (AIS) is the most common type of scoliosis affecting 1-3 % of adolescent population between 10-17 years old [1], [3]. Idiopathic meaning that the deformity has unknown cause. Untreated scoliosis results in permanent deformity, self-image and quality of life concerns [1], [3]. Sometimes, it can also lead to back pain and in severe cases cardiopulmonary problems [3]–[6]. Girls are seven to eight times more likely to have scoliosis progressing to a larger curvature [7].

Spinal bracing is a gold standard and proven non-surgical treatment for children with adolescent idiopathic scoliosis [8]. Bracing is prescribed for patient with moderate curvature (Cobb angle of 25-40 degrees) at initial diagnosis, high risk of curve progression as well as those with longer skeletal growth remaining [9]–[11]. Prescribed brace wear can range from night time only to full time which is up to 23 hours per day [8]. A spinal brace is a rigid plastic jacket customized to patient's body shape typically made of thermoplastic such as polypropylene with a thickness of 4 to 5 mm. The brace has multiple pressure pads to apply loads upon the torso to counteract the scoliotic curves when the brace is tightened with straps. The mechanical loading applied to the torso aims to stop curve progression during the rapid growth spurt of adolescence. The effectiveness of brace treatment is dependent on risk of curve progression, in-brace correction and compliance with wearing the brace with adequate tightness as well as wearing it to prescribed time [8], [10], [12], [13].

However, compliance of brace wear is an issue [14] because current braces are bulky, uncomfortable and noticeable which leads to decreased compliance that directly affects treatment outcome. A randomized control trial study with 116 patients recruited had shown that the average brace patient wear their braces only 67% of prescribed time [8]. Another study with 40 patients recruited showed an average of 55% of wear time within prescribed

tightness range determined by the orthotist [13]. Furthermore, the conventional brace design process can be cumbersome, time consuming and costly for both the patient and the orthotist. Currently, multiple steps are required to manufacture the final brace. The manufacturing process may require plaster wrapping a patient to obtain a negative body mold or the computer-aided design/computer-aided manufacturing (CAD/CAM) method that obtains a patient's body shape by a 3D scanner or camera system. The body shape file is then exported to a computer and go through multiple manufacturing steps to create a brace [14], [15]. The entire manufacturing and fitting process may take a while from prescription to completion. Since the risk of curve progression is an uncontrollable inherit factor, this research project is focused on finding ways to improve quantity (wear time) of compliance.

With the rapid advancement of 3D printing technologies, applications in the clinical setting can create positive changes in the health care sector. A CAD/CAM system can create a 3D printed brace directly by capturing a shape and sending the output stereolithography (STL) file to a 3D printer. Currently, there are some companies who had begun development of 3D printed braces for treating AIS with this CAD/CAM approach. Nevertheless, there is no scientific evidence or literature to justify selection of brace design parameters or report treatment effectiveness of these 3D printed braces. This new approach provides a novel solution that is economical, reduces manufacturing steps, less labour intensive and it also has the potential to reduce time from prescription to patient getting a brace. Also, a 3D printed brace might be more effective than traditional polypropylene brace for treatment of Adolescent Idiopathic Scoliosis (AIS).

1.1. Motivation for a 3D Printed Spinal Brace

The hypothesis for this research is that a 3D printed brace will be more comfortable therefore increasing wear time compliance which leads to more effective treatment. A 3D printed brace can be created thinner, lighter, and more breathable with addition of voids. Therefore, a spinal brace can be less noticeable, more comfortable and increasing compliance to prescribed wear time. The new brace casting and manufacturing process with 3D spinal correction, real time ultrasound and pressure measurements can also provide a more effective treatment of AIS.

Traditionally, applications in 3D printing had been primarily used for rapid prototyping before a final design is completed. However, with the advancement of 3D printing technology, it has transformed to being used as a new additive manufacturing method in creating functional parts. The advantage of 3D printing includes not requiring specialized tools, dies and molds. Also, it is especially cost effective for creating customized parts compared with existing manufacturing methods. In the biomedical field, applications of 3D printing include assisting bone healing with printed bone tissue scaffold for patient with fractured or diseased bone structures, hearing aid, anatomical models for surgical preparation, pharmaceutical drug delivery, foot orthoses and ankle/foot orthoses. For this research study, a customized 3D printed brace will be used by AIS patients with moderate spinal curvatures for typically 2-3 years until significant physical growth. Adolescent patients can go through full time wear of two or even three braces until skeletally maturity.

1.2. Objectives

The objectives of this research are:

1. To investigate the appropriate 3D printed method, orientation, material, and thickness for a spinal brace
2. To design and evaluate dynamic brace pads and brace casting frame for pressure measurement and 3D correction brace design, respectively
3. To study the accuracy and precision in acquiring patient torso geometry using a handheld 3D scanner
4. To develop a new brace casting and manufacturing process for a 3D printed spinal brace
5. To investigate the effectiveness of 3D printed brace with clinical study and evaluating the 3D printed brace manufacturing process

1.3. Scope of Work

Literature review on the background of scoliosis, brace types and biomechanical theory, current brace manufacturing, factors affecting brace effectiveness and brace material were needed to better understand the challenges at hand in treating scoliosis deformity with current brace design. Following that, literature on 3D printing and technologies to obtain

body shape needed to be explored to gather information on available tools and techniques for developing a 3D printed brace. Next, the scope of work included investigating appropriate 3D printing parameters for creating a spinal brace, evaluating and validating the durability of prototype 3D printed spinal braces. After that, the design and evaluation of airtightness and expansion of dynamic brace pads were needed before implementation in clinic. The design and evaluation of brace casting frame that would provide multi-degree of freedom for brace pads adjustment were also needed before implementation in clinic. Another major component for developing a 3D printed brace is acquiring patient body shape accurately and consistently. Therefore, the scope of work included investigation of the 3D scanned torso accuracy and precision with different torso dimensions and scan distance ranges. Furthermore, investigation of scanned torso accuracy at brace pad regions was also included. Next, the design of a new 3D printed brace casting and manufacturing process was needed. Lastly, a clinical study would be conducted by comparing in-brace corrections of traditional and 3D printed braces to determine effectiveness of 3D printed brace. Manufacturing process parameters between the traditional brace and 3D printed brace would also be compared.

1.4. Thesis Overview

This thesis includes seven chapters. This chapter begins with the background, motivation, objectives, and scope of work of the research study. In the following chapters, a comprehensive literature review on the background of scoliosis, brace treatment, 3D printing and technologies for obtaining patient body shape are discussed. Next, the appropriate 3D printing parameters and evaluation of prototype 3D printed braces are described. Then, the design and evaluation of dynamic brace pads and custom brace fitting frame are discussed. After that, the accuracy and precision study of the 3D scanned torso are described. The new brace casting and manufacturing process are also reported. Lastly, an investigation on effectiveness of 3D printed brace through clinical study is reported and discussed.

Chapter 1 states the motivation in developing a 3D printed spinal brace and the potential in providing a more comfortable and effective treatment for patients. Furthermore, specific

objectives and scope of work of this research study are included along with this overview of thesis chapters.

Chapter 2 introduces the basic anatomy relating to scoliosis as well as comprehensive literature review about the background of scoliosis, various brace types and biomechanical theory, brace manufacturing, factors affecting brace effectiveness, brace materials, 3D printing technologies and existing technologies for obtaining body shape.

Chapter 3 describes the determination of 3D printing parameters such as 3D printing method, printer, and print orientation. Appropriate 3D printed material and thickness for a spinal brace are also found through experimental study and comparison of mechanical properties. Furthermore, various evaluations of prototype printed spinal braces are reported.

Chapter 4 describes the conceptual and final design as well as evaluation of airtightness and expansion of dynamic brace pads for brace casting process. The design and evaluation of brace casting frame with a healthy volunteer before implementation in clinic are also included.

Chapter 5 reports the accuracy and precision of 3D scanned torso along different dimensions and scan distance ranges with a Vorum Spectra 3D scanner. Also, the software reconstruction accuracy at brace pad covered contours is included. The chapter ends with an overview of the new 3D printed brace casting and manufacturing process.

Chapter 6 explains the randomized controlled trial (RCT) clinical study design, reports the preliminary in-brace corrections results as well as reporting the manufacturing time, cost and brace design parameter comparison between traditional and 3D printed brace.

Chapter 7 summarizes the findings from various studies in meeting the objectives of this thesis. Future work recommendations are also reported in this chapter.

Chapter 2: Background

This chapter provides the background information in scoliosis, bracing, three-dimensional (3D) printing and body contour capture technologies. Section 2.1. explains the anatomic directional terms and planes commonly used for describing spinal anatomy. Section 2.2. describes the spinal anatomy including structure of the spine, vertebrae feature and anatomical landmarks relevant to brace treatment. A comprehensive literature review on scoliosis is discussed in section 2.3. including definition, classification, prevalence, natural history, measurement, current treatment methods and risk factors of curve progression. In section 2.4., biomechanical theories of brace treatment, different brace types and classification are reported. In section 2.5., current brace manufacturing methods are described. Section 2.6. summarizes the factors affecting brace effectiveness and various brace materials. Multiple 3D printing technologies, print orientations and literature review on 3D printing applications in the biomedical field are provided in section 2.7. Lastly, section 2.8. includes literature review on current studies of 3D scanner used in scoliosis brace manufacturing followed by exploring specific commercial devices such as Microsoft Kinect, Rodin4D Structure Sensor, and Vorum Spectra 3D scanner for obtaining 3D scanned body shape.

2.1. Anatomic Directional Terms and Planes

Anatomic directional terms and planes are often used by clinicians for describing the structure location and movement direction of human body. The main anatomic directional terms include: superior and inferior, proximal and distal, medial and lateral as well as anterior (ventral) and posterior (dorsal) which are illustrated in Figure 2 - 1. Superior (upper) and inferior (lower) refer to structure location along vertical axis of the body. Proximal (closer) and distal (further) refer to toward and away from the trunk or origin of a structure. Medial and lateral refer to side to side position toward or away from the center of the body. Anterior (front) and posterior (back) refers to a structure's relative position to the front and back of the body. The three major anatomical planes are: Coronal plane (frontal plane), Sagittal plane (longitudinal plane) and Transverse plane (cross section) (Figure 2 - 1). Coronal plane divides the body into anterior and posterior sections. Sagittal

plane divides the body into left and right sections. Transverse plane divides the body into upper and lower sections.
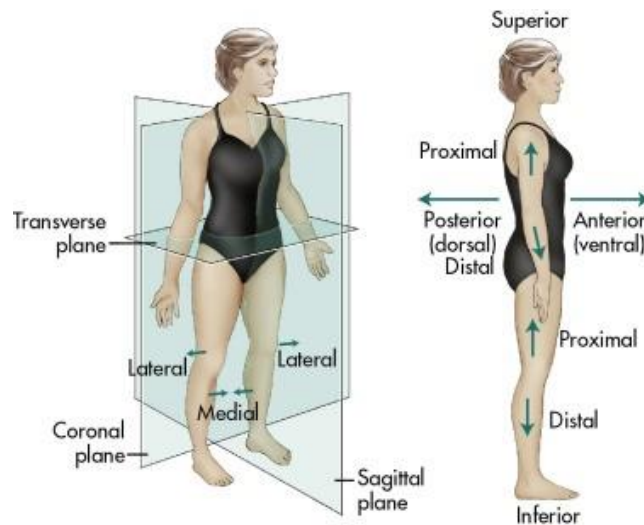
Figure 2 - 1 Illustration of anatomic directional terms and planes (Textbook of Diagnostic Sonography Eighth Edition, Chapter 5, p.81-98, 2018).

2.2. Spinal Structure

The spine (vertebrae column) consists of 7 cervical (C1-C7), 12 thoracic (T1 – T12), 5 lumbar (L1 – L5), 5 sacral, and coccyx bones (Figure 2 - 2). The cervical, thoracic and lumbar vertebrae provide protection for the spinal cord, nerve roots, structural support, mobility, and flexibility for the head, neck and torso. Normal curvatures in the sagittal plane include cervical lordosis (anterior convex curvature), thoracic kyphosis (anterior concave curvature) and lumbar lordosis (anterior convex curvature). These natural curvature forms sagittal balance where the center of gravity is maintained in an axis above the pelvis to minimize muscular exertion when spine is upright. However, the normal spine has no curvature in the coronal plane.

Adjacent vertebrae are articulated at the intervertebral and facet joints. Intervertebral joint (intervertebral disk) are made of fibrocartilaginous material at each vertebral level except for C1 and C2 allowing slight movement of the spine as well as acting as a shock absorber. Facet joints from superior and inferior articular processes guide and limit range of motion

for spinal segments. Vertebrae at the thoracic segment are articulated to the rib cage at its superior, inferior or transverse costal facet.
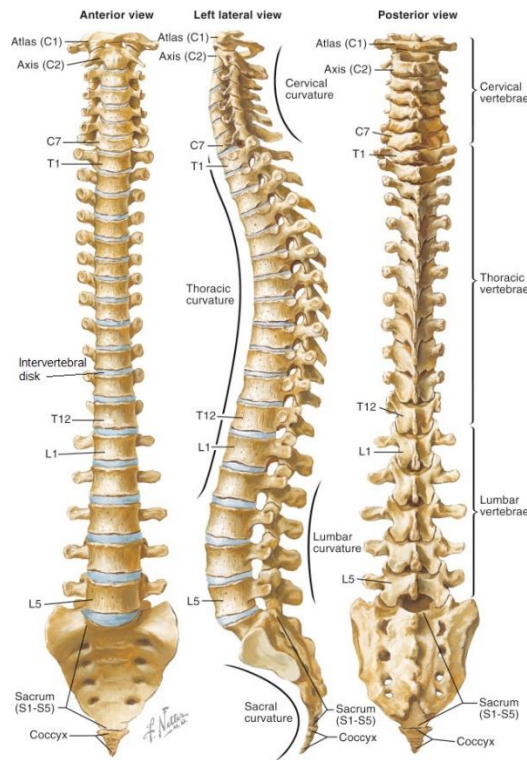
Figure 2 - 2 Anterior, lateral and posterior views of the spine (Modified from: Youmans and Winn Neurological Surgery Seventh Edition, Chapter 273, p.2259-2270, 2017).

The basic anatomy of a vertebra is a bony ring composed of vertebral body anteriorly and vertebral arch posteriorly as shown in Figure 2 - 3. Vertebral body is the oval portion and the main weight bearing structure of a vertebra. The upper and lower surfaces of the vertebral body interfacing with intervertebral disc are called endplates. The vertebral arch includes pedicles, laminae, and processes forming the vertebral foramen for the spinal cord to pass through. Pedicles connect the laminae to the vertebrae body. Laminae are posterior vertebral surfaces connecting the pedicles, transverse and spinous processes. Vertebrae at each spinal segment have identical general anatomy, however, they are distinguishable.

Thoracic vertebrae have small circular vertebral foramen, long spinous process, thick laminae and transverse processes. Thoracic spine is more stable with articulation with the ribs. Lumbar vertebrae are characterized with the largest vertebral bodies, wide laminae and larger pedicle than upper spinal segments.
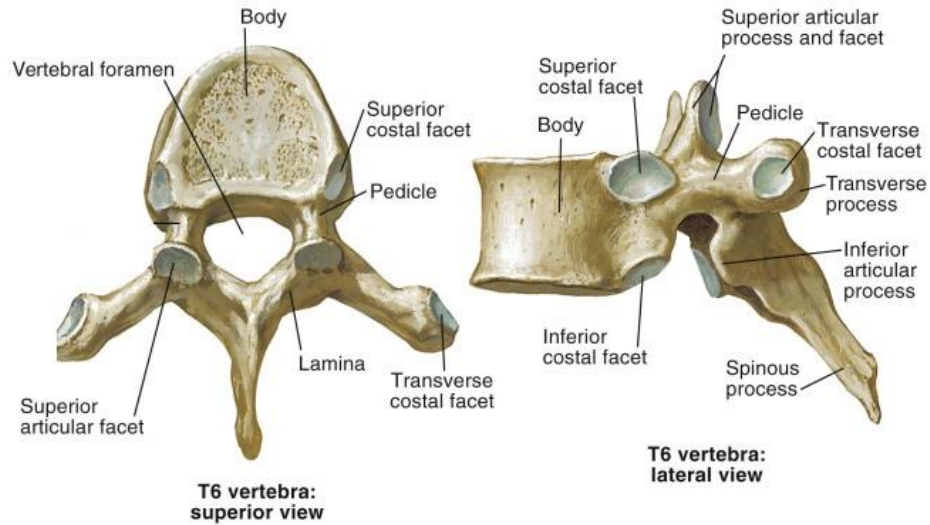
Figure 2 - 3 Basic anatomy of vertebrae (Modified from: Youmans and Winn Neurological Surgery Seventh Edition, Chapter 273, p.2259-2270, 2017).

Among the entire spinal structure, the important anatomical landmarks relevant for bracing include the waist, apex of curvature, axilla, greater trochanter, anterior superior iliac spine (ASIS), and iliac crest (Figure 2 - 4). Waist is between the lowest rib and the iliac crest. Apex of curvature refers to the vertebra within a curvature having the furthest lateral deviation from the center of spinal column in the coronal plane. The vertical distance between the waist and apex of curvature, as well as vertical distance between waist and axilla are often used by orthotist in brace fitting. Anterior superior iliac spine (ASIS) is a bony prominence of iliac crest of the pelvis. Protrusion and paddings are often added to a brace for bony prominence such as ASIS to minimize abrasion and pressure sores.
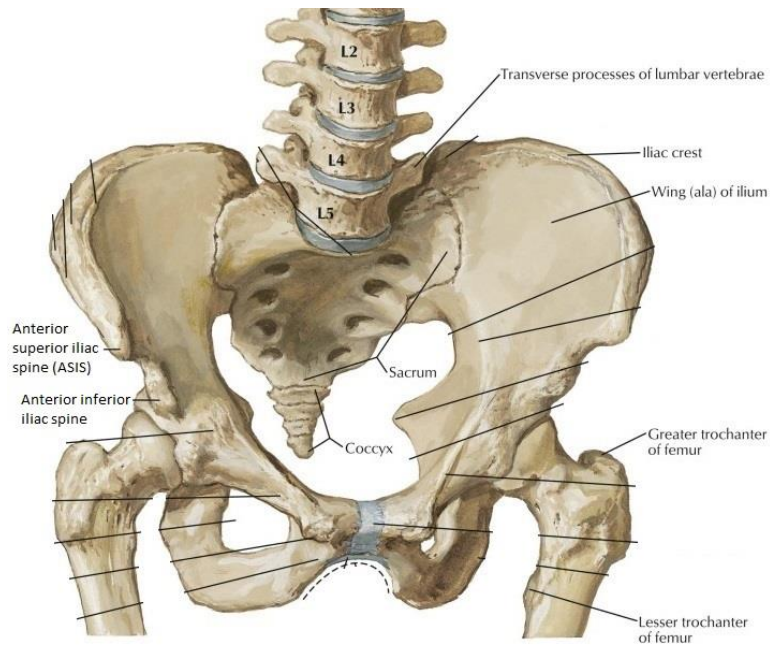
Figure 2 - 4 Pelvis bony framework relevant to brace fitting (Modified from: Atlas of Human Anatomy Sixth Edition, Chapter 6, p. 367-441, 2014).

2.3. Scoliosis

2.3.1. Definition of Scoliosis

Scoliosis is defined as a three dimensional spinal deformity consists of a lateral curvature and axial vertebral rotation [1], [2]. Cobb angle is the clinical measure from posterior-anterior (PA) standing radiograph for determining the severity of lateral deviation. A spinal curvature with a Cobb angle of 10 degrees or more is diagnosed as scoliosis. Figure 2 - 5 illustrates a scoliosis radiograph with a left lateral curve at the lumbar region defined by the apex location. Axial vertebral rotation (AVR) is the rotation of vertebra around the longitudinal axis of the body in the transverse plane [16]. Axial vertebral rotation is also evident in Figure 2 - 5 with the different shape of pedicles at the apex vertebra indicating different depths between left and right pedicle due to rotation.

Figure 2 - 5 Standing posterior-anterior radiograph of patient with scoliosis.

2.3.2. Classification of Scoliosis

Scoliosis can be classified into two major categories: non-structural and structural scoliosis. According to the Scoliosis Research Society (SRS), non-structural scoliosis is defined as a measured curve in the coronal plane in which the spinal curve can be overcorrect past zero on supine lateral side bending radiograph [17]. It is a lateral curve without rotation, and it is reversible with proper treatment of the underlying cause. It is usually a mild curvature caused by abnormal posture, shortened lower extremity, inflammatory disease of the spine and others [2], [18]. On the other hand, structural scoliosis is defined as a measured curve in the coronal plane in which the spinal curve cannot be corrected past zero on supine maximal voluntary lateral side bending radiograph [17]. It is a lateral curve with vertebral rotation that is often irreversible and usually associated with idiopathic scoliosis [2], [18], [19].

In terms of the cause of scoliosis, it can divide into 4 main types: congenital, neuromuscular, degenerative and idiopathic scoliosis. Congenital scoliosis results from abnormal segmented spine with failure of formation from birth. This leads to asymmetric

spinal growth that often associated with kidney dysfunction, urinary tract abnormalities or congenial heart defects [2], [20]. Neuromuscular scoliosis is caused by diseases such as cerebral palsy and muscular dystrophy that lead to inadequate function of nerves and muscles around the spine [2], [20]. Degenerative scoliosis is caused by degeneration of intervertebral discs or facet joints often associated with pain and discomfort [2]. Idiopathic scoliosis (IS) is defined as scoliosis with unknown cause [2].

Among the 4 different types of scoliosis, IS accounts for about 85% of the cases. Some researchers suggested that melatonin signal transduction deficiency [21] or genetic factors may be the underlying cause [4], [22]. It is reported that family members of patient with scoliosis are 6-10 times more likely than the general population to have scoliosis [2]. Idiopathic scoliosis is further subdivided by age of detection including infantile (birth to < 3 years old), juvenile (3 years to < 10 years old), adolescent (10 to <18 years old) and adult (>18 years old) [4]. Typically, there are no symptoms such as pain or discomfort caused by idiopathic scoliosis other than visual deformity [23]; it is easy for idiopathic scoliosis to be undetected until the curve significantly progresses.

Adolescent idiopathic scoliosis (AIS) is the most common type of scoliosis [24]. Physical features of deformity include asymmetry of neckline, shoulder blades or waistline, shoulder height difference, or abnormal rib hump [24]. Curve identification may include curve direction, location, and type. Curve direction is identified as right or left depending on the lateral deviation direction of the curve. Curve location is defined by the vertebral level of the apex of the curvature (the most lateral deviated vertebra within a curve). Curve location is identified as thoracic with apex locating at (T2-T11), thoracolumbar (T12-L1), lumbar (L2-L4), and lumbosacral (L5 and below) [25]. Curve types may include a single primary (major curve) with the largest Cobb angle, or additional secondary (minor curves) with smaller Cobb angle [25]. The most common curve type is right thoracic curve with or without secondary curve [20], [26].

2.3.3. Prevalence, Natural History and Measurement of Scoliosis

2.3.3.1. Prevalence

Adolescent Idiopathic Scoliosis (AIS) affects approximately 1 to 3% of the adolescent population (10-16 years old) [1]. Within those who are diagnosed with AIS, there are

approximately 30% with a curve magnitude greater than 30 degrees that requires treatment [4]. The number of boys and girls who are diagnosed with scoliosis are almost equally distributed, despite popular believe that incidence of scoliosis is higher for girls. However, girls have about eight times higher risk of curve progression compared with boys with Cobb angle >45 degrees [2].

2.3.3.2. Natural History

AIS is typically detected by asymmetry of neckline, shoulder blades or waistline, shoulder height difference, or abnormal rib hump. Spinal curve typically progresses, however it rarely progresses more rapidly than 1 degree per month. The risk of progression of a patient at Risser grade 0 and 1 with a curve magnitude of 20-29 is approximately 70% compared with 25% for those with the same curve magnitude at Risser grade 2, 3, and 4 [4]. It is rare for idiopathic scoliosis to have a severe deformation of greater than 100 degrees that causes cardiopulmonary problems, muscle fatigue or pain, postural imbalance or arthritic changes. However, a long term follow-up study of AIS patients reveals a higher risk of back pain and degenerative disk disease compared with normal population [4]. It is found that untreated AIS does not increase mortality rate but increases pain prevalence, and decreases self-image compared to those without AIS [27].

2.3.3.3. Early Detection and Measurement of Scoliosis

Adam forward bending test and scoliometer are used for early detection of AIS by identifying trunk rotation or asymmetry through school screening program [28]. Scoliosis Research Society (SRS), American Academy of Orthopedic Surgeons (AAOS), Pediatric Orthopedic Society of North America (POSNA) and American Academy of Pediatrics (AAP) acknowledge documented benefits of earlier detection for non-operative treatment of AIS [28], [29].

Scoliosis can be measured on radiographs, ultrasonography, computed tomography (CT) or magnetic resonance imaging (MRI) images for diagnosis, fitting and follow up [14]. The primary, clinical measure of scoliotic curve magnitude is Cobb angle. It is measured by selecting the most tilted end vertebrae with a curve and drawing a line parallel to each of the superior and inferior end vertebrae. Then, a line is drawn perpendicular to each of these lines. The angle of the intersection of the perpendicular lines forms the Cobb angle as

shown in Figure 2 - 6. Another parameter of measurement is axial vertebral rotation (AVR) [17]. There are different methods of measuring axial vertebral rotation. A commonly used Stokes' method involved the identification of center of pedicles and the fixed width to depth ratio at each vertebrae level for calculating rotation angle. This method required only standing PA radiograph, but it produces more random error [30], [31]. Radiography is the standard and clinically accepted method for measurement of AIS because it has good contrast between bone and soft tissue, economical and short imaging acquisition time. Nevertheless, standard radiograph has high level of radiation. Alternatively, EOS imaging system (EOS Imaging S.A., Paris, France) can be used. EOS imaging system is equipped with dual radiograph slots scanners. Furthermore, measurements from EOS imaging system accounts for pelvis tilt, and hip asymmetry. Importantly, study has shown that EOS imaging system decrease radiation dosage by 6-9 times and image quality is improved compared with standard radiograph [32].
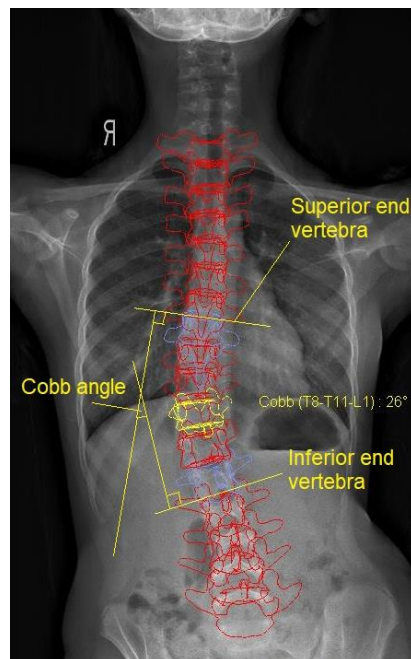
Figure 2 - 6 Cobb angle measurement from superior and inferior end vertebrae.

MRI provides good soft tissue contrast, but it is an expensive imaging method. MRI is used for rare cases of scoliosis involving rapid progression and unusual curves patterns and it is typically used for neuromuscular scoliosis [4], [20]. However, the severity of scoliosis is

reduced in the typical supine or prone position during MRI scan because of the decrease in gravitational effect [33].

CT scan can provide a high-quality 3D image of the spine compared to the standard 2D radiograph, but CT scan generates higher radiation. It is used in complex deformity especially when surgery is required [20]. For scoliosis patient that requires surgery, preoperative CT is recommended because of the screw insertion into narrow pedicles of the vertebra near the spinal cord [20]. Also, postoperative CT is recommended for patients with new neurologic complications after pedicle screw placement [20].

Both MRI and CT with cross sectional imaging capability are used in identifying scoliosis with underlying causes [20].

Recently, ultrasound has been proposed as a non-ionizing imaging alternative for measurement of AIS. Studies have shown ultrasound can measure Cobb angle within clinical accepted accuracy of 5 degrees [34]–[36]. That's because curve progression is defined as an increase of Cobb angle of more than 5 degrees [11], [20]. A pilot study also showed that ultrasound can measure AVR reliably with center of lamina method [37].

2.3.4. Treatment Methods

Physicians determine treatment of scoliosis based on age, physical maturity, growth potential, type of scoliosis, definition of curve (magnitude and location), rate of progression and if there is presence of pain.

2.3.4.1. Observation

No treatment is needed when Cobb angle is between 10-20 degrees. However, a child with significant growth remaining will require regular examination for observing signs of curve progression [2].

2.3.4.2. Bracing

Bracing is a proven non-operative treatment typically prescribed for AIS patients with curve magnitude of 25-45 degrees or a curve magnitude of 20 degrees with a rapid progression rate [2], [8]. Bracing is effective for preventing curve progression; it can eliminate the risks relating to surgery and reduces the health care cost associated. However, bracing has a higher failure rate for curves greater than 40 degrees, and patient compliance

in wearing the brace affects treatment effectiveness. One multicenter study with 116 patients showed a mean compliance rate of 67% of prescribed wear time [8].

2.3.4.3. Surgery

Most orthopedic surgeons recommend surgery for adolescent with Cobb angle > 45 degrees, adult with Cobb angle > 50 degrees that shows progression or severe back pain or if brace treatment fails and curve progresses significantly [2]. Nevertheless, orthopedic surgery is a complicated procedure and life threatening. It carries significant risks with possible surgical complications that may lead to neurological damage, persistent pain or death.

2.3.5. Risk Factors of Curve Progression

Curve progression is clinically defined as an increase of curve magnitude of greater than 5 degrees [11], [20]. The risk factors associated with progression include gender, initial age, curve pattern and location as well as pubertal status. But the most significant risk factor is the initial curve magnitude [2], [11]. On another note, spinal curve can progress even after skeletal maturity. It is shown that about 2/3 of scoliosis patients in a 40 years follow-up study shows some degrees of curve progression even after skeletal maturity [2], [38].

2.4. Literature Review on Biomechanical Principle and Theory of Bracing and Different Brace Types

2.4.1. Biomechanical Principle and Theory

There are a variety of brace designs based on different biomechanical concepts. A questionnaire regarding scoliosis cases and brace treatment approaches were presented to specialists from the Society on Scoliosis Orthopedic and Rehabilitation Treatment (SOSORT). The questionnaire results in area such as proper pad placement at the thoracic region [39] were divided between 50% suggesting pad reaching apical vertebra and 50% suggesting pad placement acting caudal to the apical vertebra. This study reveals different opinions and conflicting ideas with brace design and their respective biomechanical concepts for treatment of scoliosis. Nevertheless, general consensus accepts the "three-point system" (Figure 2 - 7 (a)) correction principle, where force is applied to the apex of the scoliotic curve, followed by two counterbalancing forces: one superior and one inferior

16

to the apex [10]. This will dynamically shift curve to desire position. Furthermore, the pad at the thoracic region is typically positioned to apply a "posterior lateral to anterior medial" force for de-rotating the spine [39]. Similarly, a "four-point system" (Figure 2 - 7 (b)) is generally accepted for double curves with superior and inferior counterbalancing forces for each apex [40].

(a)   **(b)**
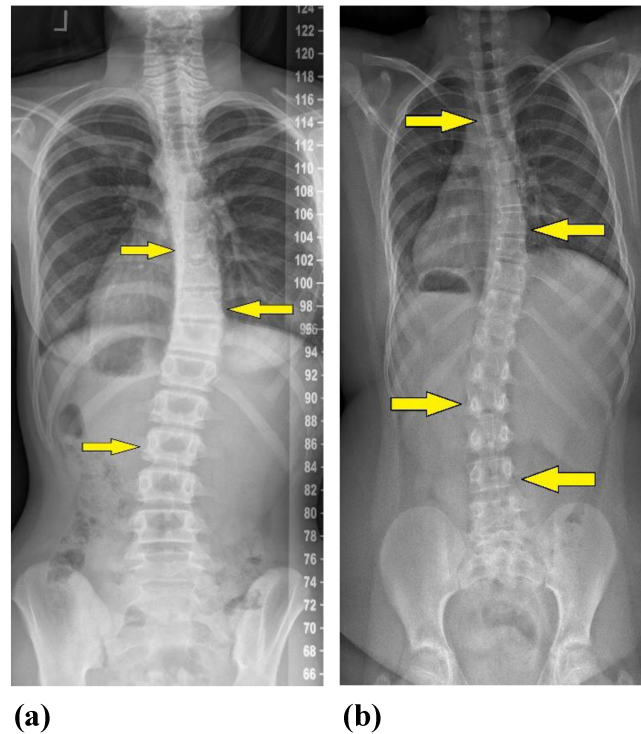
Figure 2 - 7 General brace correction principle. (a) Three-point system. (b) Four-point system.

Brace designs generally follow two components of biomechanical correction mechanisms: passive and active mechanism. Passive mechanism is where mechanical force and support is applied to the body through contact with the brace. On the other hand, the active mechanism is where the patient pulls away from the pressure site from the brace. Both mechanisms aim for correction of the abnormal curvature [10].

Other important biomechanical theories for brace treatment are Hueter-Volkmann principle and Vicious Circle Model. Hueter-Volkmann principle states that bone growth is retarded by increase mechanical compression and accelerated by reduction in loading [41]. This theory suggests that asymmetric compressive loading applied to growth plates of vertebral bodies on the concave side of the curve retards normal growth and lead to

wedging of vertebral bodies, which plays a part in development of adolescent idiopathic scoliosis [10], [42]. Bracing would unload the growth plates near apex of curve leading to acceleration of normal growth [10], [42]. Vicious Circle Model is a theory that suggests the asymmetric loading of spinal column is the primary force for progression of curves. Deformity would further increase asymmetric loading which in turn worsen deformity [43]. Brace treatment is expected to break the cycle [44]. In general, a brace applies an external force to the trunk, which imparts corrective force on the spine. The force applied may include longitudinal traction, lateral pressure from brace pads and straps, or contact pressure from the brace itself [45].

2.4.2. Brace Types and Classification

Some well-known European brace types include Chêneau brace, and Lyon brace as shown in Figure 2 - 8. Some well-known American brace types include Boston brace, Charleston bending brace, Milwaukee brace, Providence brace, and SpineCor brace as shown in Figure 2 - 9. Characteristics of the braces are explored, which includes the biomechanical theory behind each brace design. Most braces mentioned above are classified as TLSO (Thoracic-lumbar-sacral orthosis) except for Milwaukee brace, which is a CTLSO (cervical-thoracic-lumbar-sacral orthosis). This brace classification is based on curve location (apex of the abnormal curve) the braces can treat.

Chêneau brace was designed in the 1960s. It opens anteriorly and divides into zones with large free spaces for opposite pressure site. The spacing allow deep breathing for patient while in-brace, ease of movement of torso as well as de-rotating effect [46]. Chêneau brace is constructed to allow 3D correction of curve. It pushes on the right convex posterior rib prominence and simultaneously on the left anterior rib prominence at corresponding part of the brace to push perpendicularly to the body surface against the apex of the curve [47]. Passive mechanisms that are used include curve hypercorrection, elongation or "Cherry stone effect" (compression of brace on the body causes upward stretching of the body between pelvis to ribcage which helps straighten the curve), unloading of asymmetric loading, de-rotation of thorax, bending, and tissue transfer (displacement of body tissues from convex to concave part of the trunk) [47]. Active mechanisms that are used include asymmetrically guided respiratory movement of the ribcage, and anti-gravitational effect

(postural control, a portion of brace is away from axis of balance, the automatic reaction of the body to regain balance) [47].

A variation of the Chêneau brace include Rigo Chêneau brace (early 1990s). It offers regional de-rotation, the brace de-rotates the thoracic section against lumbar section, with counter-rotation pad at the upper thoracic region [48].

Another variation of the Chêneau brace is the "Chêneau light" brace (2005). It is made by removing brace material where the torso is expected to move in order to create a lighter weight brace with increase comfort. It is also adjustable [49].

Lyon brace (1958) is a rigid, asymmetric, and adjustable brace. Treatment process requires initial plaster cast to stretch deep ligaments before application of the brace [46]. Corrective plaster cast enables lengthening of concave ligaments, where ligaments undergo plastic deformation. The biomechanical theory of the brace focuses on a 3-point system for correction with thoracic de-rotation [50]. Lyon brace uses active axial auto correction and elongation (pelvic/scapular extension with equal distribution of forces on left and right side of the body) [51].

A variation of the Lyon brace is the ART Lyon brace (2013). It stands for Asymmetric, Rigid, and Torsion. Studies showed that in-brace correction of 70% is achieved [51], [52]. The ART brace has unique segmented molding in the lumbar and the thoracic areas, which reduces the likelihood of reduction of natural curvature in the sagittal plane. Elongation along the axis of the spine is carried out with simultaneous clamping of two halves of polycarbonate pieces simulating squeezing of the torso. The ART brace uses superposition of different CAD/CAM molds and segmental 3D reconstruction for designing the brace on the computer. The brace also have overcorrection effect on the coronal and sagittal plane at the pelvis, lumbar, and thoracic levels [51].
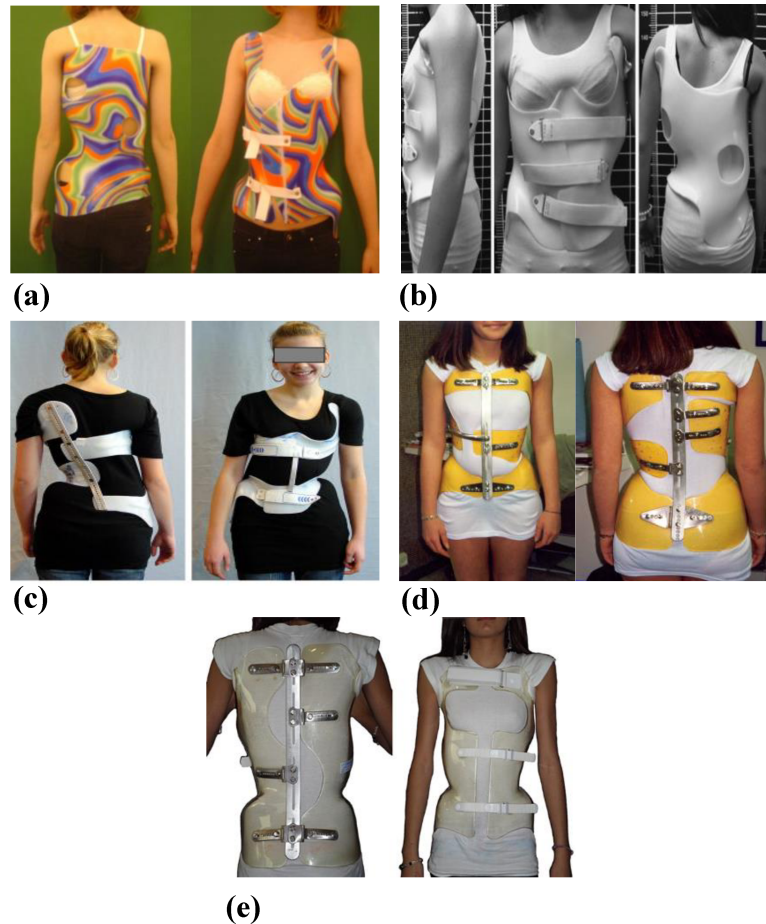
Figure 2 - 8 European braces. (a) Chêneau brace [53]. (b) Rigo Chêneau brace [46]. (c) Chêneau Light [54]. (d) Lyon brace [50]. (e) ART Lyon brace [55].

<u>Boston brace</u> (1972) is the most frequently used TLSO in North America. It is a symmetric, posterior opening brace with apical pads. Boston brace is pre-fabricated based on different plaster fitting models [46]. Passive mechanism is used for loading on the scoliotic curves. Brace design includes a 15° lumbar lordosis to decrease the tendency of reduction of natural curvature in the sagittal plane as well as a cut-out section to encourage movement of torso [46]. In-brace correction is about 50% based on a study [56]. However, Boston brace still tends to decrease thoracic kyphosis in the sagittal plane. Also, it does not produce significant changes in rib hump or apical vertebral rotation. Improvements are required for a more complete 3D correction of scoliotic deformities, which will result in not only reduction of Cobb angle in the coronal plane [57].

Charleston bending brace (1979) is a night time brace based on Hueter-Volmann principle where growth is retarded by increased mechanical compression, and accelerated by reduce loading [41]. It aggressively overcorrects the spine with side bending posture. Night time brace has the advantage of change in direction of gravity relative to body axis when lying down. Corrective forces are applied to costovertebral joints at this position as well as minimize muscle tone at rest [44]. Charleston brace is effective for single curves but it will worsen secondary curves for patients with multiple curves [58]. It uses 3-point system for curve correction [46].

Milwaukee brace (1945) is a CTLSO and the development of this brace is a landmark in treatment of scoliosis because it is the first widely used removable brace for scoliosis. It provides both passive and active mechanisms for curve correction. It can correct abnormal cervical scoliotic curve, however, it is proposed for nighttime only due to low compliance because of aesthetics with neck ring and three metal uprights [46]. Theoretically, thoracic or axillary sling apply direct passive curve correction, while throat molds or lateral pads allow for active correction as patient intentional move away from these components. Nevertheless, the active component of this brace plays little part in curve correction [46]. The pelvic module and neck ring with or without chin rest as well as the occipital pad help provide longitudinal traction force to the spine [59]. Longitudinal and especially transverse force applied by the brace are effective in correcting both coronal and sagittal plane deformity for patients with flexible spinal deformity [60]. Interface pressure between patient's body and thoracic pad is shown to be highly correlated with the tension of thoracic strap with this brace [61].

Providence brace (1992) is an asymmetric night time brace with selective contact points that provide curve correction by direct application of de-rotational and lateral forces.

The Providence system of brace fabrication begins with the patient laying on a polycarbonate measurement board. The measurement board contains vertical and horizontal grid hole for padded bolster placement to ensure optimal curve correction during fitting process. Providence brace is more frequently use nighttime brace than Charleston brace [46]. This brace applies lateral force to bring apexes of scoliotic curve to the centerline or beyond. This involves creation of void areas where brace does not contact the torso on the opposite of pressure sites. The brace is a continuous plastic shell without holes

for maintaining pressure exerted on curve. Providence brace uses a three-point system for correction of curve and elevates patient's shoulder in order to have a higher stabilizing pad on upper thoracic spine for treating curves with apexes as high as T6 vertebrae [62].

SpineCor brace (1993) is strap-based, non-rigid and elastic. It relies on patient movement to activate corrective effects. Even though aesthetically acceptable, due to poor initial response and questionable effectiveness with larger curves, it is abandoned by most clinicians [46]. Pelvic base, crotch bands, thigh bands act as anchoring point and support for actions applied to patient's trunk by the elastic bands. Stable pelvic base allows traction by the elastic bands. Bolero and corrective elastic bands use dynamic corrective principle aimed at modify postural geometry of moving spinal column [63].
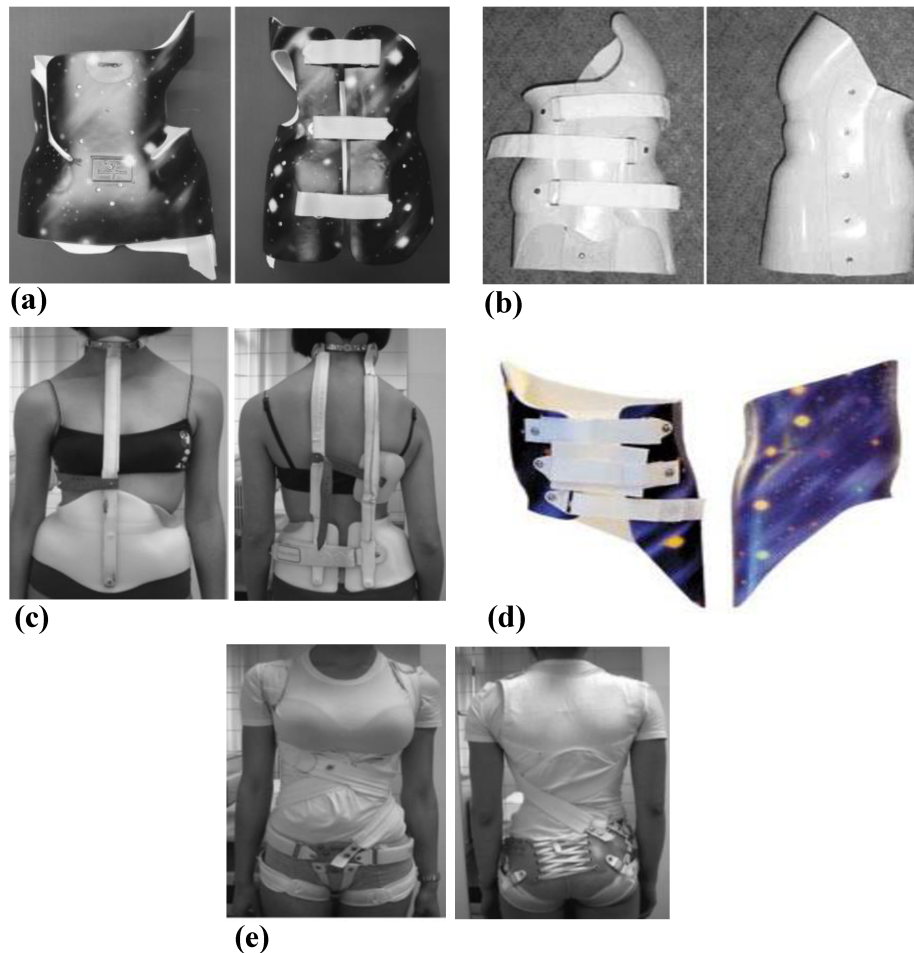
Figure 2 - 9 American braces. (a) Boston brace [46]. (b) Charleston bending brace [46]. (c) Milwaukee brace [46]. (d) Providence brace [64]. (e) SpineCor brace [46].

2.5. Literature Review on Brace Manufacturing

2.5.1. Current Casting Methods for Brace Fabrication

Following the prescription of brace treatment from initial diagnosis of curve severity, conventional brace manufacturing typically begins with casting. Current casting process involves the creation of a custom temporary negative mold of patient torso geometry. There are a number of casting methods including standing casting, standing with traction casting, frame casting, supine lying casting, and supine lying with traction casting [65]. Two common casting methods are frame and supine with traction casting [65] as shown in Figure 2 - 10. Frame and supine with traction casting involve plaster wrap patient from sternal notch to hip to obtain body shape [15], cutting out negative plaster cast, and resealing plaster cast for the next manufacturing steps [65]. Frame casting method uses a standing frame where pressure pads or bolsters mounted on the frame are applied to patient torso in reducing coronal lateral curvature and trunk rotation [65], [66]. The frame simulates in-brace condition where orthotist aims to obtain 50% in-brace correction for adequate curve correction while comfortable for patient to maintain brace wear compliance [59]. Patient will typically hold on to handles of the frame for trunk stabilization during casting [65]. Supine with traction casting method is where patient is lying on a bed in supine position while cephalocaudal traction of about 10% body weight is applied to obtain desire brace geometry. However, no other correction is applied to the spinal curves [65]. Study with 2 years follow-up of 80 AIS patients after taken off TLSO brace has reported pre-brace and 2 year after out of brace Cobb angles using frame and supine with traction casting. Both methods demonstrated significant reduction of Cobb angle between pre-brace to the start of weaning of brace period. However, frame casting showed better reduction in apical axial vertebral rotation at the early stage of the brace treatment. Supine with traction casting showed more effectiveness in postural alignment with greater long term reduction of truck listing (cervico-sacral lateral offset) [65].

Recently, ultrasound-assisted brace casting is shown to be beneficial for brace fitting and manufacturing by minimizing radiation exposure on growing children who require brace treatment [66]. An ultrasound system, a custom providence brace standing frame and a custom pressure measurement system are used during the casting process [66]. Figure 2 -

11 illustrates ultrasound image overlay with a radiograph. Ultrasound and pressure measurement system provides orthotist with real-time measurement of curve correction and pressure applied from brace pads to patient torso. This enables the orthotist to adjust pad pressure and location objectively based on quantifiable curve correction in real time [14], [66]. Then, orthotist applies plaster wrap on patient in standing position, followed by identical pad pressure levels and locations to simulate the in-brace correction configuration obtained previously. After that, a negative mold is created when the plaster wrap hardens. It was shown by study [67] that ultrasound-assisted casting decreased the number of in-brace radiographs and follow up adjustments as well as increasing in-brace correction.

(a) (b)

Figure 2 - 10 Two common casting methods. (a) Supine with traction [68]. (b) Frame casting [66].
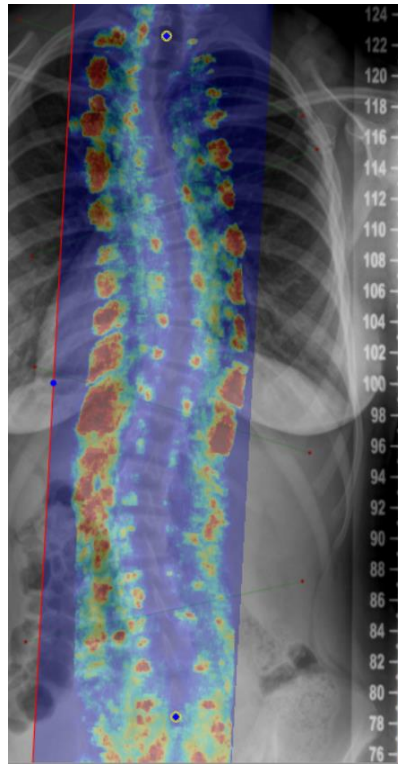
Figure 2 - 11 Ultrasound image overlay with radiography.

2.5.2. Current Methods for Brace Manufacturing

After casting, current brace manufacturing involves either the conventional manual method or CAD/CAM method in creating the final brace [15]. The manual method requires filling the temporary negative mold with liquid plaster, then removing the temporary mold once liquid plaster solidifies to form a positive mold. After that, cast rectification occurs by adding and removing plaster at specific areas such as abdomen, pelvic (anterior and posterior superior iliac spine, iliac crest), lumbar, thoracic, and axilla region [15] as shown in Figure 2 - 12. Rectification begins with labeling landmarks on the torso, then outlining boundary for regions and locating apex line inside the region. Pressure regions (addition of plaster) are created at abdomen and the region immediately above iliac crest. Relief regions (removal of plaster) are created at anterior and posterior superior iliac spines and along iliac crest [15]. Other pressure and relief regions are created according to "three-point" or "four-point" system to allow sufficient curvature reduction and trunk shift as determined by the orthotist. After that, heated plastic sheet is formed around the rectified positive plaster mold. Then, trim lines are cut; pads and straps are added on the thermoformed

plastic sheet to create a brace [15]. Lastly, final adjustments are made after final fitting of the plastic brace on the patient [15].

Alternatively, the CAD/CAM method begins with scanning the temporary negative cast with a laser scanner. After that, relevant landmarks are placed on the computer model of the torso. Cast rectification is completed virtually on the computer model with custom software as shown in Figure 2 - 12. After that, a positive foam mold is created by a craver milling machine with the modified computer file of the cast. Then, plastic sheet is thermo-vacuum formed by heating plastic sheet and forming it around the positive foam mold with small holes for vacuum suction [15]. Lastly, the remaining brace manufacturing steps are identical as the conventional method. Overall time in creating a brace is reduced by 93.3 min (37.2%) with the CAD/CAM method compared to conventional method [15]. Furthermore, study showed no significant difference between the two methods in 19 out of 25 dimensions of the five rectified regions [15]. Labour time for surface smoothing and building up of the sacrum pad are significantly reduced in CAD/CAM method. CAD/CAM method has the benefit of reducing brace manufacturing time for orthotist and more time for patient care [15]. Other existing technologies include MRI scans to produce brace within 3% error in different dimensions compared to plaster cast but with high cost [14], [69]. Another study shows that FEA simulation can be used to determine optimal pressure and location of brace pads during casting to correct spines with different stiffness [14], [70].

Figure 2 - 12 Brace manufacturing methods. (a) Manual method cast rectification [71]. (b) CAD/CAM method cast rectification [15].

2.6. Literature Review on Factors Affecting Brace Effectiveness and Brace Materials

2.6.1. Overview of Brace Treatment Effectiveness

2.6.1.1. Background

The effectiveness of brace treatment had been under debate [72][73]. In particular, a study shows no statistically significant differences in surgical rate between an active bracing center and a center where observation and non-intervention are the practices [73]. However, these studies have not investigated and accounted for the factors that affect the effectiveness of brace treatment outcome. The reason behind conflicting conclusions about the effectiveness of brace treatment is due to inconsistent inclusion criteria for brace treatment and different definitions of brace effectiveness [10]. A 242 patients multicenter landmark study with a 116 patients randomized control cohort and a 126 patients preference cohort by Weinstein et al. [8], have demonstrated the effectiveness of brace treatment including SRS Committee standardized criteria for AIS brace studies [9]. The study was stopped early due to statistically significant difference between the effectiveness

of brace treatment group compare to observation group, as well as the strong positive association between amount of brace wear time and treatment success. The result shows 75% treatment success in bracing and 42% in observation with the randomized control cohort [8]. Brace treatment is not only proven to be effective, but in order to determine and improve brace effectiveness, it is important to understand the underlying factors that affect brace effectiveness.

2.6.1.2. Definition of Brace Treatment Effectiveness

Effectiveness of brace treatment or treatment success is defined as preventing curve progression during high risk growth period of early adolescence up to skeletal maturity and prevent the need for surgery [10], [8]. More specifically, according to SRS Committee standardized criteria for AIS brace studies, brace effectiveness is assessed based on percentage of patients who have less than or equal to 5 degrees of progression, percentage of patients who have greater or equal to 6 degrees of progression at maturity (Risser 4 or above, <1 cm change in height and 2 year post-menarcheal for girls), percentage of patients with curve exceeding 45 degrees at maturity, percentage who had surgery recommended or undertake, and percentage of patients who require surgery with two years follow-up after skeletal maturity [9].

2.6.2. Factors Affecting the Effectiveness of Brace Treatment

An essential factor that affects the effectiveness of brace treatment is the potential risk of curve progression. Identification of patients with high risk of curve progression will prevent unnecessary treatment, and benefit patients from the use of brace. Therefore, factors that influence the risk of curve progression are also factors that affects effectiveness of brace and they are suitable inclusion criteria for brace studies [8], [9]. Factors that affects curve progression include initial age of detection, gender, pubertal status, skeletal maturity, curve type, peak height velocity, axial vertebral rotation (AVR), menarcheal status and most importantly initial Cobb angle [3], [8]–[11], [74]–[76]. Early and intensive bracing is believed to prevent the need for surgery in most case [75]. Bracing is recommended for patients with one or two years of growth remaining [3]. Optimal inclusion criteria for brace studies from SRS committee are initial age of detection of 10 years or older, skeletal maturity of Risser 0-2, primary curve angle of 25-40 degrees with no previous treatment,

and pre-menarcheal or less than 1 year post-menarcheal if patient is female [9]. These groups of patients represent those who are most at risk with curve progression. Another factor that affects effectiveness of bracing is weaning protocol. A study recommends weaning from brace at skeletal maturity (Risser 4 or more), 12 months post-menarcheal or no documented growth height [77].

Beside the physical and clinicians' controllable factors, compliance and in-brace correction are other important factors affecting effectiveness of brace treatment. They are patients' controllable factors that have significant potential for improvement of effectiveness. Compliance includes quantity of brace usage (wear duration) [13], which can be measured objectively with temperature, humidity sensors or pressure switches [78], [79]. Compliance also involves quality of brace usage (in-brace forces) [13], which can be determined objectively with standard force or pneumatic sensors by measuring the lateral pad force in a single pad area, where major corrective forces are applied to the torso [10]. Pressure and tension monitors can measure the magnitude of pressure from the brace and forces from straps [80]. Evidence that demonstrates the importance of tightness of brace on effectiveness is shown in a study where Cobb angle is found to correlate with pressure applied by the pad and strap tension [12]. There exists a low power portable load monitoring system to record time and tightness of brace. Through clinical study with the device, it is suggested that quality of brace usage is just as important as quantity of brace usage in preventing curve progression [81], [82]. It is also found that a battery powered microcomputer system with air bladders can monitor and even maintain loads exerted from the brace to the curve, which results in increase time of patient wearing the brace at the prescribed tightness [83]. In the study by Weinstein [8], during first 6 months of brace treatment, only 41% of patient have treatment success with average 0 to 6 hours of brace wear per day, compare with 90-93% success rate for those with at least an average of 12.9 hours of brace wear per day. In another study by Rahman [84], curve usually do not progress with at least 85% compliance to prescribed time, compare with progressive curves with 62% or less compliance. In-brace correction is also a predictor of brace effectiveness and might be dependent on curve flexibility [13]. Recently, a study [13] has shown ultrasound can measure simulated in-brace correction in real time. Curve flexibility can

also be measured from ultrasound and contributes to the effectiveness of brace treatment [8]–[10].

2.6.3. Traditional Brace Materials

There are many different materials which can be used for different brace types and are summarized in Table 2 - 1. Among these materials, polyethylene and polypropylene are thermoplastic materials that are most commonly used. Other than the shell of the brace, some braces also include additional supporting structures. These supporting structures can be made of radiolucent duralumin, aluminum, steel, Kydex or carbon fiber reinforced plastics. No literature was found for determination of the optimal brace material or quantitative rationale behind selection of brace material.

Table 2 - 1 Common brace materials for different brace types

Material	Brace Type	Brace Part
Polyethylene (PE)	Charleston, Cheneau and derivatives , PASB, Rosemberger, TLI, , Carbon [46]	Body, [46]
Polypropylene (PP)	Dynamic De-rotating [46], Providence [85], Boston [86], Milwaukee [86], Wilmington [86]	Body [46], [85], [86], Pelvic Girdle (Milwaukee) [86]
Poly (methyl methacrylate), Plexiglass (PPMA)	Lyon [46]	Body [46]
Polycarbonate (PC)	Sforzesco, ART [51], [87], [88]	Body [51], [87], [88]
Acrylic-Polyvinyl Chloride (Kydex)	Carbon [89]	Three Strengthening Straps [89]
Carbon Fiber Reinforced Plastic (CFRP)	Providence, Carbon [62], [89]	Reinforcement structure, carbon blades [62], [89]
Radiolucent Duralumin	Lyon, Sforzesco, ART [46], [51], [87]	Adjustment, Supporting structure [46], [51], [87]
Aluminum	Dynamic De-rotating, Milwaukee [46]	Support bar, structure [46]
Steel	Milwaukee [46]	Supporting structure [46]
Elastic Tissue	SpineCor [46]	Body straps [46]
Polyamide	UNYQ Align [90]	Body [90]

N/A indicates information not available through literature review

2.7. Current 3D Printing Technologies

2.7.1. Overview of 3D Printing Methods

There are many 3D printers with different printing methods available. Different 3D printing methods are explored to determine a suitable 3D printing method for printing a scoliosis brace. The different printing methods can be classified into four major categories based on the physical state of supply materials which include liquid, powder, solid sheet and gas based. Table 2 - 2 summaries the classifications, characteristics and Figure 2 - 13 illustrates in picture format the major 3D printing methods. All the major printing methods in Table 2 - 2 can create parts made of thermoplastic which is typically used as brace material. The most common 3D printing methods based on past vendor sales include SLA, FDM, and SLS [91].

2.7.2. 3D Printing Method Mechanism, Advantages and Disadvantages

2.7.2.1. Stereo-Lithography (SLA)

SLA uses ultraviolet laser curing to selectively solidify parts of a liquid resin layer in a vat resin bath. First layer is solidified on a platform, where the platform slowly moves up to allow successive layers to be solidified to form the final piece [92]. The advantage of SLA include creation of a part that has broadly isotropic mechanical properties [93]. Some disadvantages of SLA include error with overhang parts with over curing due to overhang parts not fused with bottom layer [92], and additional cost and time are required for post-processing steps [94].

2.7.2.2. Fused Deposition Modeling (FDM)

FDM melts a feedstock of thin filament with the print head and extrudes it in a stream of hot viscous material typically with a thickness of 0.25 mm [92]. The viscous material is deposited onto a base plate to form layers to build a part [92]. The advantages of FDM include little post-processing (soluble or breakaway support materials), relatively economical machine and materials [95]. However, FDM produced parts does not have smooth surface finish and they have anisotropic mechanical properties depending on print orientation [96].

2.7.2.3. Polyjet

Polyjet uses inkjet technology to deposit liquid photopolymer resin and each layer is cured with UV lamps [92]. The layer thickness is typically about 0.016 mm [92]. The advantages with Polyjet include creation of high resolution parts, little post-processing required with easy to remove support material [92]. The disadvantage includes change in mechanical properties over time [97].

2.7.2.4. Selective Laser Sintering (SLS)

Powder is sintered (fused to form a mass with heat) by applying carbon dioxide laser in an inert gas chamber at selective location of each layer [92]. The chamber is kept at near melting point of powder material. Powder bed is lowered the same amount as layer thickness when a layer is finished [92]. This allows sintering of successive layer to form a part [92]. The advantages of SLS include wide range of material selections and mechanical properties [91]. Also, SLS does not require support material since excess powder acts as support for overhang structures, which allows printing of parts with complex geometry [95]. The disadvantages of SLS include parts with surface porosity [98] as well as generally additional post-processing required for final part [99].

2.7.2.5. Three-Dimensional Printing (3D-P)

3D-P typically uses water based liquid binder supplied in a jet similar to 2D printing on a paper to a starch based powder bed [92]. Powder are glued together when binder is added to form a layer of a part [92]. Solid powder material deposits in layers are successively fused by binder to form a part [91]. The advantage of 3D-P include fast printing speed and relatively low cost method [91].

Figure 2 - 13 3D printing methods. (a) Stereo-Lithography (SL) [100]. (b) Fused Deposition Modelling (FDM) [101]. (c) Polyjet. [102] (d) Selective Laser Sintering (SLS) [103]. (e) Three-Dimensional Printing (3D-P) [104].
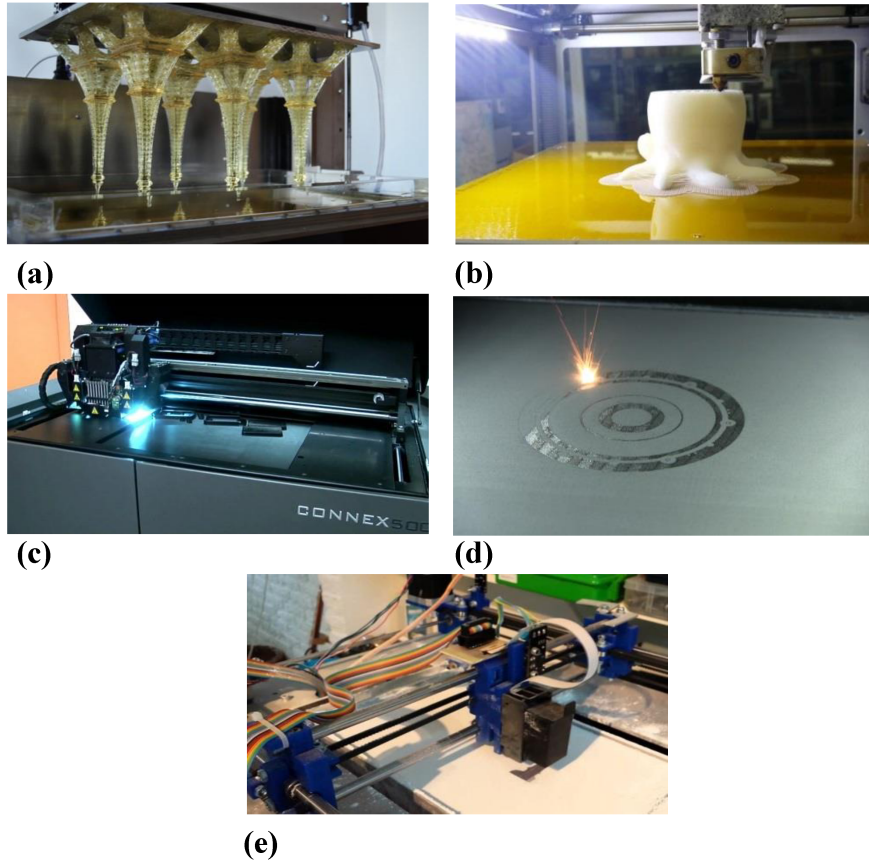
Table 2 - 2 3D printing methods classification and characteristics

3D printing method	Supply from nozzle	Layer creation techniques	Phase change during layer solidification	Printing Materials	Example of Printer Systems	References
Stereo-Lithography (SLA)	Liquid	Liquid layer deposition	Photo-polymerization (cure by UV light)	Photo-polymers: Acrylates, Epoxies, filled resins (glass, ceramic, metal),	3D system-SLA	[91],[92]
Fused Deposition Modeling (FDM)	Liquid	Continuous extrusion of and deposition	Solidification by cooling	Polymer: (ABS, PLA, PC) Wax Metals or ceramics with binder	Stratasys-FDM	[91],[92]
Polyjet	Liquid	Drop on demand deposition	Photo-polymerization (cure by UV light)	Acrylates, Epoxies, filled resins (glass, ceramic, metal)	Stratasys-Objet	[92]
Three-Dimensional Printing (3D-P)	Powder	Layer of powder + drop on demand binder printing	No phase change	Ceramics, metals or polymers with binder	Soligen-DSPC	[91],[92]
Selective Laser Sintering (SLS)	Powder	Layer of powder	Laser sintering/laser melting and resolification by cooling	Polymers, filled polymers, metals with binder, metals, sand, ceramic	DTM-Sinterstation	[91],[92]

2.7.3. Print Orientations

Print orientation is important not only for fitting the build volume of a printer, but it also affects the material properties of created part depending on printing method used. FDM printed part has anisotropic material properties [96], which results in different material properties such as tensile strength in different print orientations [96]. SLS has overall anisotropic material properties, but with some identical material properties in transverse print orientations [98], [105]. Polyjet printed part has overall anisotropic material properties, however some material types have certain isotropic material properties for different print orientations (Upright, Side, Flat) [97]. SLA on the other hand has broadly isotropic material properties as mentioned in section 2.7.2.1., with similar material properties in different print orientations (Upright, Side, Flat) [93].

2.7.4. Review of 3D Printing in Biomedical Applications

Currently, 3D printing has been applied in many biomedical areas which include bone tissue scaffolds, surgical tools and fixtures, hearing aids, prosthetics, orthotics, anatomical models for surgical planning and modelling, implants, tissue and organ fabrication, and pharmaceutical drug delivery [106]–[110]. 3D printing is particularly promising for time and cost reduction in customized medical equipment and products [106].

In particular, examples of 3D printing currently used in orthotic applications include foot and ankle-foot orthoses (AFOs) [111], [112]. One foot orthosis was created, fitted on participant and demonstrated comparable kinematics measures as traditional plaster cast foot orthosis [112]. Also, two AFOs had been created with a 3D scanner and 3D printer demonstrating comparable function from gait analysis [111].

Furthermore, 3D printed spinal braces are now commercially available [113]. One company (UNYQ, San Francisco, USA) had printed braces in 3.5 mm thickness [113] and they had provided white paper clinic results [114]. Another clinician had printed 3D printed brace with PLA materials [115]. However, there is no literature demonstrating clinical effectiveness or evaluating 3D printed spinal brace design parameters and mechanical properties.

2.8. Existing Technologies for Obtaining Body Shape

2.8.1. 3D Scanner in Scoliosis Brace Manufacturing

Acquiring 3D body contour digitally is necessary for modification of brace shape virtually and directly 3D printing modified file to create a brace. Literatures on the use of 3D scanner for brace manufacturing include manufacturing time and dimensional difference study comparing braces created by 3D scanning negative plaster cast with convention plaster casting method [15]. Another study has compared clinical outcomes such as in-brace coronal and sagittal curvatures as well as patient comfort level in wearing braces created by 3D structured light scanner with conventional plaster cast method [116].

3D structured light scanner is the most viable scanner type for acquiring body shape, because it does not require complex scanning system setup while providing rapid acquisition of smooth surfaces [117]. Therefore, three commercial 3D structured light scanners including Microsoft Kinect (Microsoft Corporation, Redmond, USA), Rodin4D structure sensor (Rodin S.A.S., Pessac, France), and Vorum 3D handheld Spectra Scanner (Vorum Research Corp. Vancouver, Canada), as shown in Figure 2 - 14 are further explored.

(a)

(b)

(c)

Figure 2 - 14 Commercial 3D scanner. (a) Microsoft Kinect. (b) Rodin4D structure sensor.
(c) Vorum 3D handheld spectra scanner.

2.8.2. Commercial Structured Light 3D Scanners

2.8.2.1. Microsoft Kinect

The first generation Microsoft Kinect is designed for gaming consoles that consist of depth sensing capabilities using structure light and triangular 3D scanner principles [118]. Table 2 - 3 summarizes some specifications of Kinect that are relevant to 3D body contour acquisition for spinal brace manufacturing. Depth and colour images can be capture up to frame rate of 30 fps, with colour point cloud containing about 300,000 points in every frame [119]. An advantage of Kinect is that the capture of 3D data is not affected by lighting condition with its infrared projector and monochrome sensor [120]. However, additional calibration is required because inaccuracy for depth measurements can be caused by heat and vibration after transportation or drift of infrared laser which results in noisy images [118]. Distance between sensor and surface of the object as well as orientation of object surface relative to sensor can also cause part of the object to be occluded affecting 3D contour accuracy [119]. Study also showed that random error of depth measurements increase and depth resolution decrease with object further away from Kinect sensor [119]. Lastly, smooth and glossy surfaces capture with Kinect can cause overexposure that lead to gap in the point cloud image [119]. Kinect has been used in many rehabilitation applications with its 3D motion capture capability [120].

2.8.2.2. Rodin4D Structure Sensor

Rodin4D structure sensor uses the 3D Structure Sensor (Occipital Inc., San Francisco, USA) for depth sensing, Captevia application to generate and save 3D scan file and Rodin4D Neo rectification software for modifying scanned body shape [121]. The structure sensor is an accessory mounted on an iPad based on structure light technology with the advantage of a mobile device with no chords attached and wireless communication [122]. The frame rate is either 30 or 60 fps and operates optimally at a temperature between 0 to 35 degree Celsius [123]. The structure sensor attached can also be use in other applications such as virtual reality headset, indoor measurements, and motion tracking beside 3D scanning [124] . Table 2 - 3 summarizes some specifications of the Rodin4D structure sensor.

2.8.2.3. Vorum 3D Spectra Scanner

Vorum 3D Spectra scanner is a handheld structure light 3D scanner specifically designed for obtaining body shape in prosthetics and orthotics applications [125], [126]. 3D body shape generated can be modified with CanFit customized software. Limited technical specifications or articles were found from literature review from this scanner. Table 2 - 3 summarizes the resolution and features of the Vorum Spectra 3D scanner.

Table 2 - 3 Specifications of Microsoft Kinect, Rodin4D Structure Sensor and Vorum Spectra Scanner

3D scanner	Range	Accuracy	Depth sensor resolution	Cost	Features
Microsoft Kinect	0.8-4 m [120]	A few millimeter range up to 4 cm [119]	640 × 480 pixels [119]	About $300 CAD [127]	Infrared projector and camera, colour camera, 3D motion capture, facial and voice recognition capabilities [118]
Rodin4D Structure Sensor	0.4-3.5 m [123]	0.5 mm at 40 cm and 30 mm at 3 m [123]	640 × 480 pixels [128]	About $400 CAD [129]	Infrared projector with uniform infrared LEDs, attachment to mobile device with battery life for 3-4 hours of active sensing [123]
Vorum Spectra Scanner	N/A	0.1 mm resolution [126]	N/A	N/A	Blue light projector with a single camera to capture 3D image [126]

N/A indicates information not available through literature review

Chapter 3: Investigation of Appropriate Parameters for 3D Printing a Spinal Brace

Chapter 2 begins with section 3.1. describing the investigation of appropriate 3D printing configurations for manufacturing spinal braces. This includes comparison of different 3D printing methods, 3D printers and 3D printing orientations. Section 3.2. describes the investigation of the optimal 3D printed brace material and thickness through comparison of mechanical properties of tensile test specimens. Following that, section 3.3. describes the evaluation of modifiability, attachment of accessories, flexibility, manufacturing time, cost, breakage safety, weight and durability of prototype 3D printed spinal braces for establishing feasibility.

3.1. Investigation of Appropriate 3D Printing Configurations for Manufacturing Spinal Braces

3.1.1. Comparison of 3D Printing Methods

Three-Dimensional Printing (3D-P) uses a liquid binder to glue together starch based powder to form a layer for building a part. It was excluded in the comparison of different 3D printing methods for manufacturing a spinal brace. That's because 3D-P materials are rigid and lack flexibility and elongation properties [130]. The other four 3D printing methods: Stereo-Lithography (SLA), Fused Deposition Modeling (FDM), Polyjet and Selective Laser Sintering (SLS) are more suitable to print thermoplastic materials that are commonly used for orthotics applications. SLA uses a laser to selectively solidify a liquid resin layer in a vat resin bath to form a part. FDM melts solid filament and extrudes it out a nozzle to form a layer. Polyjet uses inkjet technology to deposit a liquid photopolymer resin layer and immediately cures the layer with UV lamps. SLS selectively solidifies a powder bed layer with laser. In the market, there are many 3D printers commercially available for the four aforementioned printing methods.

A small scale 3D printer was considered for creating a 3D printed brace by joining multiple pieces together. However, a printed brace is customized to each patient and the addition of customized locking mechanisms for each brace can be time consuming. Furthermore, the design of locking mechanisms with adequate structural integrity and stiffness at jointing

regions for holding spinal curvatures can be challenging. Therefore, a one-piece brace printing with a larger scale 3D printer was preferable. Build volume was used to narrow down printer options. Printers with build volume close to (508 x 254 x 331) mm or (20 x 10 x 13) inches for an average adolescent scoliosis brace are ideal for printing a brace in one piece. Large scale 3D printer options are shown in Table 3 - 1.

Selection criteria of a suitable printing method for a spinal brace are a) range of material properties, b) cost of machines and printed materials, c) number of printing materials, d) printing accuracy, and e) post-processing procedures. A printing method that can produce parts with a wider range of material properties is important. That's because most printing method produce rigid parts, but a spinal brace requires material with both flexibility for donning and doffing as well as rigidity for holding spinal curvature. Lower cost machines and printing materials are necessary to provide a cost-effective alternative to the traditional brace. As for the number of printing materials, a larger number of printing material corresponds with a larger variety of material properties for furthermore mechanical testing in selecting suitable printing material for a spinal brace. An adequate printing accuracy is important in manufacturing a customized brace shape to provide comfortable fit and acceptable in-brace corrections for patients. Lastly, with fewer post-processing procedures, the brace manufacturing process will be less time consuming and labour intensive.

As Table 3 - 1 indicates, all four printing methods provide sufficient accuracy to print a spinal brace with clinical acceptable accuracy in the 1 cm range. Polyjet and FDM methods provide wider range of material properties, support more printed materials and require less post-processing time. At the same time, FDM machines are relatively less expensive than the Polyjet system with similar build volume. Also, the material cost for FDM are cheaper compared with SLA, Polyjet and SLS in general [131], [132] . Therefore, FDM printing method is the recommended approach for the orthotic application.

Table 3 - 1 Characteristics of 3D printer with different printing methods (Information gathered from respective manufacturers and 3D printer resellers Javelin Technologies Inc. and 3D Revolution Technologies Inc.)

Manufacturer	Stratasys			3D Systems				Rodin4D	WASP		AON 3D
3D Printer	ObJet 1000	FORTUS 450	FORTUS 900	ProJet MJP 5600	ProJet 7000	ProXSLS 500	sPro60 HD-HS	Rodin4D	Delta WASP 40-70	Delta WASP 40-70 Industrial	AON-M2
3D Printing Method	Polyjet	FDM	FDM	Polyjet	SLA	SLS	SLS	FDM	FDM	FDM	FDM
Build Volume (X · Y · Z)cm³	(99.8 x 79.7 x 49.7)	(40.6 x 35.5 x 40.6)	(91.4 x 60.9 x 91.4)	(51.8 x 38.1 x 29.9)	(38.1 x 38.1 x 25.4)	(38.1 x 33.0 x 45.7)	(38.1 x 33.0 x 45.7)	39.8 cm diameter base, 59.9 cm height	39.8 cm diameter base, 66.8 cm height	39.8 cm diameter base, 69.8 cm height	(45.5 x 45.5 x 63.5)
Material Properties	Wide range (flexible and rigid)	Wide range (flexible and rigid)	Wide range (flexible and rigid)	Wide range (flexible and rigid)	Mostly rigid	Mostly rigid	Wide range (flexible and rigid)	N/A	N/A	N/A	N/A
Material Selection	Blend material available	11	12	Blend material available	9	6	8	N/A	5	10	6
Post-Processing	Waterjet support	Breakaway and soluble support	Breakaway and soluble support	Steam, Bath, wash	Bath, UV Cure	Cooling, Vacuum, blast	Cooling, Vacuum, blast	Break away	Break away	Break away	Break away
Accuracy	0.6 mm	0.127mm	0.089 mm	0.025-0.05 mm/ 25.4 mm	0.045 mm	0.08-0.15mm	0.08-0.15 mm	N/A	>0.4 mm	>0.4 mm	>0.25m m
Machine cost (USD)	$750K	$200K	$500K	$222K	$292K	$341K	$523K	N/A	$10K	$13K	$30K

N/A indicates no information available from manufacturer

3.1.2. Evaluation of 3D Printers for FDM Printing

A decision matrix (Table 3 - 2, Table 3 - 3, Table 3 - 4) was used for selecting a suitable 3D printer among the FDM 3D printer options in Table 3 - 1. Table 3 - 2 reported the weighting and scoring scale for evaluation of 3D printers according to requirements in scoliosis brace application. Certainty referred to the reputation of the printer manufacturer, as well as support, maintenance, specifications and printer availabilities. Table 3 - 3 reported the scores of printers at each category based on characteristics from Table 3 - 1. After that, scores obtained from each category were multiplied by weightings for each category to calculate the final score. As shown in Table 3 - 4, the three printers with highest scores were DeltaWASP 40-70 Industrial (Score 178), FORTUS 450mc (Score 207), and FORTUS 900mc (Score 214). The printer with the highest score was FORTUS 900mc (Stratasys Ltd., Minnesota, USA). FORTUS 900mc was the 3D printer recommended and it is one of the machines that could potentially be used for printing a spinal brace.

Table 3 - 2 Weighting and scoring scale for evaluation criteria of 3D printers

Weighting Scale	
5	Must have
3 to 4	Should have
1 to 2	Nice to have
Weighting of Requirements	
Build Volume	5
Material Properties	5
Cost of Machine and Materials	4
Certainty	4
Material Selection	3
Accuracy	3
Post-Processing	3
Score in 1-10 Scale	
9 to 10	Meet project requirement
7 to 8	
5 to 6	
3 to 4	
1 to 2	Does not meet project requirement

Table 3 - 3 Scores of different 3D printers at each evaluation criteria

3D Printers	Build Volume	Material Properties	Material Selection	Accuracy	Post-process	Cost of Machine & Material	Machine Cost (USD)	Cert-ainty
A: FORTUS 450	7	8	8	9	7	6	$200K	9
B: FORTUS 900	10	8	9	10	7	2	$500K	9
C: Rodin4D	8	3	5	5	10	5	No Response	3
D: Delta WASP 40-70	8	3	5	5	10	10	$10K	5
E: Delta WASP 40-70 Industrial	8	3	6	5	10	10	$13K	5
F: AON-M2	10	3	6	5	7	9	$30K	4

Table 3 - 4 Weighted scores of different 3D printers at each evaluation criteria

3D Printers	Build Volume	Material Properties	Material Selection	Accuracy	Post-process	Cost of Machine & Material	Certainty	Total
A: FORTUS 900	50	40	27	30	21	8	36	**214**
B: FORTUS 450	35	40	24	27	21	24	36	207
C: Rodin4D	40	15	15	15	30	20	12	147
D: Delta WASP 40-70	40	15	15	15	30	40	20	175
E: Delta WASP 40-70 Industrial	40	15	18	15	30	40	20	178
F: AON-M2	50	15	18	15	21	36	16	171

3.1.3. Evaluation of 3D Printing Orientations

Since FDM created parts are anisotropic therefore the material properties of the 3D printed objects are dependent on print orientation, the print orientation with the best material properties is optimal. Mechanical testing of standard test specimens is used to obtain material properties. The three print orientations of test specimens are side (on-edge), flat and upright as shown in Figure 3 - 1 (a), (b) and (c) respectively. Standard test specimens are typically loaded up to break point to evaluate strength. Theoretically, based on the loading direction of standard test specimens as shown in Figure 3 - 1 (d), (e) and (f), upright print orientation has the lowest strength while on-edge and flat print orientations have comparable strengths. Upright printed specimens will break by separation of layers with the loading direction while specimens printed on-edge or flat will break by separation of the strains of filament. Upright orientation is weaker than the other two orientations because the bonding strength of each layer is weaker than the strength of continuous strains of filament in the loading direction.
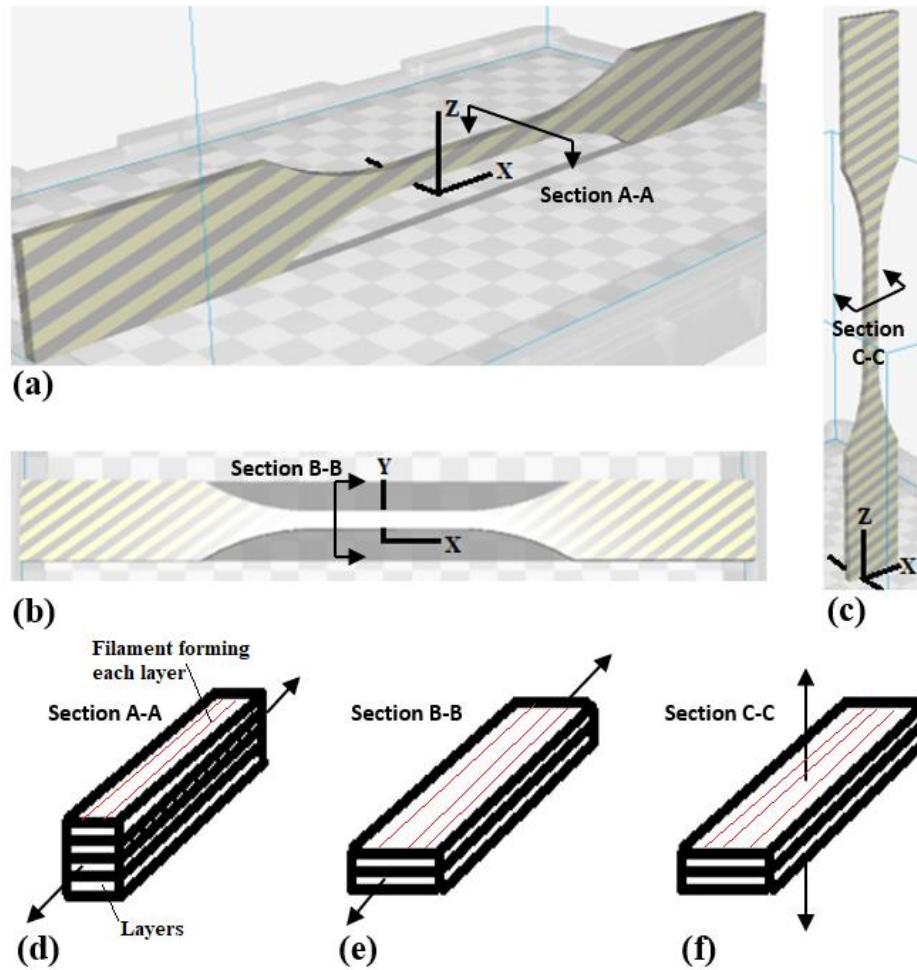
Figure 3 - 1 Print orientations of test specimens. (a) On-edge (X-Z plane) orientation. b) Flat (X-Y plane) orientation. (c) Upright (Z-X) orientation. (d) Cross section A-A displaying printed layers and loading direction. e) Cross section B-B displaying printed layers and loading direction. f) Cross section C-C displaying printed layers and loading direction.

Material properties of printing materials from FORTUS 900mc has shown generally better strength and elongation in side (on-edge) print orientation from manufacturer data sheet. Also, test specimens printed in side orientation with longitudinal edges as the bottom layer is most similar as printing a spinal brace from bottom to top in an upright position as shown in Figure 3 - 2. In addition, the loading direction while opening a brace printed in upright position is similar with loading direction of a standard test specimens printed in side orientation. Therefore, the superior material properties of test specimens printed in side orientation found from the manufacturer corresponds with better material properties printing a spinal brace in upright position. Furthermore, printing a spinal brace in upright position reduce support material, printing and post-processing time shown in estimation from pre-print Insight software. Therefore, upright position is the most appropriate orientation for printing a spinal brace.
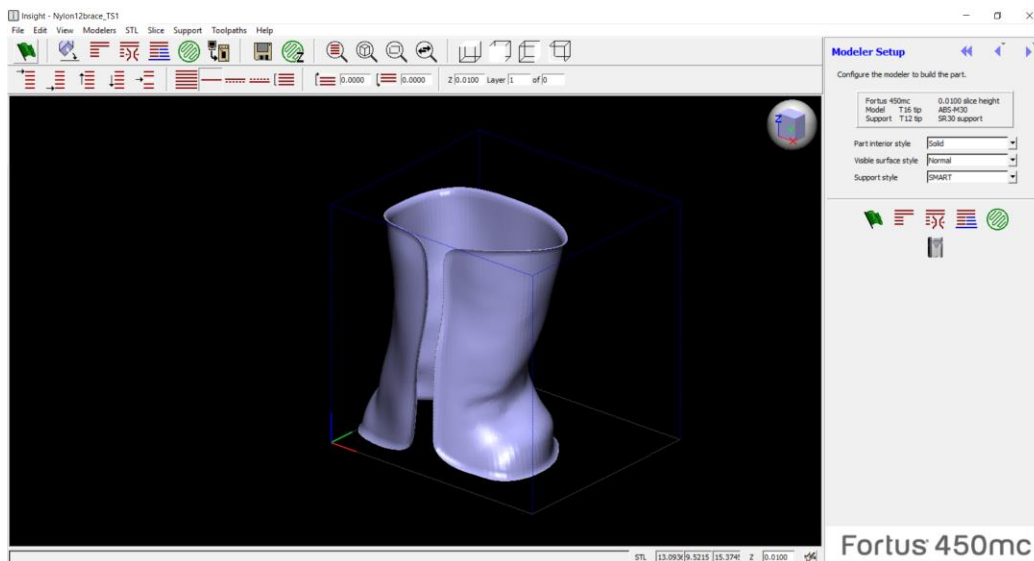
Figure 3 - 2 Graphic interface of a spinal brace print in upright position from Insight software of FORTUS 900mc printer.

3.2. An Experimental Study to Investigate Appropriate Material and Thickness for a 3D Printed Brace[*]

3.2.1. Introduction

A spinal brace is generally described as a rigid plastic jacket which is customized to patient torso and typically made of thermoplastics such as polypropylene. Its thickness is normally between 4 to 5 mm. According to clinical information, a spinal brace is shown to be durable and able to last for more than 2 years even though patients are donning and doffing their braces a few times per day.

Recently, 3D printed spinal braces have become commercially available. A company (UNYQ, San Francisco, USA) had printed braces in 3.5 mm thickness with polyamide type of material. While another company (WASP, Ravenna, Italy) had printed braces with PLA material. However, there are no literature reports on how the companies select the material and thickness for the 3D printed scoliosis brace or evaluation of the mechanical properties of these commercially available braces. Evaluation of mechanical properties such as strength and flexibility of 3D printed brace can ensure structure integrity as well as potentially improving brace wear comfortability.

The objectives of this study were to evaluate the mechanical properties of different potential 3D printed materials and to determine the appropriate material and thickness for spinal braces.

3.2.2. Selection of Testing Materials and Specimen Geometry

From section 3.1, FORTUS 900mc was the printer selected for fabricating a spinal brace. This machine supported 11 printed materials including PC-ISO, ULTEM9085, ULTEM1010, Nylon12, Carbon-fiber reinforced Nylon12, ASA, PC-ABS, ABS-M30, ABS-M30i, ABS-ESD7 and polycarbonate (PC). Table 3 - 5 summarized the material properties and the support material characteristics relevant to brace structural integrity and manufacturing. Among the 11 materials, only ULTEM1010 and Nylon12 were selected for this study. ULTEM1010 was the strongest and stiffest material which had a higher yield

[*] Materials in this section were included in a submitted manuscript: K. Ng, K. Duke, and E. Lou, "Evaluation of Mechanical Properties on Potential 3D Printed Materials for Spinal Braces," *Addit. Manuf.*, 2018.

strength, ultimate tensile strength and Young's Modulus compared with the standard brace material, polypropylene. Nylon12 had the closest material properties as polypropylene in term of yield strength, Young's Modulus and tensile elongation at yield. To compare the mechanical properties of ULTEM1010, Nylon12 and polypropylene, these 3 materials were all prepared as type II geometry specimens according to ASTM D638-14 Standard [134]. All specimens had length, width and a gauge length width of 25.8 cm, 2.8 cm and 0.6 cm, respectively. Three different thicknesses, 2.5 mm, 3.25 mm and 4 mm were tested with ULTEM1010 and Nylon12, but only 4 mm was tested for polypropylene as it was close to the standard brace thickness. Furthermore, the tested specimens had longer and wider grip handles to provide more contact area with the testing grips to ensure the breakage area was within the narrow section instead of the gripping region.

Table 3 - 5 Material properties and specifications from manufacturers for polypropylene and 11 different 3D printing materials in side build orientation

Material properties and specifications	Polypropylene	PC-ISO	ULTEM9085	ULTEM1010	Nylon12	Carbon-Fiber Reinforced Nylon12
Yield Strength (MPa)	33	N/A	47	64	32	63
Ultimate Tensile Strength (MPa)	33	57	69	81	46	76
Young's Modulus (MPa)	1400	2000	2150	2770	1282	7515
Tensile Elongation at Yield (%)	8.0	N/A	2.2	2.2	2.4	0.9
Support Material Removal	No support needed	Breakaway	Breakaway	Breakaway	Soluble	Soluble

N/A   Indicates no manufacturer data available

Material properties and specifications	ASA	PC-ABS	ABS-M30	ABS-M30i	ABS-ESD7	PC
Yield Strength (MPa)	29	41	31	N/A	N/A	40
Tensile Strength (MPa)	33	N/A	32	36	36	57
Young's Modulus (MPa)	2010	1900	2230	2400	2400	1944
Tensile Elongation at Yield (%)	2.0	N/A	2.0	N/A	N/A	2.2
Support Material Removal	Soluble	Soluble	Soluble	Soluble	Soluble	Breakaway/Soluble

N/A   Indicates no manufacturer data available

3.2.3. Tensile Test Experiment

A MTS 810 Material Testing System Model 318.10 (MTS Systems Corporation, Minnesota, USA) was used to perform tensile tests. This testing system included hydraulic lift and locks, hydraulic actuator, a 10 N range load cell and control system as shown in Figure 3 - 3. A pair of custom grips were designed and built with serrations for soft specimens to ensure no slippage during experiments. For strain measurement, a MTS 634.12E-24 axial extensometer (MTS Systems Corporation, Minnesota, USA) was used. The extensometer had a gauge length of 2.54 cm and a maximum travel of 1.27 cm, corresponding to a maximum of 50% strain measurement. The accuracy of the extensometer also met or exceeded ASTM E83 Class B1 and ISO9513 Class 05 standards with low hysteresis and activation forces.

Among the 3 tested materials, a total of 31 specimens were tested which included 13 specimens of ULTEM1010, 13 specimens of Nylon12 and 5 specimens of polypropylene. Within the 13 specimens of ULTEM1010 and Nylon12, there were 4, 5, and 4 specimens for 2.5 mm, 3.25 mm and 4 mm thickness, respectively. Multiple experiments with the same thickness were to confirm reliability and accuracy. In addition, these anisotropic ULTEM1010 and Nylon12 specimens were printed in side orientation as this print orientation was equivalent to printing a brace in an upright position that might provide optimal strength and elongation based on the manufacturer data sheet [135]. On another note, all polypropylene specimens were machined from a standard polypropylene sheet (4 mm thick). The width and thickness at gauge length were measured with a Vernier caliper (Mitutoyo, Japan) with accuracy of ±0.02mm.

(a)   (b)   (c)

(d)
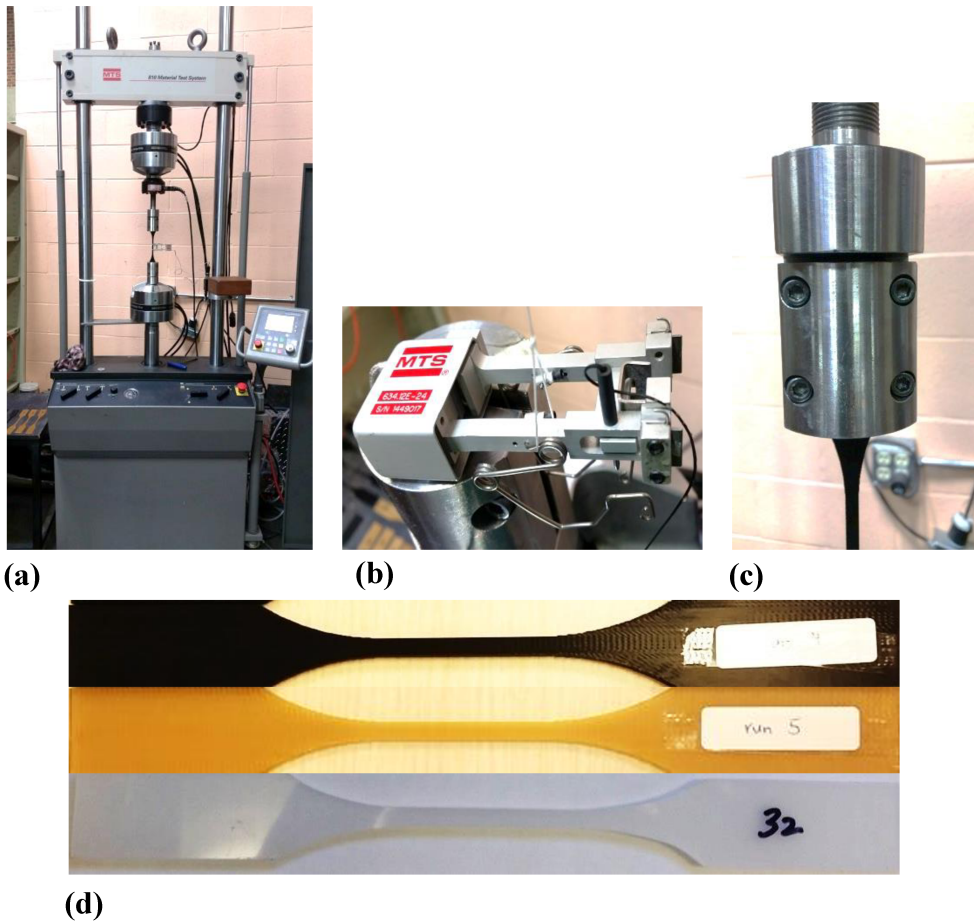
Figure 3 - 3 Tensile testing equipment and specimens. (a) MTS 810 Material Testing System Model 318.10. (b) MTS 634.12E-24 axial extensometer. (c) Custom grip. (d) Golden (run 5) ULTEM1010, black Nylon12 and white polypropylene test specimens.

All specimens were randomly selected for testing and the procedures were: 1) clamped the specimen with top and bottom grips, 2) zeroed the preload forces on the specimen from tightening, 3) mounted extensometer onto specimen at gauge length, 4) zeroed initial strain measurement from mounting and disengaging of locking mechanism, and 5) applied loads to specimens with loading rates of 5 mm/min, 10 mm/min, and 25 mm/min for ULTEM1010, Nylon12, and polypropylene, respectively. These loading rates would allow breakage of specimen within 0.5-5 minutes according to ASTM D638-14 standard. Sampling frequency was 15 Hz for both Nylon12 and polypropylene and 30 Hz for ULTEM1010. Higher sampling frequency was used for ULTEM1010 because ULTEM1010 is not ductile which should break earlier with less elongation. Therefore, more sample points were acquired for adequate depiction of general tread of stress strain

and force displacement curves to obtain mechanical properties. Lower sampling frequency was used for Nylon12 and polypropylene to reduce data storage because a longer time of elongation was expected before they broke.

3.2.4. Data Processing

Force (N) generated from the actuator, strain (mm/mm) from strain gauge, stroke displacement (mm) from the material testing system and time (s) were parameters acquired for processing. Stress-strain and force-displacement curves for obtaining mechanical properties were plotted. Stress for plotting stress-strain curve is defined as

$$\sigma = \frac{F}{A} \tag{3 - 1}$$

where σ is the stress level at the breakage region (MPa), F is the applied load (N), and A is the cross-sectional area of the breakage region at gauge length (mm^2).

Displacement at gauge length for plotting force displacement curve is defined as

$$D = l - l_0 = \epsilon \cdot l_0 \tag{3 - 2}$$

where D is the displacement of the specimen at gauge length (mm), l is the final length of extensometer (mm), l_0 is the initial length of extensometer (mm) which is 2.54 cm for a MTS 634.12E-24 axial extensometer and ϵ is the strain at gauge length in (mm/mm). With known initial length of extensometer and the recorded strain at gauge length, displacement at gauge length was calculated at each time point.

Custom MATLAB programs were developed to automate data processing by plotting stress strain and force displacement curves. The mechanical properties a) 0.2% offset yield strength (MPa) and b) strain to yield at 0.2% offset (%) were obtained by identifying the yield point. On the stress strain graph, the yield point was obtained by drawing a linear line from zero stress and 0.2% strain position parallel to the stress strain curve. The first intersection point of the linear parallel line and the stress strain curve was the yield point. This method followed ISO 527-1 standard [136] and it was the recommended practice from

literature [137]. After that, c) ultimate tensile strength (MPa), d) strain to break (%), e) yield stress (MPa), f) strain to yield (%), g) Modulus of Elasticity (MPa), and h) toughness (MJ/m^3) were also extracted from the stress strain curves. Furthermore, i) maximum force (N), j) yield force (N), k) displacement at gauge length to break (mm) and l) stiffness (N/mm), which is the initial linear slope, were obtained from force displacement curves. Furthermore, force stroke-displacement curves representing the overall mechanical properties characteristics were compared among all test groups.

Statistical analysis was performed using IBM SPSS version 19.0 and Microsoft Excel 2016. Standard deviation and probability value were found using Excel. Analysis of Variance (ANOVA) was performed using SPSS statistical software package. Seven "One way between subjects ANOVA" comparisons representing each test group which means 3 ULTEM1010 (different thickness), 3 Nylon12 (different thickness), and 1 polypropylene group were analyzed between experimental and manufacturer data in mechanical properties a) to d) and g) described above. Another "One way between subjects ANOVA" was analyzed between all seven test groups. In particular, multiple comparison analyzes were conducted to compare polypropylene and 2.5 mm Nylon12 groups with the other test groups. The dependent variables for these comparisons were mechanical properties described above from i) to l). Next, a "Two way between subject ANOVA" was analyzed with materials and thickness as independent variables while the 6 dependent variables were mechanical properties a), g) and i) to l). 95% confidence intervals and effect sizes were also reported. Independent of error, normality and homogeneity of variance assumptions were checked.

The material properties from experimental results of the 2 selected printing materials, ULTEM1010, Nylon12, were compared with their corresponding manufacturer data. The difference between the averages of 4 specimens' experimental results with the manufacturer data was calculated. Furthermore, the experimental stiffness was also compared with the theoretical axial stiffness which was calculated by the following equation:

$$\mathbf{k} = \frac{\mathbf{AE}}{\mathbf{L}}$$
[3 - 3]

Where k is the theoretical axial stiffness at gauge length in (N/mm), A is the estimate cross sectional area of specimen at gauge length in (mm^2), E is the Modulus of Elasticity (MPa), and L is the gauge length in (mm). To evaluate these two materials along with the traditional brace material, polypropylene, 4 mm thickness groups were used.

3.2.5. Results

The experimental mechanical properties of the 3 tested materials and thicknesses were summarized in Table 3 - 6. Mechanical properties were used for determining the appropriate material and thickness for a brace because mechanical properties depend on both material and thickness. Comparing the three materials with the same 4 mm thickness, ULTEM1010 showed highest stiffness followed by polypropylene and then Nylon12. All ULTEM1010 thicknesses showed higher stiffness than polypropylene and all Nylon12 thicknesses showed lower stiffness than polypropylene. The greatest stiffness differences between test groups and 4 mm polypropylene brace material are 4 mm ULTEM1010 with 109.6% higher stiffness and 2.5 mm Nylon12 with 44.1% lower stiffness. Stiffness data had low standard deviations demonstrating consistent results.

Break force for all groups were larger than polypropylene except for 2.5 mm Nylon12 that was 8.6% lower. 3.25mm Nylon12 had a 22.3% higher break force than polypropylene. Consistent break force for all groups was demonstrated by low standard deviation. Yield force was higher for all groups compared with polypropylene. 2.5 mm and 3.25 mm Nylon12 had a 34.3% and 74.8% higher yield force compared to polypropylene respectively. Standard deviations for all groups were between low to moderate, indicating reasonable consistency in yield force. Comparing the three materials with the same 4 mm thickness, ULTEM1010 had the highest break and yield force followed by Nylon12 and then polypropylene.

Force stroke-displacement curves representing an average of specimen for each test group were shown in Figure 3 - 4. Force represents the applied load and stroke displacement represents how much the entire specimen had been stretched. The ULTEM1010 groups could withstand higher force but they could not elongate as much. On the other hand, Nylon12 groups could only withstand lower force similar with polypropylene but they could elongate much more, with displacement close to polypropylene. Polypropylene force

56

stroke-displacement curve lies between 2.5 mm and 3.25 mm Nylon12 group. Polypropylene curve had a general trend with closest resemblance with the two groups.

Tale 3 - 6 Mechanical properties of three materials at 2.5mm-4mm thickness

Materials		Nylon12			ULTEM1010			PP
Design Thickness (mm)		2.50	3.25	4.00	2.50	3.25	4.00	4.00
Mechanical Properties	Stiffness	Mean ± SD (N/mm)						
		722 ± 10	941 ± 12	1131 ± 41	1723 ± 37	2271 ± 49	2706 ± 41	1291 ± 118
		Percent Difference from Polypropylene (%)						
		44.1	27.1	12.4	33.4	75.9	109.6	N/A
		95% Confidence Interval (N/mm)						
		706-738	929-961	1066-1197	1663-1782	2228-2347	2641-2771	1072-1504
	Break force	Mean ± SD (N)						
		680 ± 9	909 ± 11	1064 ± 15	1466 ± 32	1816 ± 37	1639 ± 233	744 ± 16
		Percent Difference from Polypropylene (%)						
		8.6	22.3	43.0	97.1	144.2	120.3	N/A
		95% Confidence Interval (N)						
		666-694	888-929	1039-1088	1415-1516	1774-1828	1268-2009	716-774
	Yield Force	Mean ± SD (N)						
		492 ± 9	641 ± 40	720 ± 103	774 ± 56	871 ± 89	901 ± 134	367 ± 23
		Percent Difference from Polypropylene (%)						
		34.3	74.8	96.4	111.1	137.6	145.9	N/A
		95% Confidence Interval (N)						
		479-506	577-680	556-884	684-864	746-931	688-1115	331-387

N/A   Indicates no manufacturer data available
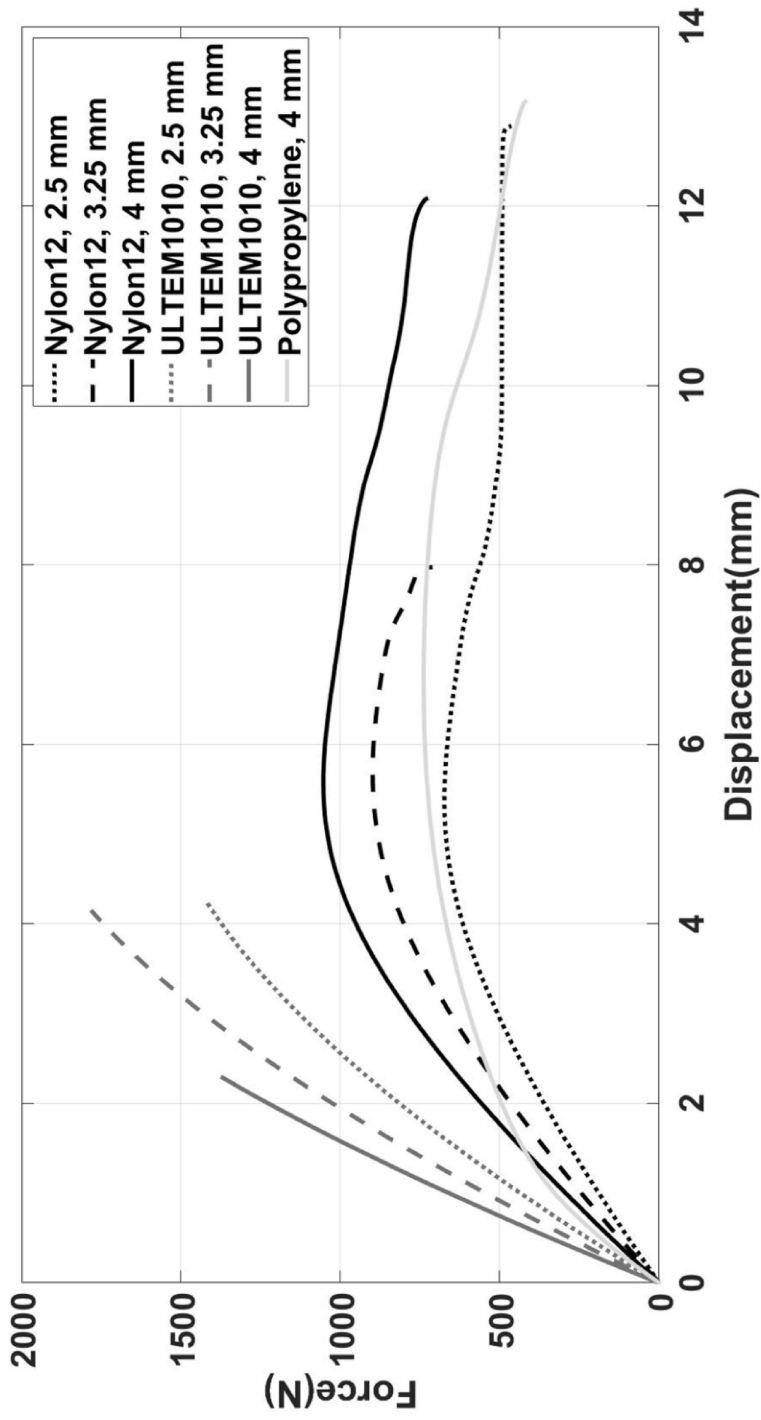
Figure 3 - 4 General trends of force displacement curves representing an average of specimens for each test group.

59

Validation showed small percent differences between experiment and manufacturer data for ultimate tensile strength, and Modulus of Elasticity as shown in Table 3 - 7. However, percent differences were higher for strain to yield at 0.2% offset, 0.2% offset yield strength and strain to break at gauge. The smallest percent difference was 1.3% for Nylon12 ultimate tensile strength and largest percent difference was 79.8% for polypropylene strain to yield at 0.2% offset. Experimental and calculated theoretical stiffness were close to identical as shown in Figure 3 - 5. Linear regression lines were also generated in predicting changes in stiffness for 2.5 - 4 mm range with an R squared value close to 1. This indicated a strong linear trend for stiffness with change in thickness.

Table 3 - 7 Experimental and manufacturer data for material properties of three materials

Mechanical properties	Materials	Experiment (MPa)	Manufacturer (MPa)	Percent Difference (%)
		Mean ± SD	Mean Data	
Ultimate Tensile Strength	U	70.0 ± 10.1	81	13.5
	N	46.6 ± 0.6	46	1.3
	P	35.9 ± 0.6	N/A	N/A
Modulus of Elasticity	U	2864 ± 54	2770	3.4
	N	1261 ± 19	1282	1.7
	P	1520 ± 145	1400	8.6
Strain to yield at 0.2% offset	U	2.5 ± 0.2	2.2	15.2
	N	3.2 ± 0.1	2.4	32.3
	P	1.6 ± 0.1	8.0	79.8
Strain to break at gauge	U	2.8 ± 0.6	3.3	16.7
	N	27.1 ± 19.3	30.0	9.8
	P	35.9 ± 15.8	N/A	N/A
0.2% Offset Yield Strength	U	67.2 ± 3.2	64.0	5.0
	N	37.3 ± 0.9	32.0	16.5
	P	21.2 ± 1.1	33.0	35.6

U   ULTEM1010

N   Nylon12

P   Polypropylene

N/A   Indicates no manufacturer data available
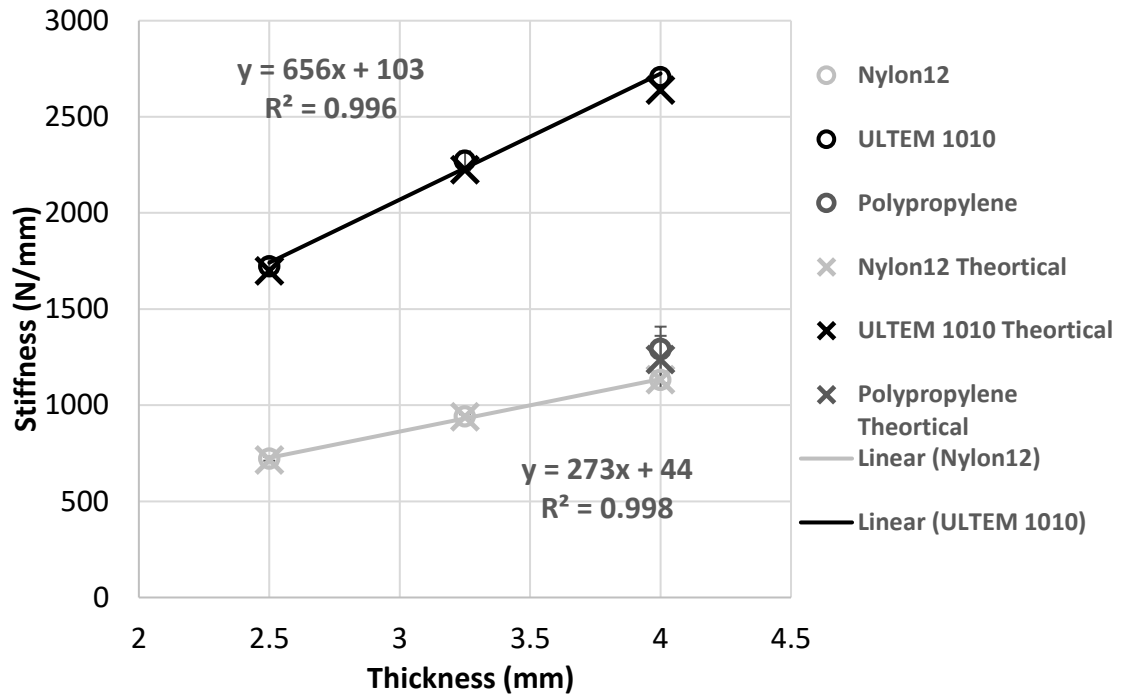
Figure 3 - 5 Experimental and theoretical stiffness of three materials at 2.5 mm to 4 mm thickness.

3.2.6. Discussions

Stiffness for the different material and thickness test groups was important to evaluate. That's because lower brace stiffness corresponds to the ease of daily donning and doffing of the brace for patients. 2.5 mm Nylon12 is ideal since it has the lowest stiffness. Nevertheless, there was an initial concern of whether lower stiffness than the traditional polypropylene brace material will cause significant material deformation when the torso contacts the brace. That's because a less stiff material tends to deform easier with force applied. In that case, the brace shape will not hold spinal curvature as intended. This concern was dismissed after finding that the brace interface pressure with the torso causes insignificant deformation on the brace material. This was demonstrated by a study showing that the highest interface pressure between the brace and patient torso was only 12 ± 7 kPa for a Boston brace [138] as opposed to the mega-Pascal stress level needed to cause any significant deformation for the tested materials from stress strain curves.

The 2.5 and 3.25 mm Nylon12 had similar or better break and yield force than the 4 mm polypropylene brace material from Table 3 - 6. Also, the force stroke-displacement curves of 2.5 mm and 3.25 mm Nylon12 had the closest proximity with the standard 4 mm polypropylene according to Figure 3 - 4. Both points demonstrate 2.5 and 3.25 mm Nylon12 had similar strength and ductility as 4 mm polypropylene.

Validation was conducted by comparing material properties between experimental results and manufacturer data. A higher percent difference was found between the experimental result and manufacturer data for strain to yield and yield strength. This was likely due to manufacturer not using the recommended 0.2% offset strain method in identifying the yield point.

Literature review was also conducted to compare experimental results with studies investigating material properties of 3D printed materials. Studies were found on similar testing of 3D printed materials [139], [140]. The objective of these studies was to understand the effect of printing setup such as layer height, percent infill, print orientation, laser power, laser speed, scan spacing, build orientation, and position on material properties [139], [140]. Material properties such as modulus of elasticity, yield strength, ultimate tensile strength and fracture strain were found for laser-sintered Nylon12 [6]. The material properties of the FDM printed Nylon12 from the current experimental results were within range of the material properties of the laser-sintered Nylon12 reported by Starr [6]. In the field of orthotics, preliminary study using 3D scanning and printing method for creating foot/ankle braces had been conducted, but material properties were not investigated [111].

Some limitations of this study included breakages outside of gauge length for some specimens and small sample size. Firstly, all specimens tested were broken within the narrow region where cross-sectional area was constant, but some specimens did not break within the shorter gauge length where the extensometer was mounted. A reason was printing imperfections that led to higher stress concentrations especially at the transition between the neck to grip region of the test specimen. Another reason was stress concentrations created by mounting the extensometer on specimens. Also, Nylon12 and polypropylene specimens could stretch beyond the maximum extensometer range. This limitation caused inaccuracy in strain to break results, but all mechanical properties at the

elastic region were not affected. Future study could simulate brace with finite element analysis (FEA) to understand the stress distribution of the entire brace while opening. This analysis will enable further optimization of brace design for creating a more lightweight and breathable brace by removing material at low stress regions where materials are not needed structurally.

3.2.7. Conclusion

In conclusion, this study investigated the mechanical properties of ULTEM1010 and Nylon12 3D printed materials. Based on greater flexibility than traditional polypropylene for donning and doffing of the brace, as well as similar strength and ductility with traditional polypropylene, Nylon12, 2.5-3.25 mm is an appropriate material and thickness for a 3D printed spinal brace.

In this experiment, each test groups had 4 or 5 specimens tested. Due to the small sample size in each test groups, ANOVA results were not included in this study. Furthermore, the next study on validating the durability and structure integrity of the 3D printed prototype braces was initiated due to the test specimens' small sample size and the unique geometry of the brace.

3.3. A Study to Evaluate and Validate the Durability of ULTEM1010 and Nylon12 3D Printed Prototype Braces[*]

3.3.1. 3D Printed Braces Evaluation Procedures

A body shape file from previous surface topography scan of a female scoliotic volunteer was used to print two full scale spinal braces with 2.54 mm thickness using ULTEM1010 and Nylon12 materials. The printed thickness was based on orthotists preferences by trying a thinner brace. It was hypothesized that patients might feel more comfortable with a thinner brace as it is lighter, more breathable and lower profile. To evaluate the 3D printed braces, the following assessment such as a) brace shape modification possibility with heat,

---

[*]Materials in this section were included in a submitted manuscript: K. Ng, K. Duke, and E. Lou, "Evaluation of Mechanical Properties on Potential 3D Printed Materials for Spinal Braces," *Addit. Manuf.*, 2018.

b) buckles and liners attachment feasibility, c) brace break safety, d) brace flexibility for donning and doffing during daily activities e) production time, f) labor and material costs, and g) final weight of a same shaped brace were compared with the same subject's traditional brace. Furthermore, the brace gap distances at the anterior opening after simulated donning and doffing were also measured to assess if any plastic deformation occur over time. Five repeated measurements of the brace gap distance were conducted using a Vernier caliper (Mitutoyo, Japan) with accuracy of ±0.02 mm at the locations approximately 1/3 below the top edge of the brace, middle of the brace and 1/3 above the bottom edge of the brace. These measurements were recorded every 372 times of donning and doffing which simulates 3 months of brace wear.

3.3.2. Results

Figure 3 - 6 (a) and Figure 3 - 6 (b) showed the 3D printed braces using UTEM1010 and Nylon12 materials, respectively. Figure 3 - 6 (c) illustrated the 3D printed braces after evaluation. Both printed braces were able to adjust brace shape after heating ULTEM1010 and Nylon12 to their respective glass transition temperatures at about 215°C and 190°C, respectively. Strap buckles and brace liners were added using the standard method without fracturing the brace. While an orthotist used a plier to apply a huge force at the corner of both printed braces, ULTEM1010 cracked with a sharp edge, but Nylon12 was gently torn off from the brace. This demonstrated ULTEM1010 had a higher energy and brittle fracture as opposed to Nylon12 exhibiting ductile elongation before delamination of the layers with excessive bending. Furthermore, when open and close procedure were performed for both printed braces to simulate donning and doffing, Nylon12 brace showed more flexibility while retaining structural integrity after 2920 times of open and close procedure. However, ULTEM1010 brace cannot elongate as much as Nylon12 brace and started to fracture after 615 times of open and close procedure. In terms of manufacturing time, 3D printed braces required 40 printing hours and 3 labor hours, while the traditional brace requires 9 labor hours. Regarding to the material cost and weight of the ULTEM1010, Nylon12 and polypropylene braces compared in this study, they were CAD$508, 770g; CAD$188, 649 g and CAD$100, 921g respectively. The result of brace gap distance is shown in Table 3 - 8. The largest gap difference between intended design and initial printed brace is 1.46 cm and 0.42 cm for bottom edge of Nylon12 and ULTEM1010 brace respectively. The largest

standard deviation of five repeated measures is 0.6 mm and the largest standard deviation between three brace sections is 2.4 mm. The average gap distances of Nylon12 and ULTEM1010 braces did not show increasing trends from initially printed to the end of simulation of donning and doffing.

(a)

(b)

(c)
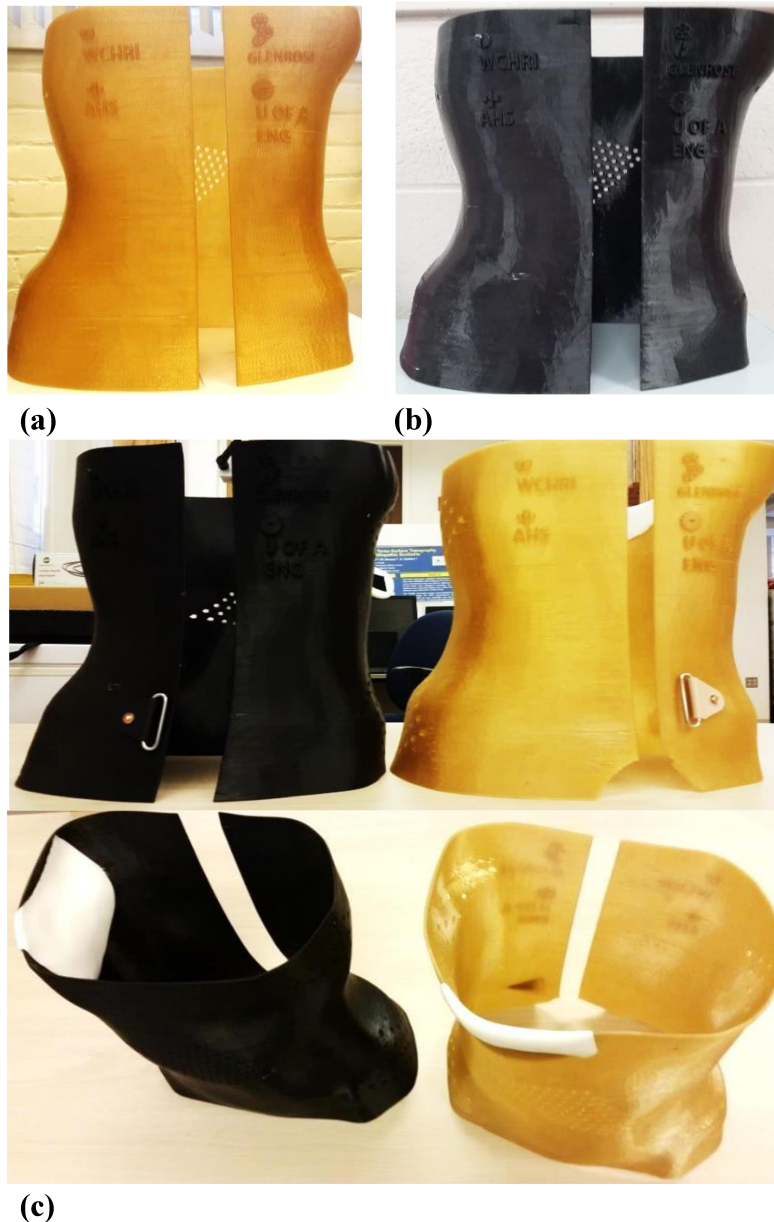
Figure 3 - 6 3D printed braces. (a) 2.54 mm thick ULTEM1010 brace. (b) 2.54 mm thick Nylon12 brace. (c) ULTEM1010 and Nylon12 braces after orthotists evaluation.

Table 3 - 8 Anterior brace gap distance after donning and doffing for Nylon12 and ULTEM1010 prototype braces

Brace Gap Distance (mm)					
Simulated time (months)	Nylon12				
	Top edges	Middle edges	Bottom edges	Average	Standard deviation
Design	25.4 ± 0.1	25.5 ± 0.1	25.9 ± 0.0	25.6	0.3
0	35.9 ± 0.3	36.9 ± 0.3	40.5 ± 0.1	37.8	2.4
3	36.6 ± 0.3	37.1 ± 0.3	40.8 ± 0.1	38.2	2.3
6	36.6 ± 0.2	36.9 ± 0.2	40.0 ± 0.2	37.8	1.9
9	36.5 ± 0.4	36.5 ± 0.3	40.2 ± 0.1	37.7	2.1
12	36.6 ± 0.2	37.2 ± 0.2	40.5 ± 0.3	38.1	2.1
15	36.9 ± 0.4	37.4 ± 0.2	40.5 ± 0.5	38.3	2.0
18	36.3 ± 0.2	37.0 ± 0.2	40.3 ± 0.3	37.9	2.1
21	36.5 ± 0.2	36.8 ± 0.2	40.1 ± 0.4	37.8	2.0
24	37.9 ± 0.5	38.3 ± 0.6	41.9 ± 0.4	39.4	2.2
Simulated time (months)	ULTEM1010				
	Top edges	Middle edges	Bottom edges	Average	Standard deviation
Design	25.4 ± 0.1	25.5 ± 0.1	25.9 ± 0.0	25.6	0.3
0	21.7 ± 0.1	21.7 ± 0.3	21.7 ± 0.4	21.7	0.0
3	21.7 ± 0.1	21.5 ± 0.2	21.7 ± 0.2	21.6	0.1
6	21.6 ± 0.1	21.7 ± 0.3	21.8 ± 0.1	21.7	0.1

3.3.3. Discussions

Evaluation of spinal braces manufactured with 3D printing had shown that Nylon12 brace was modifiable, flexible, and able to retain structural integrity with 2 year (2920 times) of donning/doffing. On the other hand, ULTEM1010 brace fractured at 5 months (615 times) of donning/doffing. The material cost for Nylon12 brace was also about 37% of ULTEM1010 brace. Nylon12 brace had about 30% weight reduction from traditional brace and required one third of the labour time. Material cost of Nylon12 was about twice of the traditional brace. However, the overall cost was still lower with reduction in labour cost. The gap difference between intended design and initial printed brace is likely due to thermal expansion in the printing and cooling process, which could possibly be accounted for in future brace manufacturing. Small standard deviation of repeated measures at each section indicates consistent measurements, and a larger standard deviation between brace

sections might indicate a variable gap distances between brace sections due to different change in length due to thermal expansion of different geometries. Importantly, ductile Nylon12 brace did not show increase in gap difference after 24 months of simulated donning and doffing which indicated no plastic deformation occurred. ULTEM1010 brace also did not show increase in gap difference before fracture as expected because ULTEM1010 is a brittle material with small tensile elongation to break according to manufacturer data [133]. Based on the findings from evaluations, 2.54 mm Nylon12 prototype brace is the optimal 3D printed spinal brace.

3.3.4. Conclusion

In conclusion, this study evaluated 2.54 mm ULTEM1010 and Nylon12 3D printed prototype braces. 2.54 mm Nylon12 prototype brace is found to be an optimal 3D printed spinal brace found so far. 2.54 mm Nylon12 brace has twice the material cost of a traditional 4 -5 mm polypropylene brace, however, the overall cost is lower. As well, it has 30% weight reduction, nearly half as thin, and requiring one third of labour time to manufacture.

Chapter 4: Design and Evaluation of Dynamic Brace Pads and Brace Casting Frame

Chapter 4 reports the design and evaluation of the dynamic inflatable brace pads and the brace casting frame which can be used for assisting brace design. Section 4.1. includes the design process of four dynamic brace pads beginning with design specifications, conceptual designs, prototypes, revision and the final product. Section 4.2. reports the evaluation of the dynamic brace pads. It includes pressure leakage experiments, evaluation of pad expansion, interpretation of results and brace pad manufacturing challenges. Lastly, section 4.3. describes the design and evaluation of the brace casting frame. Pilot evaluation of brace casting frame was performed in the laboratory with a volunteer prior to clinical study.

4.1. Design Process of Dynamic Brace Pads

4.1.1. Dynamic Brace Pad Design Motivation and Specifications

Current brace casting process with the providence system requires four different brace pads pushing laterally on the body at axilla, thoracic, lumbar and greater trochanter regions to simulate in-brace pad contact on torso for correcting scoliotic curve. Orthotists push the pads on patient's torso to hold the spinal curve while casting to capture body shape. The amount of force the orthotist applied is within patient tolerance in order to obtain in-brace correction of at least 50% based on recommended clinical practice [141], which is also the minimum initial in-brace correction needed for successful treatment outcome [142], [143]. However, quantitative measures of how hard orthotist needs to push at each region for obtaining adequate curve correction are not known. Development of the dynamic brace pads aims not only to maintain pressure level at each torso region, but also provide real-time pressure measurements. The casting pressure measurements can help orthotists adjust applied pressure at each torso region accurately and consistently based on curve correction observed.

Prior to designing the dynamic brace pad, a pump-valve pressure control monitor system was developed. The pressure control system was able to measure and control air pressure wirelessly via Bluetooth by using an iPad. The dynamic brace pads are then connected to

the pump-valve monitor. Through the iPad, the designed brace pads can be inflated and deflated to change pressure level or maintaining a certain pressure level within a range of threshold values.

The design specifications of the dynamic brace pads are:

1) airtight without leakage,

2) inflatable up to 120 mmHg (16 kPa) (based on literature [83], [138]),

3) easily adaptable to the developed pump/valve control unit,

4) comfortable to contact patient's torso,

5) thin and lightweight design to be easily added on the brace casting system,

6) designed to conform to the custom providence brace casting system,

7) durable for long term use as part of the brace casting system, and

8) easily clean and suitable for direct contact on patients' body.

4.1.2. Conceptual Designs and Testing

4.1.2.1. First Conceptual Design

The first conceptual design had L-shape geometry, with an overall dimension of 12.2 cm in length, 10.5 cm in width and 0.9 cm in thickness as shown Figure 4 - 1 (a). The L-shape geometry had a rough approximation of the shape and size of a thoracic pad in a typical daytime brace for simplifying the design. This design consisted of a sleeve and L-shape pad components as shown in Figure 4 - 1 (b). The brace pad was designed in two parts in order for removal of printing support material inside. This would allow space for air to fill when inflating. The sleeve had two thin sliding rails with a trapezoid cross section for ease of sliding into the slots of the L-shape pad and for better sealing. The L-shape part had a nozzle for connection with the pump/valve unit. The entire brace pad was 3D printed with TangoBlackPlus material with an ObJet EDEN350V Polyjet 3D printer. The TangoBlackPlus is a soft rubbery material that has high percentage of elongation to break. The sleeve was first attached using superglue compatible with Polyjet material (Sico Met). However, due to fast curing of superglue, the sleeve was unable to attach fully on the slots leading to leakage. Epoxy was then used to seal the remaining gap. After the prototype was ready, a hand pump (Figure 4 - 2) was used to inflate the pad few times with pressure up

to 30 mmHg (4 kPa). The brace pad then started leaking with a pin-hole developed at the fillet region on the inner corner of the L-shape. This was due to pad expansion creating high stress concentration at the fillet region. More leakages were observed at the sleeve area when the pad was immersed into water. Air bubbles came out from the pin-hole area with a small crack initiated. Due to the leakage problem, a new design was proposed.

(a)

ITEM NO.	DESCRIPTION	Exploded view/QTY.
1	Sleeve	1
2	L shape pad	1

(b)
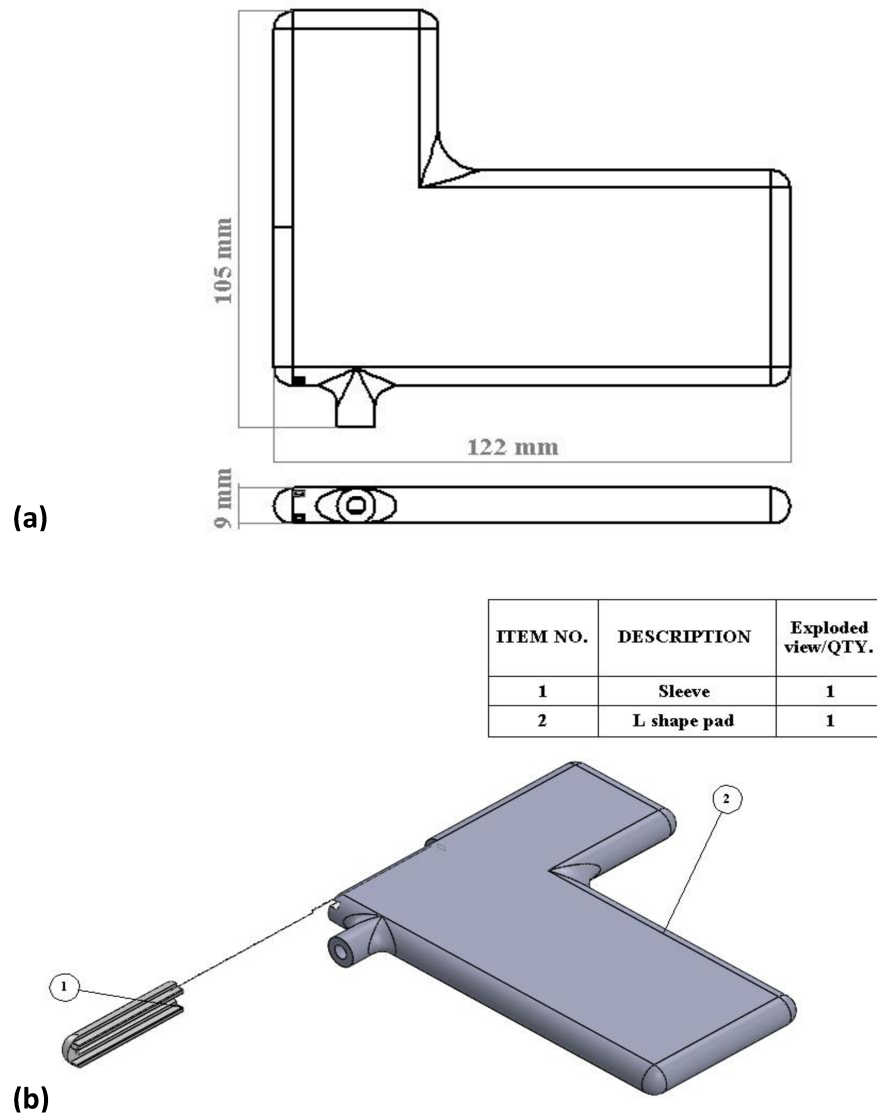
Figure 4 - 1 First dynamic brace pad conceptual design. (a) Exploded isometric view and component list. (b) Top and front views with overall dimensions.

Figure 4 - 2 Prototype and testing of the first dynamic brace pad conceptual design.

4.1.2.2. Second Conceptual Design

The overall dimensions of the second conceptual design are shown in Figure 4 - 3 (a). The design concept was a close approximation to the shape and size of the thoracic pad in a typical daytime brace with components shown in Figure 4 - 3 (b). The pad design consisted of a 3D printed rigid base using an ObJet30Pro printer with PolyJet VeroClear material. The printed base included a nozzle at the edge for connection with the pump-valve control unit. The edge around the rigid base was designed with a specific cross section as shown in Figure 4 - 4 (a), (b), (c), and (d). A 3D printed TangoBlackPlus rubbery pad cover was connected to the rigid base. The connection was similar to a car tire and rim connection, where the 3D printed rubbery material was stuffed into the rigid base edge with a special tool. Four configurations with different cross sections (Figure 4 - 4 (a), (b), (c), and (d)) were proposed to be tested for optimal airtight seal and ease of manufacturing. However, after estimation of the cost in 3D printing the rubbery material and the foreseeable difficulties in manufacturing, this design was discarded.

ITEM NO.	DESCRIPTION	QTY.
1	Rigid Base	1
2	Pad Cover	1
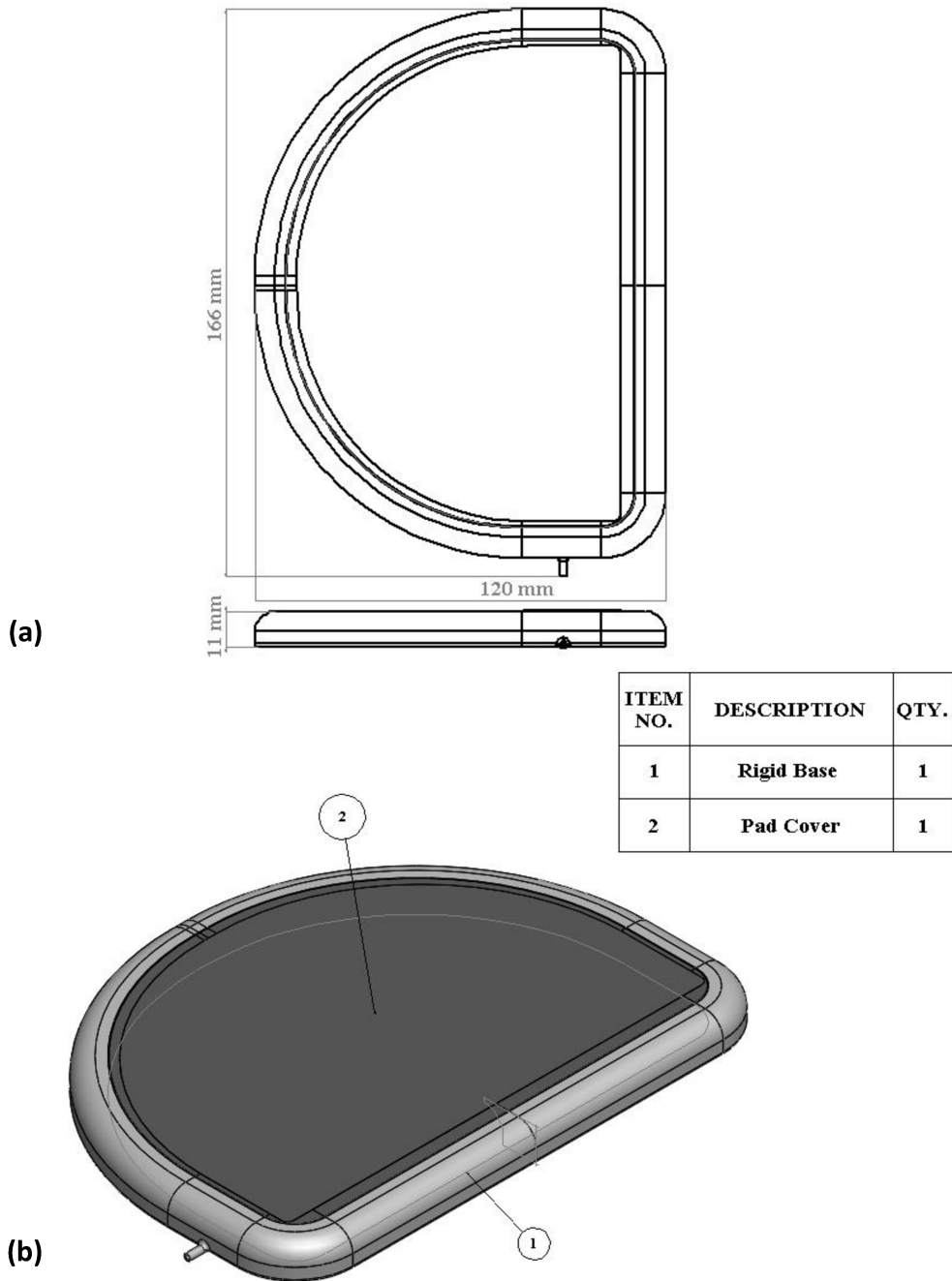
Figure 4 - 3 Solid model of second brace pad conceptual design. (a) Top and front views with overall dimensions. (b) Isometric view with component list.
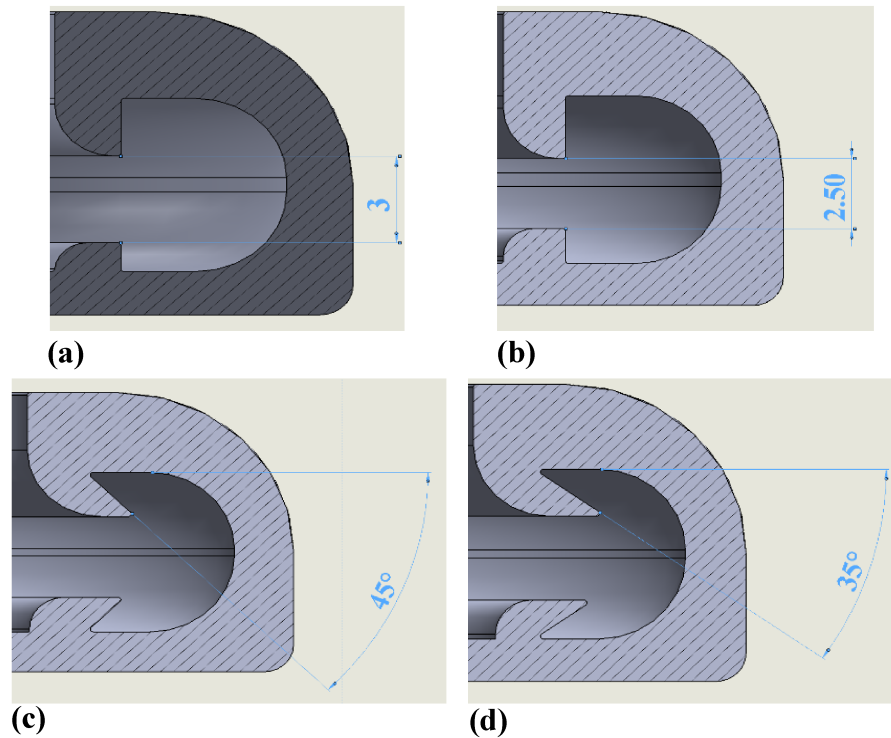
Figure 4 - 4 Brace pad rigid base cross section. (a) Flat hooks with 3 mm gap. (b) Flat hooks with 2.5 mm gap. (c) 35 degrees slanted hooks. (d) 45 degrees slanted hooks.

4.1.2.3. Third Conceptual Design

An alternative design was proposed with modifications from the second conceptual design. Modifications include using rubber type material normally used for wheelchair seat cover to replace the 3D printed rubbery material as pad cover. An additional modification includes using glues to attach the rubber cover on the base of the pad. The base pad design only included a simple ledge around the pad. A ring of silicon glue was placed between the ledge and pad cover for airtight sealing.

Prior to designing the final prototype, experiments were conducted on the third concept design. One experiment was testing whether the 3D printed base can be modified to conform to the providence casting system brace pad shapes with heating after printing. That's because modelling custom curved brace pad shapes would be more challenging, and it would require additional 3D printing support material. Another experiment was conducted to verify the airtightness for this design concept. A scale down prototype was

created and tested to be airtight up to 120 mmHg. Lastly, a full-scale prototype as shown in Figure 4 - 5 was created. The brace pad was pumped to an air pressure of 100 mmHg with two points of leakage found. The two points of leakage were found at the connecting section between the base pad and the pad cover. This was due to inconsistency in the application of silicon glue that left pockets of thinner sealed sections because of the difficulty in spreading silicon glue evenly. Another cause was the weak bond strength of silicon glue to withstand the strong pulling force of the pad cover when inflated. The leakage was from the foam layer beneath the rubber cover allowing air to pass through to the edge of the pad cover at the weakly silicon sealed region.

(a)   **(b)**
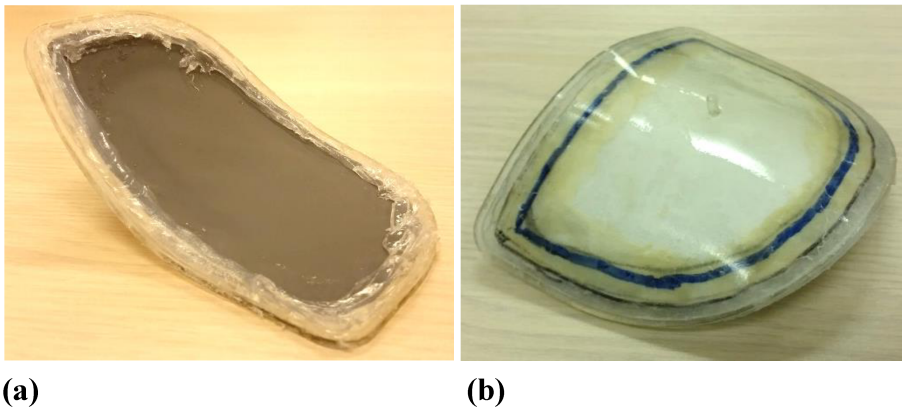
Figure 4 - 5 Third conceptual brace pad design. (a) Front view. (b) Back view.

4.1.3. Final Design

To resolve the challenge of leakage with increase pressure level from the previous design, the new final design consisted of a top ring and a pad base as shown in Figure 4 - 6. The overall dimensions of axilla, lumbar, thoracic, and trochanter pads are shown in Figure 4 - 7 and Figure 4 - 8. Both the top ring and the pad base had teeth for clamping cover sheet in place. The cross section in Figure 4 - 9 illustrates how the pad cover sheet was clamped in place as well as how the top ring and the pad base were connected. There were four teeth at the cross section with 0.6 mm height and a 0.4 mm gap between the teeth from the top ring and pad base. The teeth at the cross section increased friction to counter the pulling force of pad cover with inflation. As well, the epoxy glued at the outer edge provided much strong bonding and clamping force against pulling force of pad cover with inflation.

A nozzle adaptable to pump-valve control unit was designed at the back of the pads. Small screw holes around the rim of the pad were designed so that top ring and pad base would be connected when bending the brace pad into curve shape to create similar bending curvatures. Furthermore, the top ring and pad base were clamped in place with screws and nuts at the screw hole while silicon and epoxy glue were settling. The top ring and pad base were 3D printed with RGD450, a flexible simulated polypropylene material with lower modulus of elasticity, flexural modulus and higher elongation to break that would allow more bending without breaking than other brittle 3D printed materials. The pad cover sheet was made of food grade silicon. Both sides of the cover sheet were made of the same airtight material. Furthermore, it is biocompatible to skin and it could be cleaned with soap or alcohol.

ITEM NO.	DESCRIPTION	Exploded view/QTY.
1	Top ring	1
2	Silicon cover sheet	1
3	Pad base	1
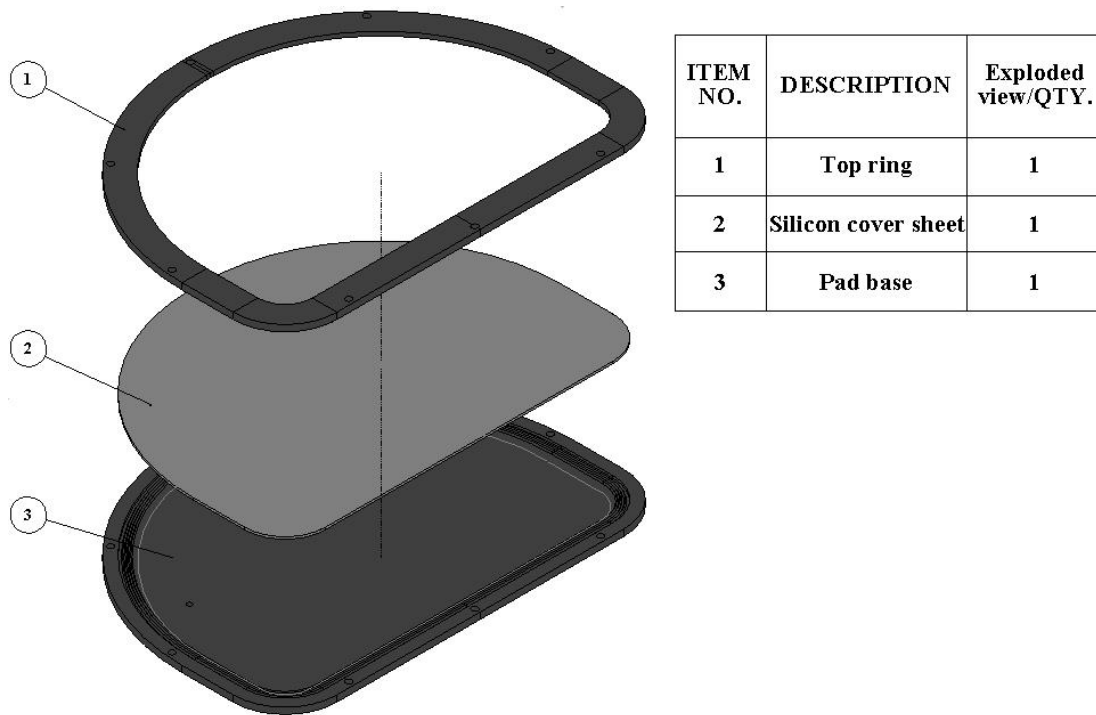
Figure 4 - 6 Exploded view and component list of final dynamic brace pad design.
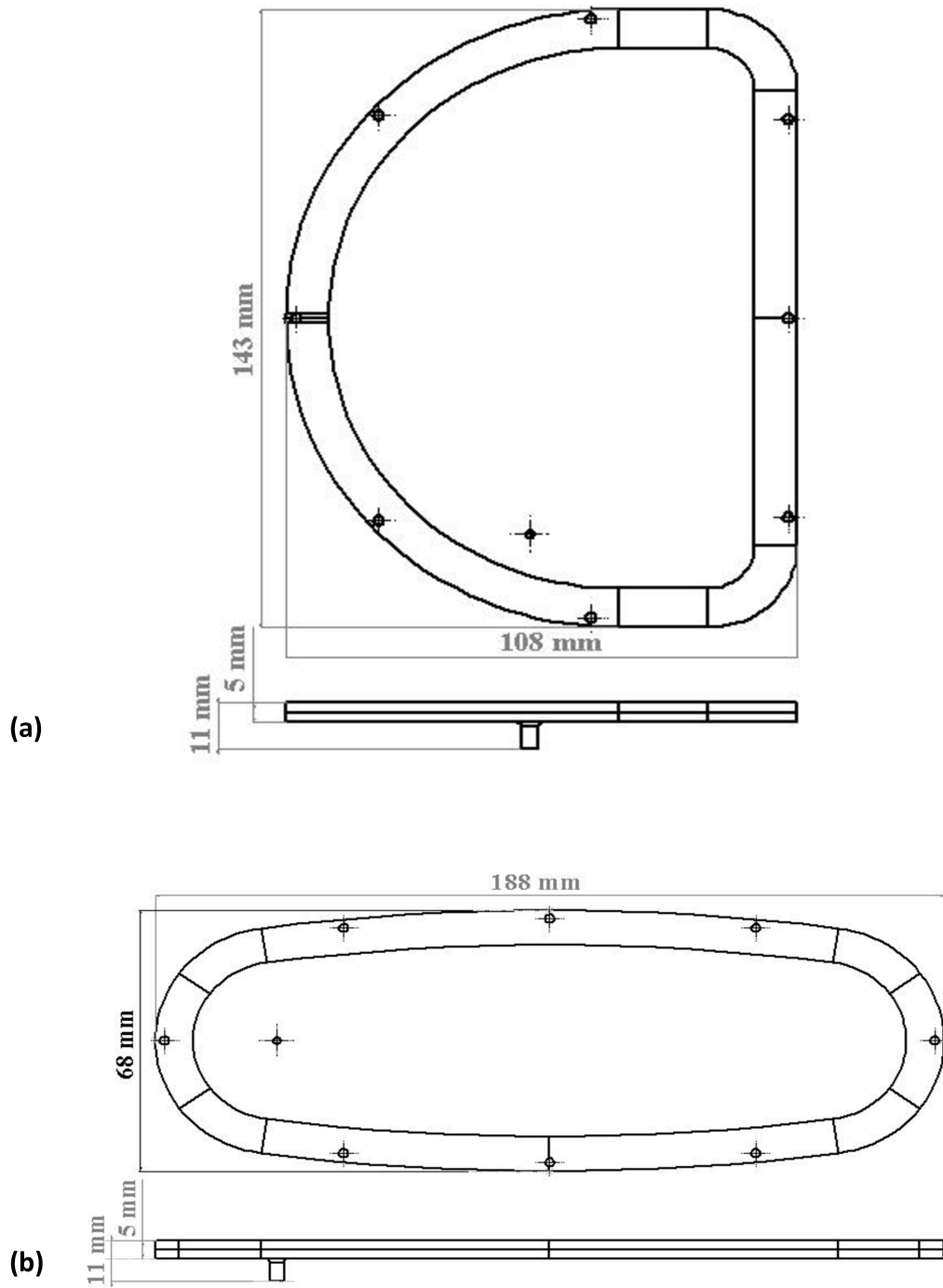
Figure 4 - 7 Top and front view of final brace pad design. (a) Axilla pad. (b) Lumbar pad.
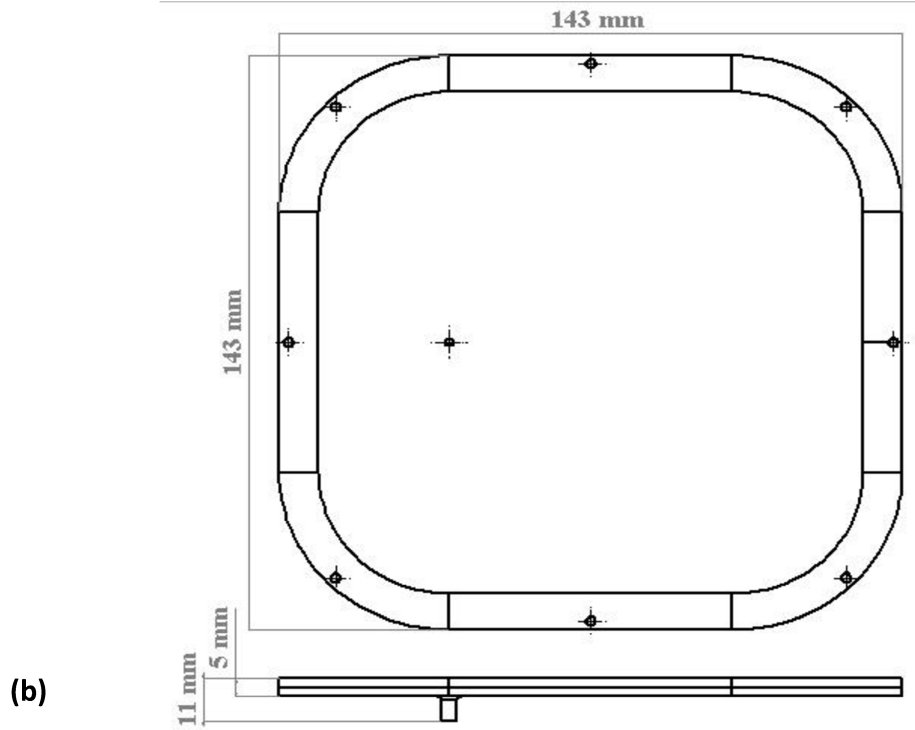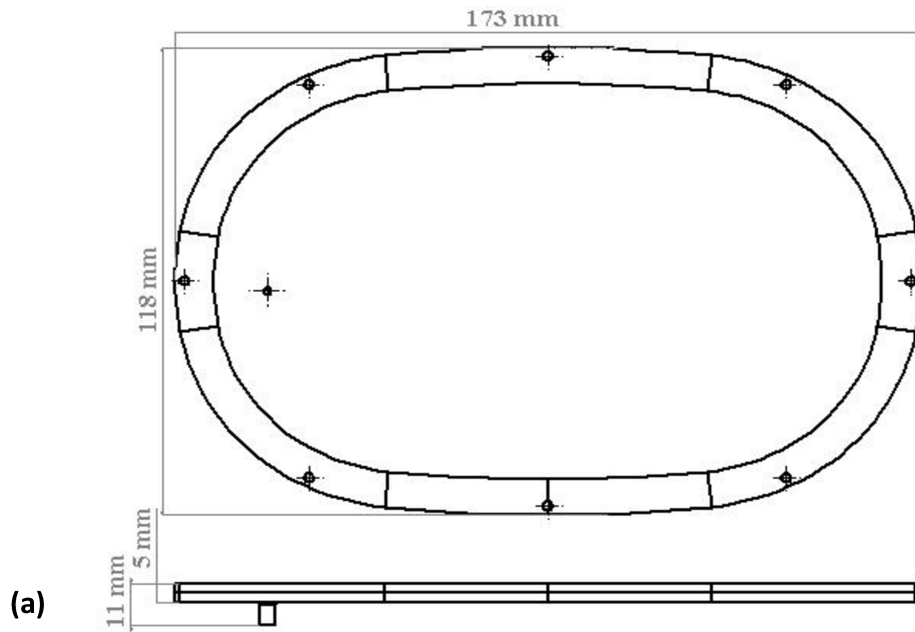
Figure 4 - 8 Top and front view of final brace pad design. (a) Thoracic pad. (b) Trochanter pad.
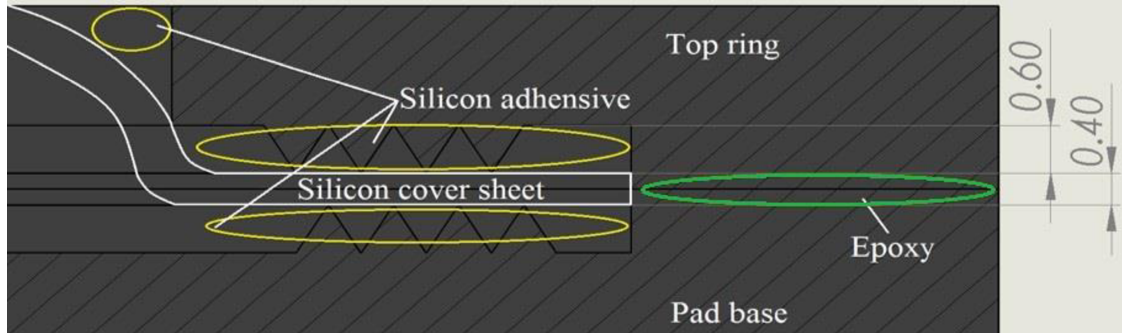
Figure 4 - 9 Cross section of the rim segment of the final dynamic brace pad design.

A set of 3D printed tools were created to apply silicon glue and epoxy evenly on the connecting surfaces of the brace pad. A glue spreading fork (Figure 4 - 10 (a)) was dipped in a pool of silicon glue or epoxy and it was applied across the edge around the brace pad. The concave hole of the spreading fork created an even bead of glue along the edge of the brace pad. After that, the glue wipe (Figure 4 - 10 (b)) was used to remove any residual glue stuck on the spreading fork or on the edge of the brace pad.

(a)   (b)
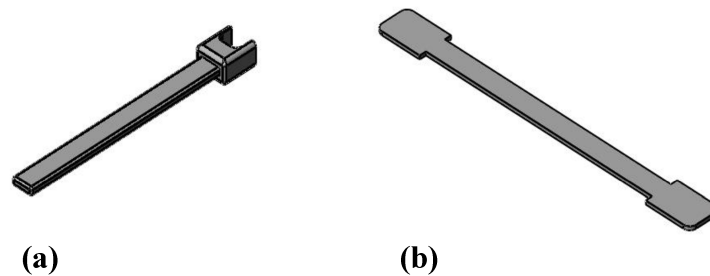
Figure 4 - 10 Custom tools for applying silicon glue and epoxy evenly on brace pad connecting surfaces. (a) 3.5 cm long spreading fork. (b) 5 cm long glue wipe.

In order to test the grip strength of the proposed design against a large pulling force, a small segment of the cross section around the pad was printed. A small piece of silicon cover sheet was clamped by the teeth cross section segment and glued as described previously. The small piece of cover sheet was pulled aiming for removal from the teeth cross section grip. As a result, the silicon sheet was torn with the teeth cross section still holding a piece of the silicon cover sheet. This demonstrated a strong grip design that would be able to withstand the pulling force of an inflated pad. Another similar experiment was conducted but with a segment of teeth cross section bended for testing the grip strength of a curved

shape pad with pulling force. The curve segment was able to retain the silicon cover sheet with pulling force, which demonstrated a strong grip strength design even with a curve brace pad. After the grip strength tests, the final brace pads were printed and assembled as shown in Figure 4 - 11. The brace pads did not show any leakage from initial inflation and deflation.

Figure 4 - 11 Manufactured dynamic brace pads. Top left: thoracic pad. Top right: trochanter pad. Bottom left: lumbar pad. Bottom right: axilla pad.

4.2. Evaluation of Dynamic Brace Pads

4.2.1. Leakage Experiments to Evaluate the Airtightness of Pressure Monitoring System for Brace Casting Process

The final dynamic brace pads were tested to evaluate if there was any leakage at maximum pressure during casting. Thoracic, lumbar, axilla, and trochanter brace pads were attached to four different pump-valve control units described in section 4.1.1.

and they were inflated to 100 mmHg without any compression on the pad cover. One initial and final pressure measurements after 20 minutes were recorded with the pressure values displayed on an iPad. Pressure level of 100 mmHg was tested instead of the maximum pressure of 120 mmHg, because there was the concern of plastic deformation of silicon cover sheet with significant volume expansion of thoracic and trochanter pads.

Final pressure was recorded after 20 minutes because the brace pads were typically applied on the patient for about 20 minutes during brace casting process.

The result of the experiment showed a significant pressure drop of 33% for lumbar pad with pressure control unit 2 within 20 minutes. After that, the lumbar pad was placed underwater, but it did not reveal any leakage with escaping air bubbles. Through this preliminary experiment, it was determined that testing of both the dynamic brace pads and the pump-valve control system were needed. That's because both components would be used for pressure measurements during casting and the pump-valve control system could be leaking.

The next experiment involved finding the leakage of each brace pad and pressure control unit with 1) hand pump (Figure 4 - 2) measurement and 2) pressure control unit measurement of each brace pad. First, the leakage caused by the hand pump needed to be found. The hand pump leakage was tested by plucking the outlet and inflating the hand pump to 120 mmHg. The hand pump pressure was recorded after 20 minutes. The hand pump leakage was tested three times, and the average leakage was 3 mmHg after 20 minutes with no deviation between measurements. Since the hand pump leakage was a systematic error, it could be subtracted from the total leakage in the experiment 1) hand pump measurement of brace pads for finding brace pad leakage. With the brace pad leakage known, the pressure control unit leakage could also be found. It was found by subtracting brace pad leakage from the total leakage found in experiment 2) pressure control unit measurement of brace pads.

The set up for experiment 1) and 2) (Figure 4 - 12) was for simulating compression of brace pads with contact on torso during the brace casting process instead of the previous experiment with no compression on the inflated pads. The setup was constructed with the Open Beam mini T-slot framing, which allowed adjustable clamping distance and height of the brace pads.

(a)　　　　　　　　　　　　(b)

(c)
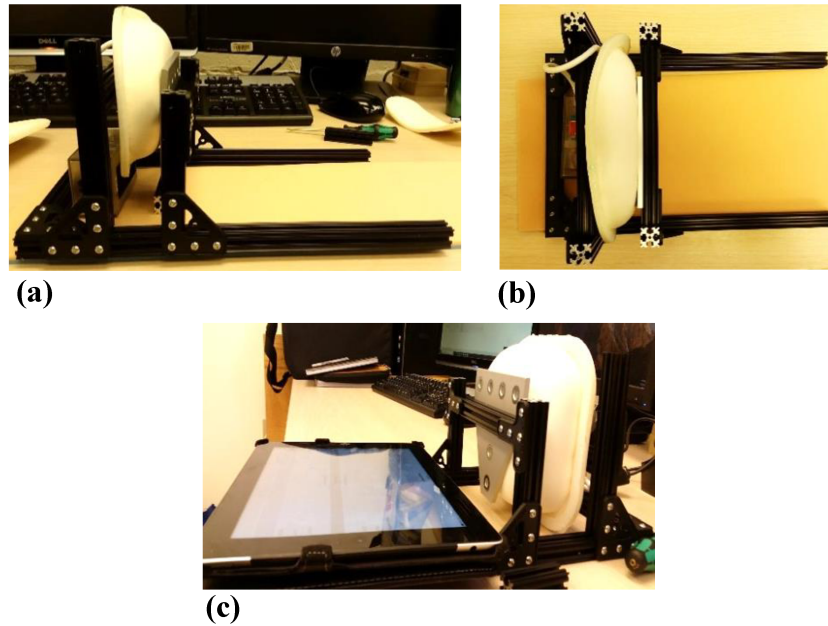
Figure 4 - 12 Dynamic leakage test setup. (a) Front view of thoracic pad testing. (b) Top view of thoracic pad testing. (c) Front view of trochanter pad testing.

The thoracic and trochanter pads were inflated to an initial pressure of 40 mmHg. Lumbar and axilla pads were inflated to an initial pressure of 60 mmHg. That's because thoracic and trochanter pads had a much larger expansion height at the same pressure level as lumbar and axilla pads due to their unique brace shapes.

Two framing columns were adjusted and locked in place in order to clamp on the brace pads and increased the brace pad pressure up to 120 mmHg. An aluminum plate was sandwiched between the horizontal framing beam and the silicon cover sheet for distributing the applied pressure similar as contacting the patient torso. Pressure measurements for the four brace pads were recorded for 20 minutes in 5 minutes intervals for monitoring any subtle changes in pressure with both hand pump and pressure control units. The brace pads and corresponding pressure measurement control unit for the leakage test is shown on Table 4 - 1. Following the test, pressure control unit 2 was resealed with silicon adhesive to prevent leakage. Another test was conducted with identical experimental set up except for using control unit 2 for lumbar pad pressure measurement. Pressure measurement with control units was conducted with initial pressure of 120 mmHg.

Only the initial pressure and final pressure after 20 minutes were recorded. However, five repeated measurements were performed for each brace pad.

Table 4 - 1 Brace pad and corresponding pressure measurement control unit for leakage test

Brace pad	Pressure control unit
Thoracic	4
Lumbar	1
Axilla	3
Trochanter	1

4.2.2. Airtightness of Dynamic Brace Pads and Pressure Control Units

Brace pad and pressure control unit leakages were found with experiment 1) hand pump measurement and experiment 2) pressure control unit measurement of brace pads as shown in Table 4 - 2. Pad leakage was calculated by subtracting the hand pump systematic error $(3 \pm 0 \text{ mmHg})$ from the total leakage from hand pump measurement of brace pad. Pressure control unit leakage was calculated by subtracting the pad leakage from the total leakage from control unit measurement of brace pad. Maximum pad leakage was 3 mmHg, maximum pressure control unit leakage was 5 mmHg, and the maximum combined leakage was 7mmHg. No drastic pressure drop was observed in Figure 4 - 13 for the pressure measurements of the brace pads with control units at 5 minutes intervals for 20 minutes. The largest pressure drop from Figure 4 - 13 was about 4 mmHg for lumbar pad from 15 to 20 minutes. From section 4.2.1., the lumbar pad with measurement from pressure control unit 2 had significant pressure drop. However, hand pump and pressure control unit 1 measurements of lumbar pad did not show significant pressure drop. This demonstrated leakage was due to pressure control unit 2 and the control unit was resealed. The resealed pressure control unit 2 was used to measure lumbar pad pressure. Repeated measurement was conducted for testing brace pads with their corresponding pressure control units that would be used for the brace casting process. Results were shown in Table 4 - 3. Lumbar and axilla pads had the highest average pressure drops of 5 mmHg (5 %) and 7 mmHg (6%) respectively.

Table 4 - 2 Brace pad pressure measurements after 20 minutes with 120 mmHg initial pressure

Brace pad	Total leakage from hand pump measurement (mmHg)	Pad leakage (mmHg)	Pressure control unit	Total leakage from control unit measurement (mmHg)	Pressure control unit leakage (mmHg)
Thoracic	6	3	4	4	1
Lumbar	5	2	1	7	5
Axilla	4	1	3	6	5
Trochanter	4	1	1	6	5
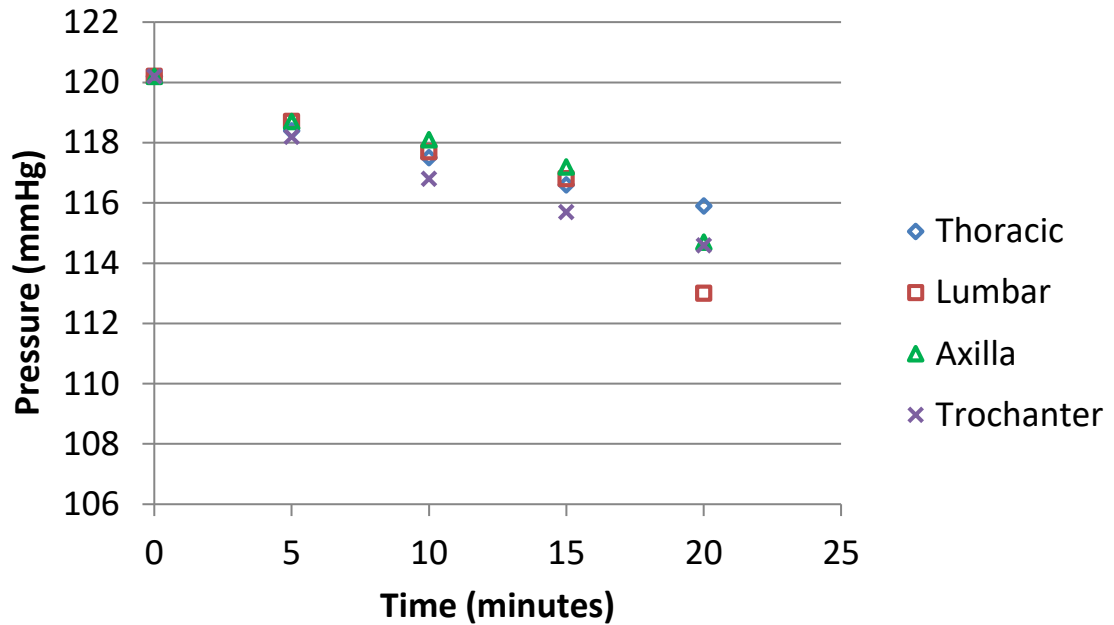
Figure 4 - 13 Pressure measurements of brace pads with control units at 5 minutes intervals for 20 minutes duration from initial pressure of 120 mmHg.

Table 4 - 3 Average pressure measurements of brace pad with pressure control units after 20 minutes with 120 mmHg initial pressure

Brace pad	Pressure control unit	Average pressure (mmHg)	Average pressure drop (%)
Thoracic	4	117 ± 1	3
Lumbar	2	115 ± 1	5
Axilla	3	113 ± 3	6
Trochanter	1	116 ± 1	3

4.2.3. A Study to Evaluate the Expansion of Dynamic Brace Pads

The four brace pads had different expansion heights at the same pressure level due to different geometries. A minimal expansion height is optimal for decreasing instability during brace casting. That's because a more convex brace pad surface with larger expansion height is more prone to shifting of body position during brace casting. The objective of this study was to evaluate the expansion height of brace pads with different inflation pressures for determining the adequate initial inflation pressure for brace casting. The brace pads were inflated up to 100 mmHg in 20 mmHg increments with pressure control units with no compression on pad cover. The brace pads were inflated up to only 100 mmHg because of the exceedingly large expansion heights of trochanter, axilla and thoracic pads with higher pressure that would likely cause permanent plastic deformation of silicon cover sheet. The brace pads were measured with a Vernier caliper (Mitutoyo, Japan) with accuracy of ±0.02mm from the lowest point of the pad base to the highest point of silicon cover sheet. The measurements were repeated five times consecutively at different positions around the brace pads. Figure 4 - 14 showed that both thoracic and trochanter pads had greater maximum pad height than axilla and lumbar pads at different pressure levels. Lumbar pad had the lowest maximum pad height even at the highest inflation pressure. Maximum inflation height is ≥ 15 mm and ≤ 30 mm for thoracic, axilla, trochanter pads at 20 mmHg, and lumbar pad at 60 mmHg.
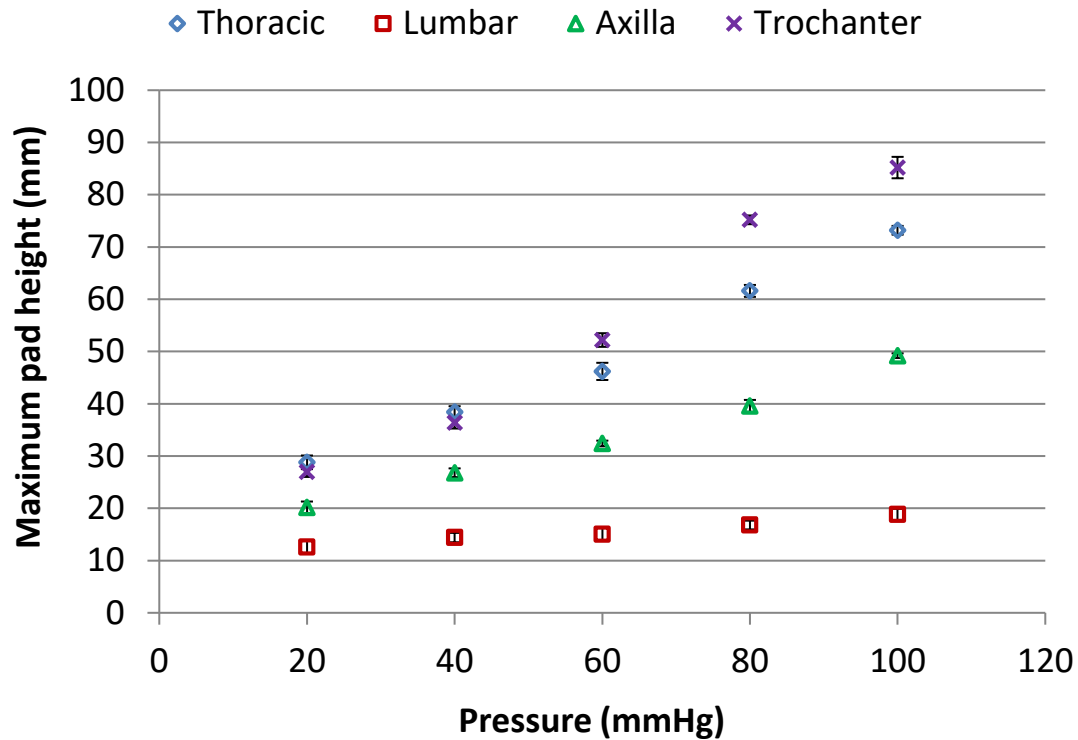
Figure 4 - 14 Maximum expansion height of the brace pads at different pressure levels.

4.2.4. Interpretation of Evaluation Results and Manufacturing Challenges

The maximum average pressure drop for different brace pads was 7 mmHg (6%) after 20 minutes with initial pressure of 120 mmHg for the axilla pad. This level of pressure drop is acceptable since the applied pressure on patient torso in clinic is typically about 40-60 mmHg. A lower initial pressure results in a lower magnitude pressure drop.

Furthermore, automatic pressure adjustment could be applied to maintain closer pressure level. A limitation for the brace pad expansion height evaluation was the measurement of a deformable pad cover. Since the pad cover was deformable, caliper measurement of maximum height could only provide a rough estimate of expansion height with some error caused by caliper clamping on a deformable surface. It was found that 20 mmHg for thoracic, axilla and trochanter pads and 60 mmHg for lumbar pad were adequate initial inflation pressures for brace casting. This would provide a maximum expansion height of at least 1.5 cm but not more than 3 cm. These initial pressure levels for the pads would have minimal expansion heights while maintaining torso contact on air cushion rather than

contacting the pad base. That's because the contact of pad base would affect the accuracy of pressure measurements during brace casting process.

There were two main manufacturing challenges for the dynamic brace pads. Manufacturing a dynamic brace pad could be a cumbersome process requiring careful distribution of two types of adhesive. Another challenge would be the consistency of manufacturing quality dependent on the creator's manufacturing skill. That means manufacturing the brace pads would require additional training and practice to achieve adequate quality.

4.3. Design and Evaluation of Brace Casting Frame

4.3.1. Design of Brace Casting Frame

A brace casting frame was used to apply brace pads on patient torso, which would simulate a patient wearing a brace in order to obtain the body shape while spinal curves were corrected. The body shape obtained was then used for creating a customized brace for the patient. However, it was often difficult to apply brace pads at the optimal location and pressure level for obtaining adequate in-brace curve correction during casting.

The new brace casting frame design aimed to be compatible with an ultrasound machine and the pressure measurement system mentioned in section 4.1.1. During casting, the real time measurements of the magnitude of spinal curve from ultrasound scans and casting pressures would be used to guide the orthotist in optimal placement and applied pressure of brace pads to obtain better in-brace corrections. The new brace design frame was also compatible with a 3D scanner for capturing the patient body shape in frame with pads applied. On another note, the traditional providence brace casting system required patient laying supine during casting, which reduced the magnitude of curvature due to gravitational effect. The providence casting system mainly allowed 2D correction of spinal curve with medial-lateral applied brace pads. On the other hand, the new brace casting frame design required patient standing during casting, which eliminated underestimation of curve severity. Also, the new casting frame allowed 3D correction of spinal curves with multi-degree of freedom brace pads, which allowed medial-lateral as well as posterior-anterior application of brace pads.

The design specifications of the new brace casting frame included:

1) Dimensions: adequate dimensions for fitting variety of patients between 10-18 years old. The height range according to CDC height chart is 122 cm to 190 cm for boys and 127 cm to 175 cm for girls [144]

2) Mounting of brace pads: able to mount four different brace pad geometries. Axilla and trochanter pads with four degrees of freedom of adjustment and thoracic and lumbar pads with six degrees of freedom of adjustment

3) Compatibility: allow the ultrasound GPS system in close proximity of ultrasound transducer which contacts the patient's spine, as well as minimal obstacles blocking a 360 degrees 3D scan around patient torso

4) Stability: adequate rigidity to maintain corrective force applied through brace pads rods during ultrasound and 3D scanning

5) Adjustment: brace pad location and applied pressure can be easily adjusted

6) Comfort: comfortable for patient with armrest during casting process

7) Portability: can be easily moved to a different location after brace casting clinic

The brace casting frame consisted of three major components including the basic frame (Figure 4 - 15 (a)), the brace pad rod mount (Figure 4 - 15 (b)) and the brace pad mount (Figure 4 - 15 (c)). The overall dimensions of the basic frame and brace pad mount system are shown in Figure 4 - 16. The basic frame was made up of T-slot aluminum framing including vertical, cross and floor bars, as well as sliders, railings, L brackets, and supporting plates as shown in Figure 4 - 15 (a). The brace pad rod mount included a screw adaptor pin, 3D printed half-screw adapter, a nylon 1'' threaded rod, aluminum bearing block as tube holder, aluminum handles, tripod head, and a 3D printed tripod to T-slot adapter as shown in Figure 4 - 15 (b). The pressure control units were attached on top of the half screw adaptor with Velcro. The brace pad mounting system included a 3D printed cup, threaded handle, adjustment screw, brace pad arm mount as well as Velcro-loop attaching the brace pads as shown in Figure 4 - 15 (c).
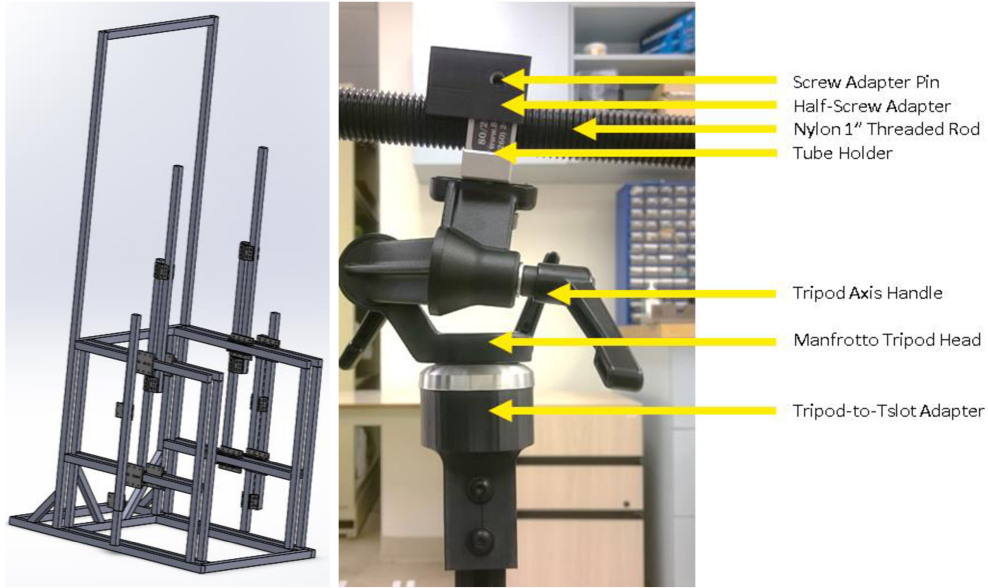
ITEM NO.	PART NUMBER	QTY.
1	Cup	1
2	Threaded Rod	1
3	Rod Handle	1
4	Adjustment Screw	2
5	Brace Pad Arm Mount	1
6	Velcro-Loop	1
7	M3 x 12mm Screw	3
8	M3 Nut	3
9	6-40 x 0.375in. Screw	2
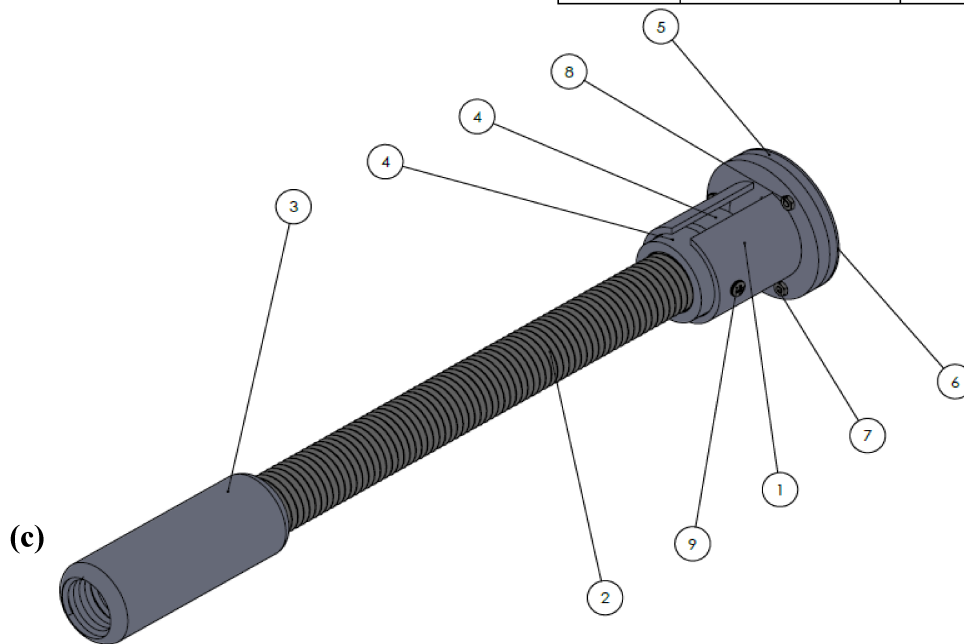
Figure 4 - 15 Brace casting frame major components. (a) Basic frame. (b) Brace pad rod mount. (c) Brace pad mount system (exploded isometric view and component list).
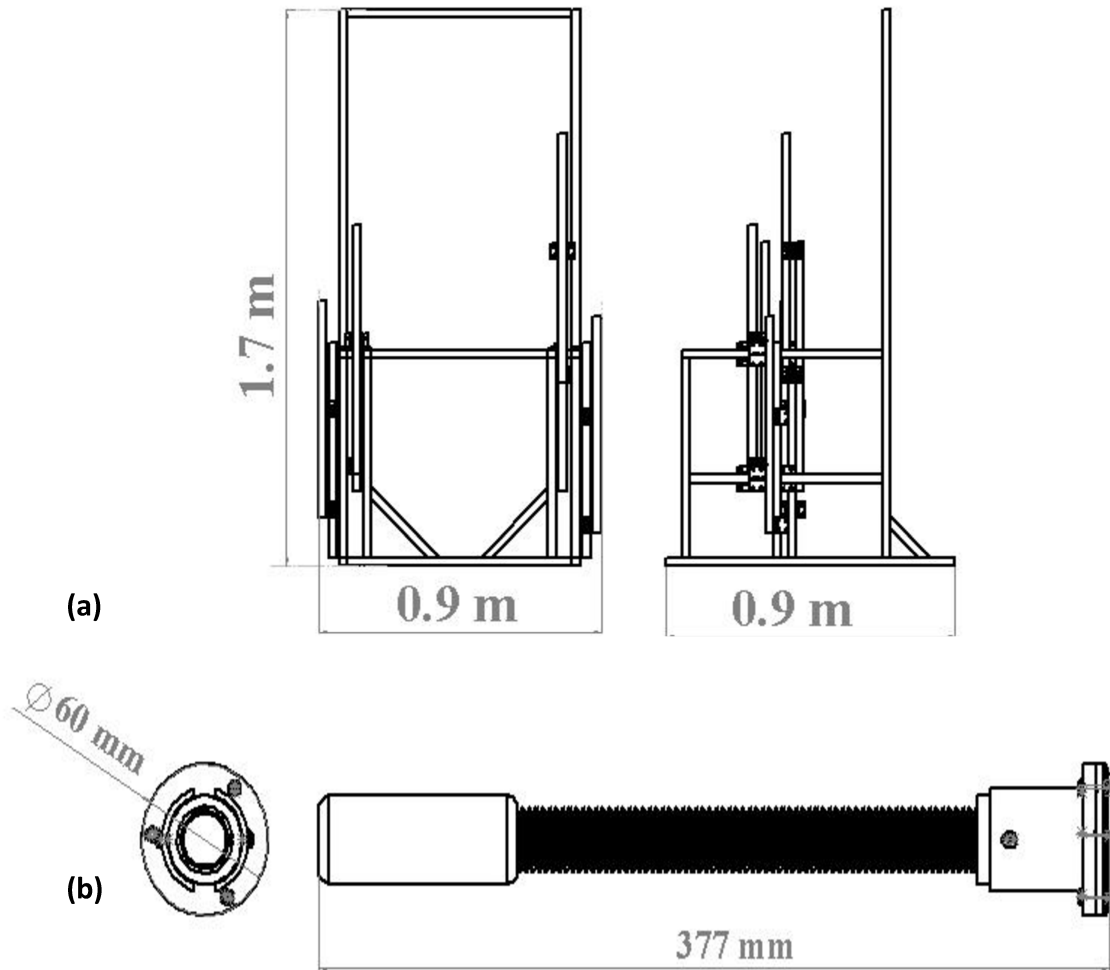
Figure 4 - 16 Front and side view with overall dimensions. (a) Basic frame. (b) Brace pad mounting system.

4.3.2. Brace Frame Mechanism and Casting Process

The constructed brace casting frame is shown in Figure 4 - 17 with patient facing the arm rest side while standing. The brace casting frame had six degrees of freedom for each brace pads. The translation of vertical height in superior-inferior direction and depth in anterior-posterior direction used the slider mechanism. Each adjustment was made by loosening and tightening the two handles clamping on the two sliders and bars. The pitch, row and yaw rotations of the brace pads were achieved by loosening and tightening each of the three handles on the tripod head of the brace pad rod mount. The last degree of freedom was the adjustment of the brace pad rods in medial-lateral direction. Global adjustment was done

by removing the screw adapter pin and half screw adapter to push or pull the rod. Fine adjustment was done by leaving the screw adapter pin and half screw adapter in place while screwing or unscrewing the rod. The brace pad mounting system shown in Figure 4 - 15 (c) allowed continue fine adjustment to increase contact pressure after the brace pad contacts patient torso. That's because the rod could rotate independently from the brace pad. The vertical range of motion magnitude of the brace pads (superior-inferior) was 30.5 cm with the slider. The vertical range of motion for axilla and thoracic pads was 31 cm to 61 cm relative to the bottom of the basic frame. The vertical range of motion for lumbar and trochanter pads was 3 cm to 33 cm relative to the bottom of the basic frame. The depth range of motion magnitude for all the pads (anterior-posterior) was 51 cm with the slider. The width range of motion (medial-lateral) was 23 cm for axilla and thoracic pads and 53 cm for lumbar and trochanter pads with the screwing motion of the brace pad rod. All the approximate range of motion had excluded the additional range with the tripod head.
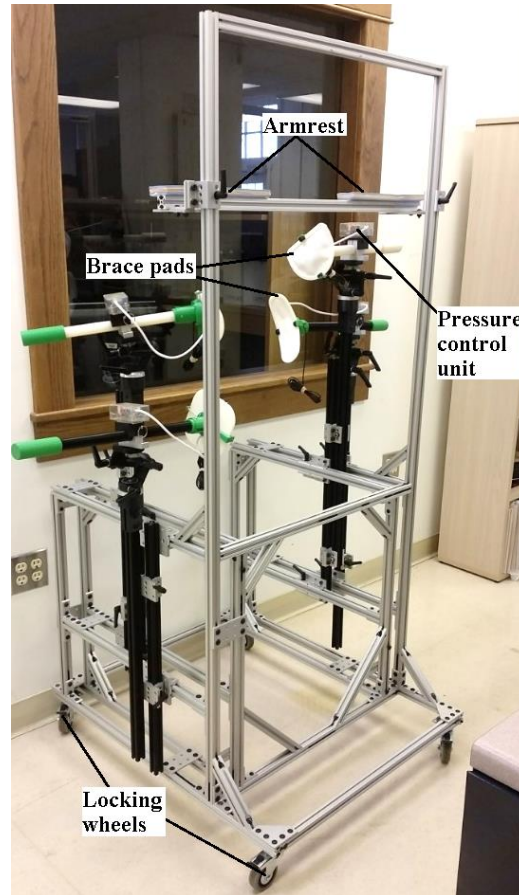
Figure 4 - 17 Constructed brace casting frame with foam arm rest, locking wheels, brace pads, and pressure control units attached.

During the brace casting process, the patient stepped into the frame facing the vertical bars with armrests. The horizontal armrest was adjusted to the neck level of a patient with the two sliders clamped in place with two handles at the adjusted level. The patient stood with forearm resting on the armrest while the clinician adjusted the vertical and depth positions of each pad to match the anatomic positions of the patient. The pitch, row and yaw orientations of the brace pads were then adjusted. The brace pad rods were pushed to contact patient torso, followed by the fine adjustment to increase pressure level at each pad by screwing the brace pad rods. Ultrasound scans and pressure measurements were conducted in between brace pad location and pressure adjustments. After optimal pad configuration was obtained, 3D scanning was conducted around patient torso in the optimal brace pad configuration. Lastly, the wheels were unlocked, and the brace casting frame was rolled out of the clinic area for storage after the casting process.

4.3.3. Evaluation of Brace Casting Frame

A healthy adult male subject with 168 cm height was recruited for the pilot evaluation of brace casting frame in the laboratory before implementation in the brace casting clinic. The brace casting frame was evaluated from an experience orthotist based on whether the seven design specifications were met. For 1) the dimension specification, the height of test subject was within design requirement of 122 cm to 190 cm for boys and 127 cm to 175 cm for girls. All brace pads were able to be adjusted by the orthotist to the necessary height corresponding to the anatomical locations (thoracic, lumbar, axilla, trochanter) of the test subject. For 2) mounting of brace pads, all brace pads with different geometries were mounted on the brace pad mount system. The brace pads were adjusted to the necessary positions by the orthotist. However, slight interference was observed between the lumbar pad rod and the vertical T-slot for mounting the axilla pad. This challenge was resolved by angling the lumbar pad slightly posterior of the torso. This lumbar pad placement was acceptable to the orthotist. For 3) compatibility, the ultrasound GPS system was able to fit near the posterior space of the patient for ultrasound scanning of the spine. Nevertheless, 3D scanning around the test subject took about 30 minutes to generate a good quality 3D scanned torso. The challenge of generating a good quality 3D scan in a short amount time was due to avoiding obstacles such as T-slot supporting beams as well as additional practice and training required for scanning pad covered regions. For 4) stability and 5) adjustment, the rigidity of the brace casting frame was adequate to maintain corrective forces with both global and fine adjustment of the brace pad rod based on orthotist evaluation. The orthotist was able to easily adjust brace pad location and pressure after practice. For 6) comfort, the test subject reported arm rest provided adequate comfort during casting. However, the prolong standing with long scan time caused slight weariness. Lastly, for 7) the portability specification, the brace casting frame was portable with the mounted wheels. In conclusion, the dynamic brace pads and brace casting frame met all the design specifications and requirements for the casting process based on evaluations in this chapter.

Chapter 5: Evaluation of 3D Scanned Torso Accuracy and the Design of a New 3D Printed Brace Manufacturing Process

This chapter describes experiments to evaluate the accuracy and precision of 3D scanned torso contour and the development of a new 3D printed brace manufacturing process. Section 5.1. describes Vorum's 3D Spectra scanner that was selected for torso scanning. Also, the rationale and objectives to evaluate the accuracy and precision of the 3D scanner are described. Section 5.2. describes the experiments and reports the results of investigating the accuracy and precision of the 3D scanner versus a motion camera system. Section 5.3. describes the experiments and reports the results of exploring torso cross section accuracy and reconstruction accuracy at pad covered regions. Section 5.4. discusses the interpretation of the results from the accuracy and precision studies. Section 5.5. describes the limitation of the studies. The findings of appropriate 3D printing parameters from chapter 3, the design and evaluation of brace casting frame and dynamic brace pads from chapter 4 as well as the accuracy and precision evaluations of the 3D scanner from this chapter were combined for developing a new brace manufacturing process. Section 5.6. reports the design of the proposed new 3D printed brace manufacturing process.

5.1. Vorum 3D Spectra Scanner

The Vorum 3D Spectra scanner is a handheld structure light scanner designed specifically for prosthetics and orthotics applications. A build in light source projects a rectangular blue light pattern on the scanned torso and a camera captures the reflected light pattern as shown in Figure 5 - 1.

Figure 5 - 1 Vorum Spectra scanner acquiring patient body contour [126].

The detected light pattern is analyzed for determining the distances from the scanned surface points to the scanner detector. The surface points are stitched together with build-in algorithms to generate the body contour. The scanner is connected to a laptop and the Spectra^{TM} software processes the data to display real time scanning surfaces. A scan range light indicator (three distance ranges) provides feedback signal for user to adjust to recommended scanning distance range with best surface detection as shown in Figure 5 - 2. The top red and orange color lights (Figure 5 - 2 (a) and (b)) indicated too close scan range (26 -38 cm), the middle green color light (Figure 5 - 2 (c)) indicated recommended scan range (38-48 cm) and the bottom red and orange color lights (Figure 5 - 2 (d) and (e)) indicated too far scan range (48-58 cm). The Spectra^{TM} software also included an algorithm to calibrate scanner setting before each scan to adjust the scanned torso body tone and surface reflectiveness, as well as the ambient light intensity. Also, the 3D scanner is sensitive to sunlight and blue light spectrum. The scanner should be used in indoor environment only. The scanned body contour can be exported to the manufacturer software, CanFit^{TM}, for modification to brace shape. The manufacturer has reported that the resolution of the output file is 0.1 mm in general.
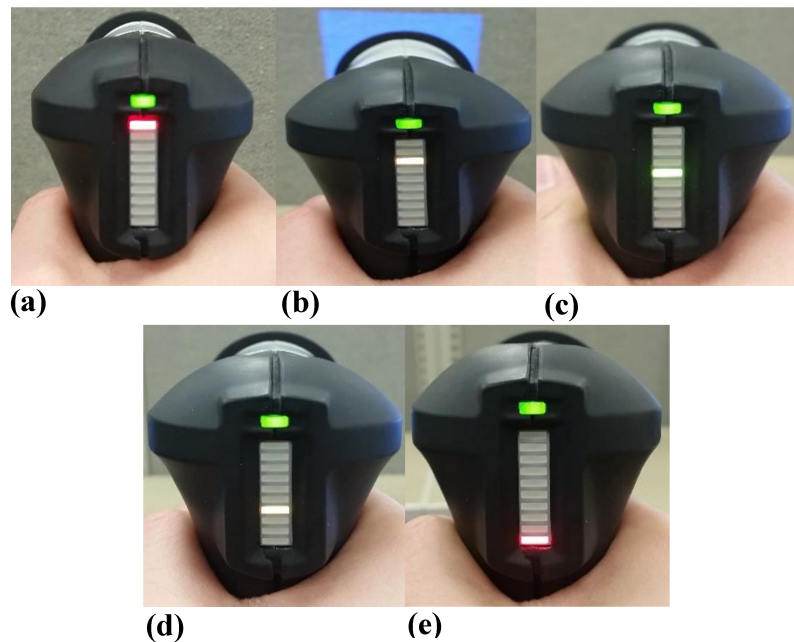
Figure 5 - 2 Scan range light indicator on Vorum 3D Spectra scanner. (a) Top red light, close scan range. (b) Top orange light, close scan range. (c) Middle green light, recommended scan range. (d) Bottom orange light, far scan range. (e) Bottom red light, far scan range.

Although the resolution of the scanner is reported, there is no study to truly validate the accuracy and precision of a scanned torso image. Furthermore, since the dynamic brace pads are to be applied onto patient torso during scanning, the accuracy of the pad covered areas after reconstruction is not known. Therefore, studies described in this chapter were aimed to evaluate the accuracy and precision at different dimensions of the 3D scanned torso and scanning the torso at different scan distance ranges as well as to investigate the scanned torso accuracy at pad covered regions after reconstruction.

5.2. Investigation of 3D Scanned Torso Accuracy and Precision Along Different Dimensions and Scan Distances[*]

A set of 3 Optitrack Prime 13W motion capture cameras (NaturalPoint Inc., Oregon, USA) (Figure 5 - 3 (a)) with a calibrated accuracy of 0.10 mm were used as the benchmark

---

[*]Materials in this section have been published in the following paper: K. Ng, E. Lou, and K. Duke, "Evaluation of accuracy, precision and optimal parameters of a 3D scanner in acquiring body contour of patients with adolescent idiopathic scoliosis," in Scoliosis and Spinal Disorders, 2018, vol. 13, p. 8.

measurement tool to capture specific dimensions on the torso (Figure 5 - 3 (b)) to compare with measurements from the Spectra Scanner (Figure 5 - 3 (d)). Each motion capture camera has ten high power LED lights filtered to infrared wavelength. The emitted light is reflected off a reflective marker placed on an object. The reflected light is used to find the 3D position of the marker when the marker is in the field of view of at least two cameras. Furthermore, sunlight, extraneous illumination or reflective surfaces should be avoided when using motion capture cameras to minimize error. Prior to using the motion cameras, they were calibrated to produce average position accuracy of 0.1 mm.
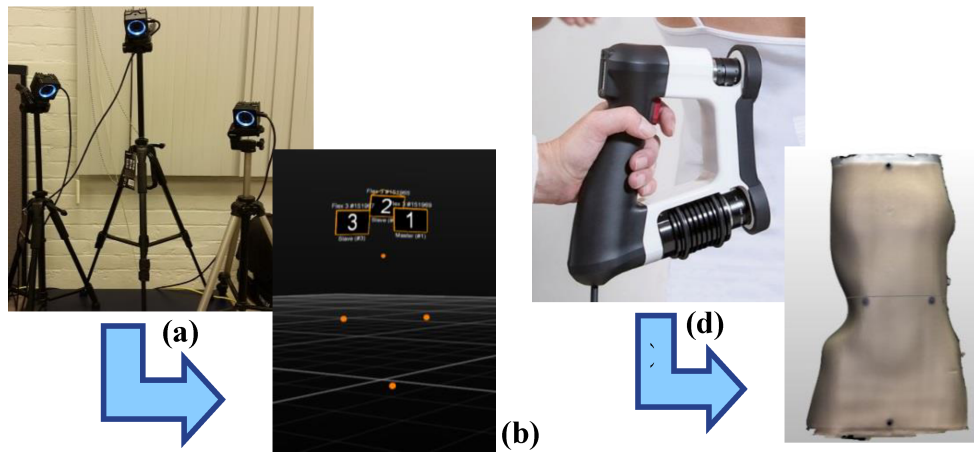
Figure 5 - 3 (a) Three Optitrack motion capture cameras mounted on tripods, (b) an image indicates the three Optitrack motion capture cameras noted by 1, 2, 3 and four reflective markers attached to a torso mold, (c) a Vorum Spectra 3D scanner, and d) an image on CanFit^{TM} software of a 3D scanned torso mold with four reflective markers attached.

A torso foam mold with ten (6.8 mm diameter sphere) reflective markers were placed in pairs to provide five linear distance measurements as shown in Figure 5 - 4. The five linear dimensions includes distance A- superior-inferior length from rib-to-waist (103mm), distance B - anteroposterior length along waist level (105mm), distance C - Lateral length along waist level (132mm), distance D - Length between axilla and iliac crest (240mm) and distance E - a torso length (495mm).
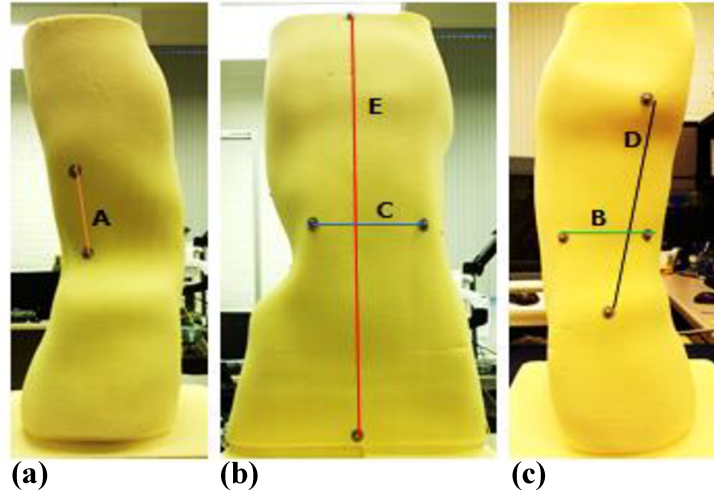
Figure 5 - 4 Three different views of the body foam mold with 10 reflective markers attached in pairs to show the five linear torso measurements. (a) Right view with measurement A, (b) Front view with measurement C and E, and (c) Left view with measurement B and D.

The torso foam mold was first placed at 1 m away from the 3 Optitrack cameras. The foam mold was put in a slanted view between Figure 5 - 4 (a) and Figure 5 - 4 (b) facing the cameras. In this way, all reflective markers would be captured by at least by 2 cameras for measurements A, C and E. The motion cameras were capturing at 240 Hz for 0.55 seconds. 132 samples were collected and the average (x, y, z) positions of each marker were calculated. After this, the foam mold was rotated at the same position until the makers for measurements B and D (shown in Figure 5 - 4 (c)) were captured by at least two cameras. Another 0.75 seconds motion capture recording with 179 frames was taken. The average x, y, z positions of the remaining markers were calculated. The linear distances (A-E) from the motion capture measurements were calculated as

$$d = \sqrt{(x_2 - x_1)^2 + (y_2 - y_1)^2 + (z_2 - z_1)^2} \qquad [5 - 1]$$

where d is the linear distance between the two centers of reflective markers (mm), and x_1, x_2, y_1, y_2, z_1, z_2 are the 3D positions of each reflective marker relative to the reference zero of the camera system.

After finding the linear distances with motion capture recordings, five 3D scans using the Spectra scanner were taken continuously at each distance. The operator walked around the torso mold at three different scan ranges 1) 26-38 cm (close configuration), 2) 38-48 cm (recommended configuration) and 3) 48-58 cm (far configuration) based on the manufacturer specification. Five measurements were performed on each image file per distance measurement. A total of 375 measurements (5 scans x 3 distance configurations x 5 linear distances (A – E) x 5 repeat measurements) were measured by one rater continuously. For the 3D scanner, linear distance between two reflective markers was measured with CanFit^{TM} software measurement tool based on the same formula [5 - 1] mentioned above. Accuracy was calculated by finding the average of the deviations between the motion capture camera and the 3D scanner measurements. Precision was calculated with the 95% confidence interval standard error from the repeated 3D scanner measurements.

5.2.1. 3D Scanned Torso Accuracy and Precision Along Different Dimensions at Different Scan Distances

The ranges for 3D scanned torso accuracy and precision along different dimensions and scan distances were 0.0-6.3 mm and 0.5-4.2 mm, respectively. The total combine error range was 0.15-8.49 mm. Figure 5 - 5 summarizes the accuracy and precision results for different scan dimensions and distances. On the vertical axis, average accuracy is represented as columns and precision represented by error bars. Each column on the graph represents the result of 25 measurements from 5 scans. On the horizontal axis, the label A-E are average values of linear distance measurements with motion camera images. They were 103, 105, 132, 240 and 495mm, respectively. The largest dimension (E) had the poorest accuracy between -2.4 to -6.3 mm while the smallest dimension (A) had the best accuracy between 0.0 to -0.9 mm. Precision was within 2 mm for measurements less than 240 mm and within 4.5 mm for larger measurements results.
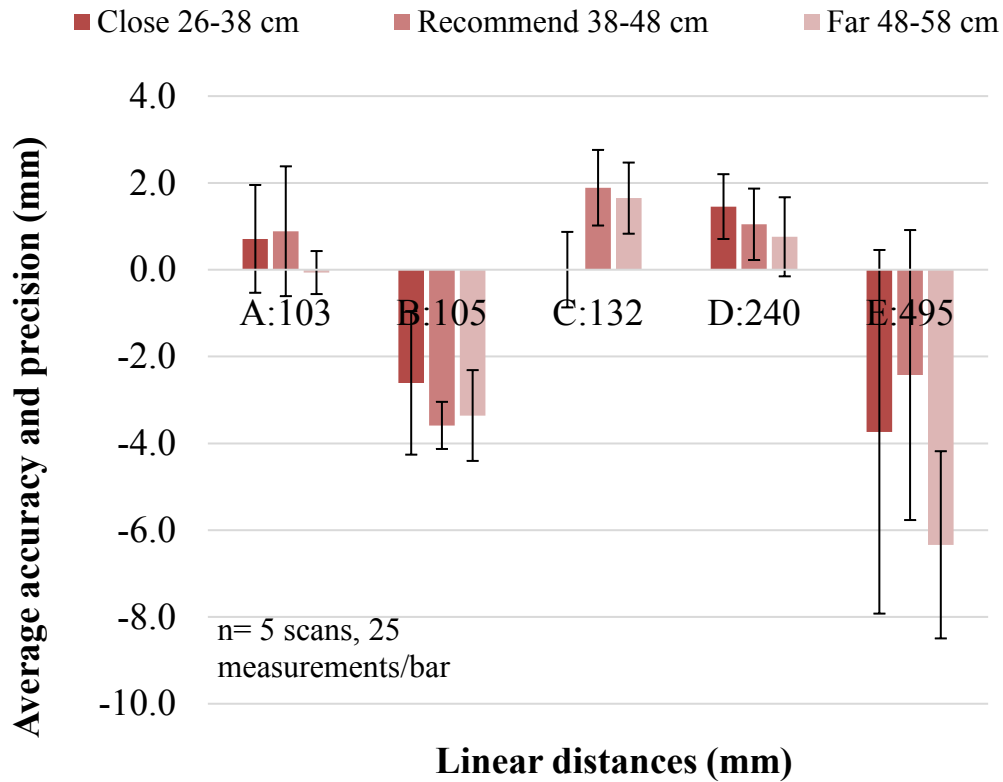
Figure 5 - 5 3D scanned torso accuracy and precision along different dimensions and scan distances.

The mean accuracy and precision of different scan distances were compared using two-tailed paired student t test. The results are shown in Table 5 - 1. No statistically significant difference was observed between the scan distances. This demonstrated the accuracy and precision of 3D scanned torso does not vary significantly with the three different scan distance ranges. The 3D scanner demonstrated better surface detectability with the recommended scan distance range, but the manufacturer had not reported accuracy and precision with the three different scan distance ranges.

Table 5 - 1 Probability values of scan distance comparison for mean accuracy and precision (n=5 for each group)

Scan distance comparison	Mean accuracy	Mean precision
Close vs. Recommended configuration	$p = 0.80 > 0.05$	$p = 0.30 > 0.05$
Close vs. Far configuration	$p = 0.43 > 0.05$	$p = 0.16 > 0.05$
Recommended vs. Far configuration	$p = 0.70 > 0.05$	$p = 0.37 > 0.05$

Note: Close configuration: 26-38 cm; Recommended configuration: 38-48 cm; Far configuration: 48-58 cm.

5.3. Investigation of 3D Scanned Torso Cross Section Accuracy and Reconstruction Accuracy at Pad Covered Regions

5.3.1. Determination of Torso Cross Section Accuracy

Three torso foam molds (Figure 5 - 6) were used to determine the 3D scanned torso cross section accuracy. Thirty markers (red dots on Figure 5 - 6) were placed on 15 horizontal levels (4 axilla, 4 thoracic, 4 trochanter and 3 lumbar levels) with 1 marker on the middle of the back and 1 on the side of the foam mold at each level.
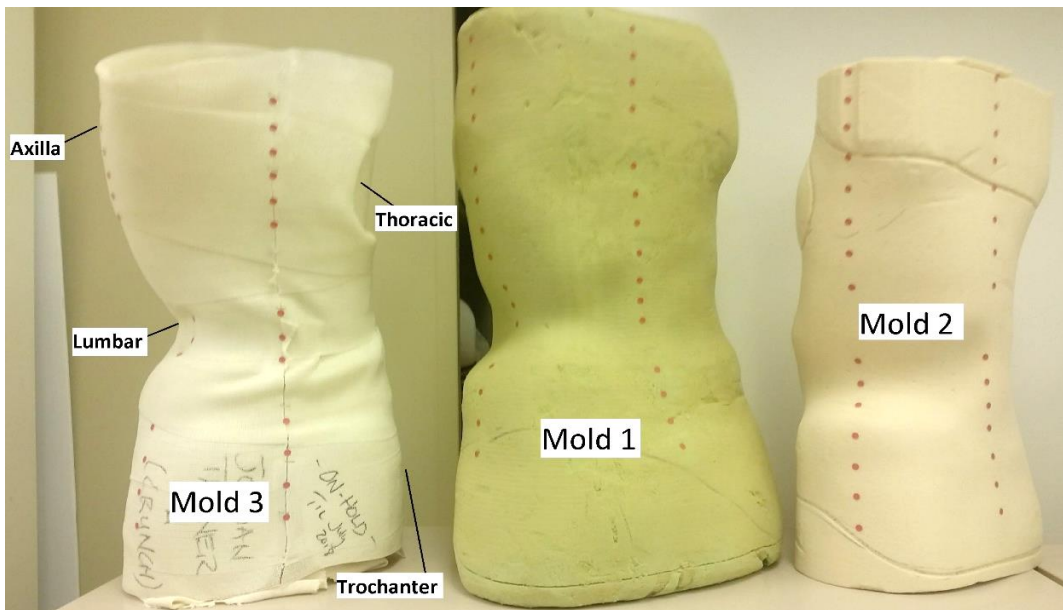
Figure 5 - 6 Three torso foam molds with foam mold number and regions labelled.

A torso mold was placed on a flat platform and the operator conducted two scans aiming for scanning at the recommended scan range (38-48 cm) (with better surface detection) around each torso mold. Scans between each torso mold were conducted at least one week apart. Black virtual markers were placed on top of scanned markers at those 15 horizontal levels for each scan to ensure horizontal alignment with grey cross section measurement line (Figure 5 - **7** (a)). Linear torso width and thickness were measured at each horizontal level with the black markers displayed on the cross-sectional view in Figure 5 - **7** (b). In Figure 5 - **7** (b), the torso width was measured from the center of the diamond shaped black marker to the furthest point (square shaped black marker) of the blue cross section contour horizontally (green line). Similarly, the torso thickness was measured from the center of the diamond shaped black marker to the furthest point (square shaped black marker) of the blue cross section contour vertically (red line). Mean absolute difference (MAD) ± standard deviation (SD) of torso width and thickness between the two repeated scans was used for evaluating the torso cross section accuracy from the three body molds.
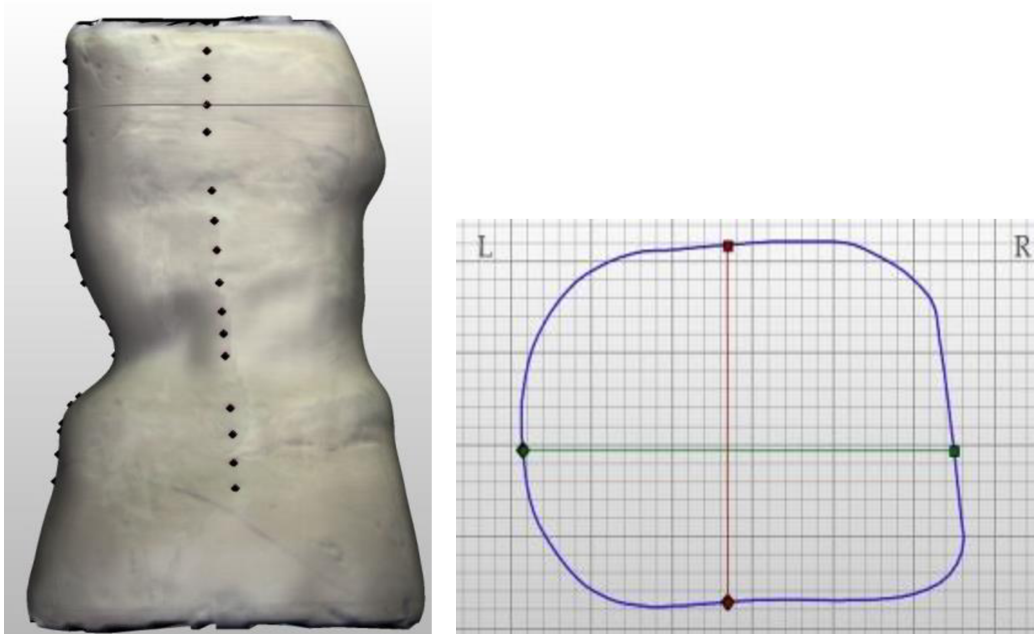
(a)   **(b)**

Figure 5 - 7 Scanned torso mold in CanFit^{TM} software. (a) Posterior view of a scanned torso mold; (b) Cross-sectional contour at a horizontal level with green horizontal line as linear torso width and red vertical line as torso thickness measurement.

5.3.2. Determination of Reconstruction Accuracy at Brace Pad Regions

The three foam molds with markers attached as shown in Figure 5 - 6 from previous section 5.3.1. were also used for determining the reconstruction accuracy at brace pad regions. A scan of a torso mold without pads applied from section 5.3.1 was used for comparing with a scan with reconstructed pad regions to determine reconstruction accuracy. The scan without pads was obtained by placing a torso mold on a flat platform and the operator scanned around the torso mold at the recommended scan range (38-48 cm). The scan with reconstructed pad regions was obtained by placing a torso mold on a flat platform inside the brace casting frame designed from chapter 4. Brace pads from the casting frame were then applied at axilla, thoracic, lumbar and trochanter regions as shown in Figure 5 - 8. The contact pressures of axilla, thoracic, lumbar and trochanter pads were 25 mmHg, 25 mmHg, 70 mmHg, and 25 mmHg, respectively, for adequate contact of torso mold while within typically applied pressure range. The operator conducted a 3D scan at the recommended

scan range (38-48 cm) around each torso mold with the pads applied. Scans between each torso mold were conducted at least one week apart.
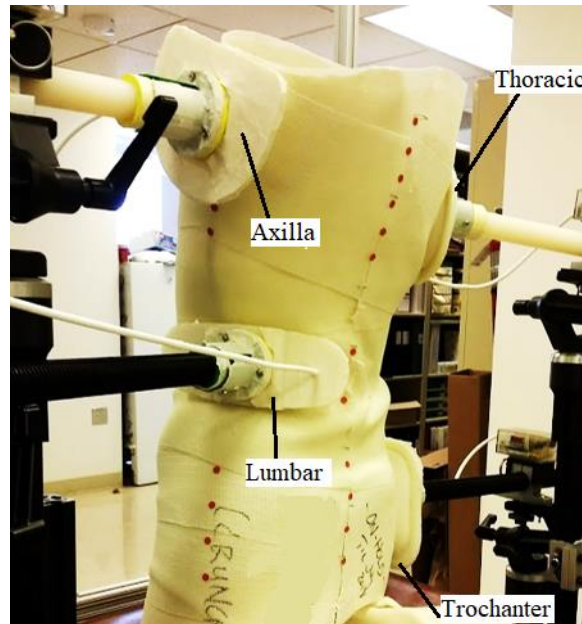
Figure 5 - 8 Pad covered body foam mold with 30 markers inside the brace casting frame.

The pad covered scans (Figure 5 - 9 (a)) were reconstructed at the pad regions (Figure 5 - 9 (b)) with the "de-feature" tool on CanFit™ software by interpolating reconstructed region based on contour of surrounding area. The scan without pads (Figure 5 - 9 (c)) was automatically aligned using the CanFit™ alignment tool with the reconstructed scan (Figure 5 - 9 (b)) for each torso mold.
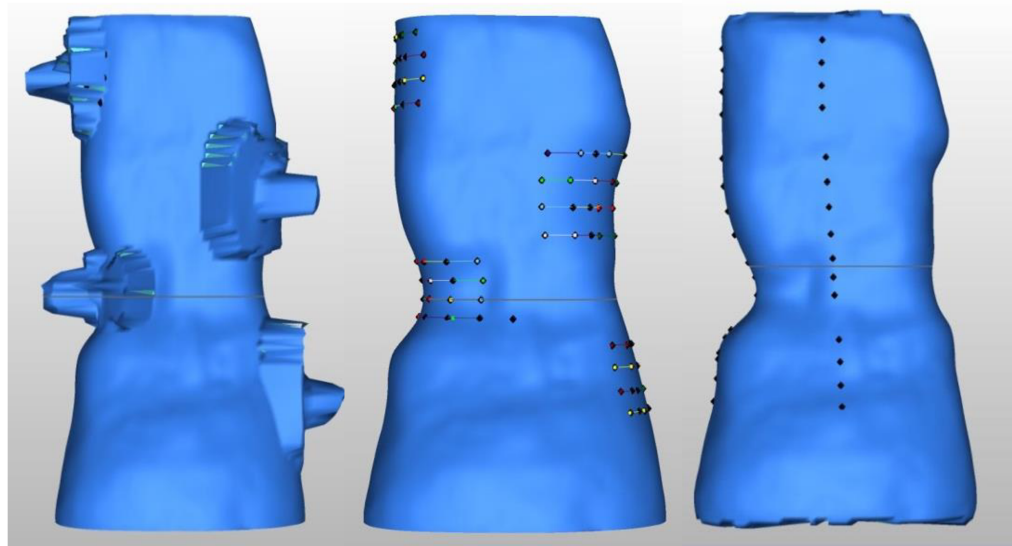
Figure 5 - 9 Torso mold scans. (a) Scan with pad cover. (b) Scan with reconstructed pad covered regions. (c) Scan without pad cover.

After that, different number of landmarks was placed virtually on each pad regions as sampling points (Figure 5 - 10 (a)) depending on the size of reconstructed region. Landmarks were placed at each of 15 horizontal levels with an additional level at lumbar region. Vertical interval between sampling points were no more than 3 cm at each reconstructed region. Horizontal interval between sampling points at each horizontal level were no more than 4 cm at each reconstructed region. The cross-sectional view of the horizontal level of the scanned torso (Figure 5 - 10 (b)) was used for deviation measurement between the scan without pad contour (red) and reconstructed contour (blue). As shown in the detail view of (Figure 5 - 10 (c)), the deviation was measured with a line that was normal to the tangent line about a sampling point. The normal line was measured from the reconstructed contour to the scan without pad contour. Mean absolute difference (MAD) ± SD was calculated with the deviation measurements from all the sampling points at each region to evaluate the body contour reconstruction accuracy.

(a)

(b)

(c)
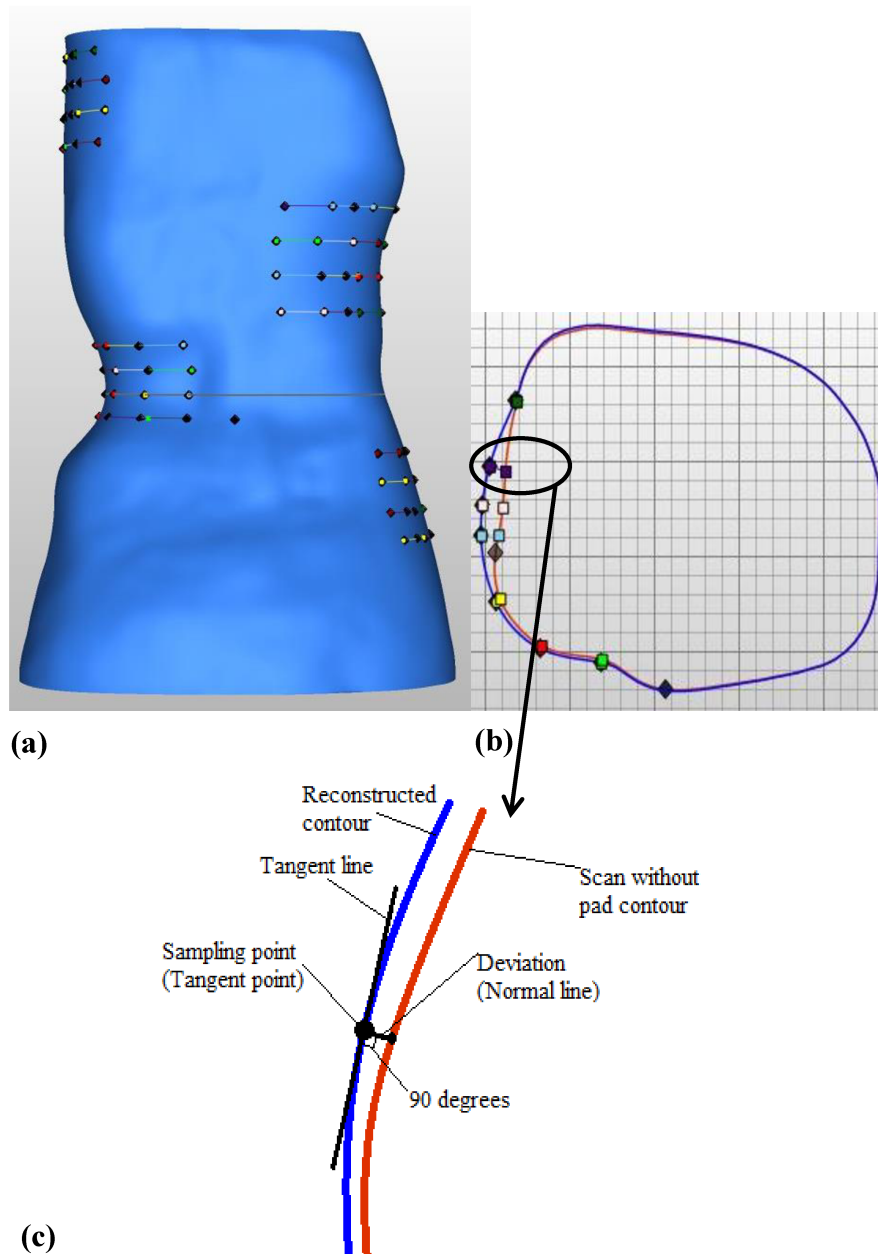
Figure 5 - 10 (a) Landmark placements on reconstructed scan. (b) Cross sectional view of scanned torso with scan without pad contour (red) and reconstructed contour (blue) aligned (c) Deviation measurement for determining reconstruction accuracy at pad covered regions.

5.3.3. Results of Torso Cross Section Accuracy and Reconstruction Accuracy at Pad Covered Regions

The accuracies of torso cross sectional width were 2.4 ± 1.8 mm, 2.1 ± 1.5 mm, 1.7 ± 1.5 mm, 2.3 ± 1.3 mm for axilla, thoracic, lumbar and trochanter regions between the three body molds. The accuracies of torso cross sectional thickness were 1.3 ± 0.3 mm, 0.8 ± 0.1 mm, 0.6 ± 0.3 mm, 1.0 ± 1.2 mm for axilla, thoracic, lumbar and trochanter regions between the three body molds. The overall accuracies of the torso cross section width and thickness between the three body molds were 2.2 ± 0.3 mm and 0.9 ± 0.2 mm, respectively. Figure 5 - 11 shows the MAD ± SD reconstruction accuracy based on deviations between scan without pad and scan with reconstructed pad regions at four different pad regions. In Figure 5 - 11, the horizontal axis includes labels for each pad covered regions and the vertical axis represents the MAD. Each pad region was categorized into results from three different body molds. No specific pattern was observed for reconstruction accuracy with different pad regions or bold mold. Reconstruction accuracy was within 25 mm for axilla, lumbar and trochanter regions, and within 10 mm for thoracic region.
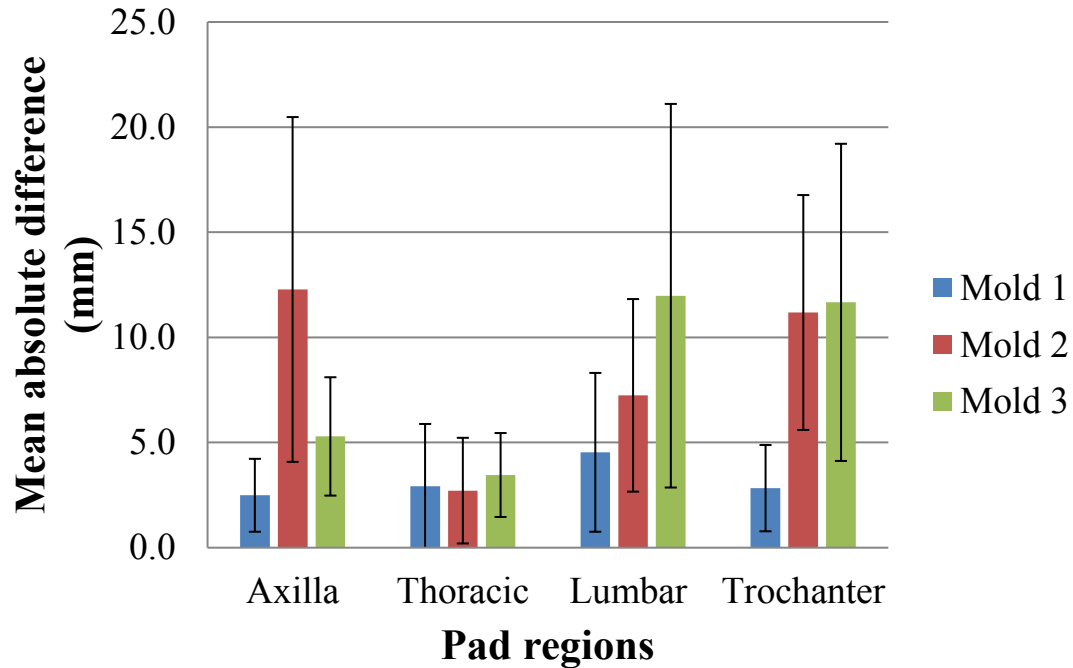
Figure 5 - 11 MAD reconstruction accuracy at each pad region (Mold 1: axilla n=23, thoracic n=24, lumbar n= 21, trochanter n=23; Mold 2: axilla n=20, thoracic n=24, lumbar n=23, trochanter n=26; Mold 3: axilla n=22, thoracic n=27, lumbar n=23, trochanter n=27; where n is the number of sampling points on the pad region).

Reconstruction accuracy contour plots for all pad regions of the three body molds were generated and examined for finding any noticeable accuracy pattern based on linear interpolation of red and black sampling points. The black sampling points were placed based on the spacing intervals described in section 5.3.2. The red sampling points were additional sampling points added on a horizontal level to indicate the maximum deviation value between the scan with pad and reconstructed contour as shown in Figure 5 - 10 (b). Contour plots at all pad covered regions of bold mold 1 were shown in Figure 5 - 12 to Figure 5 - 15 to give a general idea of accuracy at all reconstructed regions of a scanned torso. The contour plot lines were 1 mm apart and the origin of the contour plot was at the furthest left point of the top horizontal level. It was found that reconstruction accuracy pattern varied between body molds and pad regions with different surface contours. However, at lumbar region, the poorest accuracy appeared to be at the most concave yellow region at the center horizontal level (Figure 5 - 14, Figure 5 - 16 and Figure 5 - 17). Positive

deviations indicating outward bulge of reconstructed torso contour were $6 \pm 10\%$, $36 \pm 30\%$, $85 \pm 2\%$, and $13 \pm 23\%$ of sampling points in the axilla, thoracic, lumbar and trochanter regions, respectively.
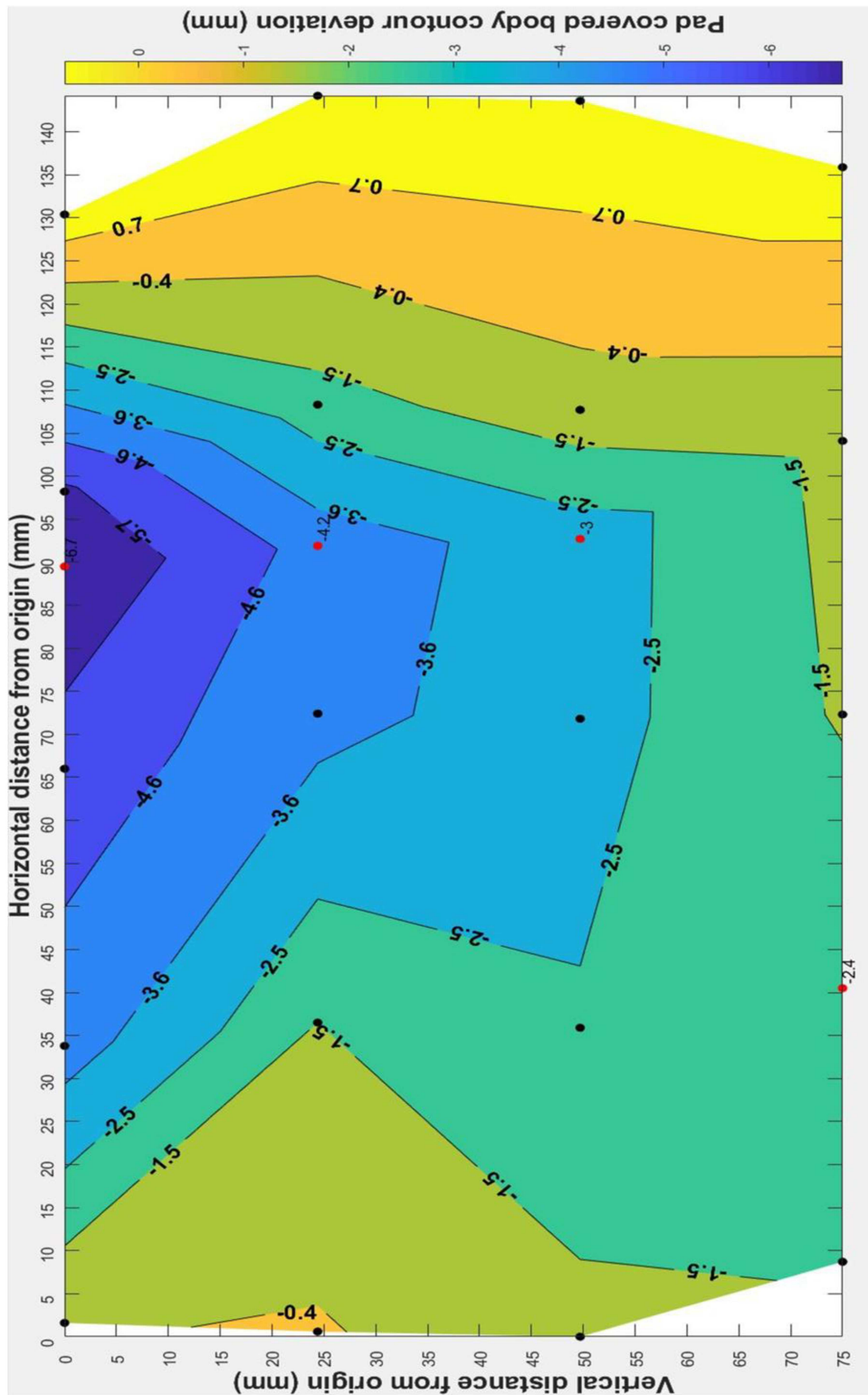
Figure 5 - 12 Reconstruction accuracy contour plot at axilla pad region for foam mold 1.
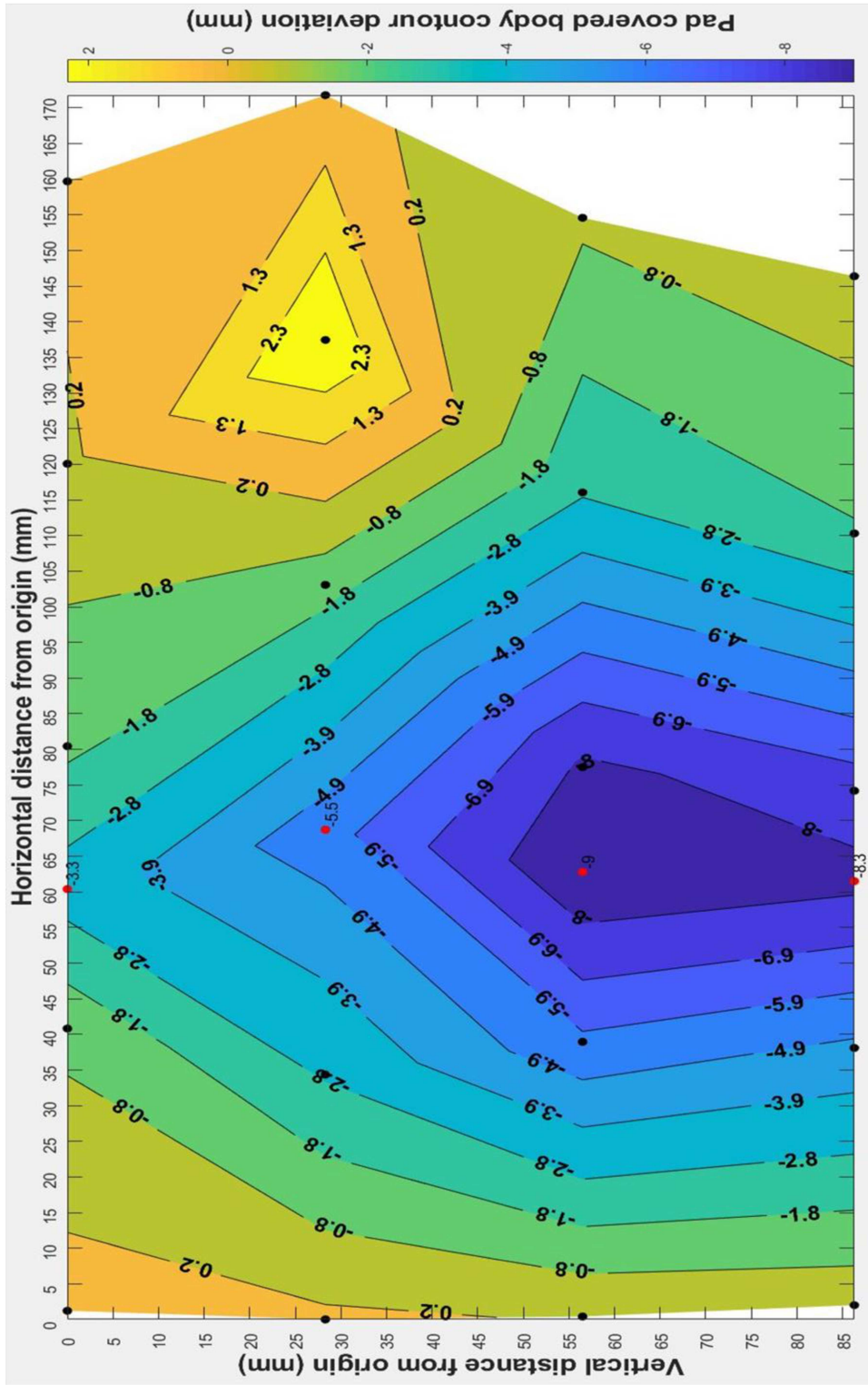
Figure 5 - 13 Reconstruction accuracy contour plot at thoracic pad region for foam mold 1.
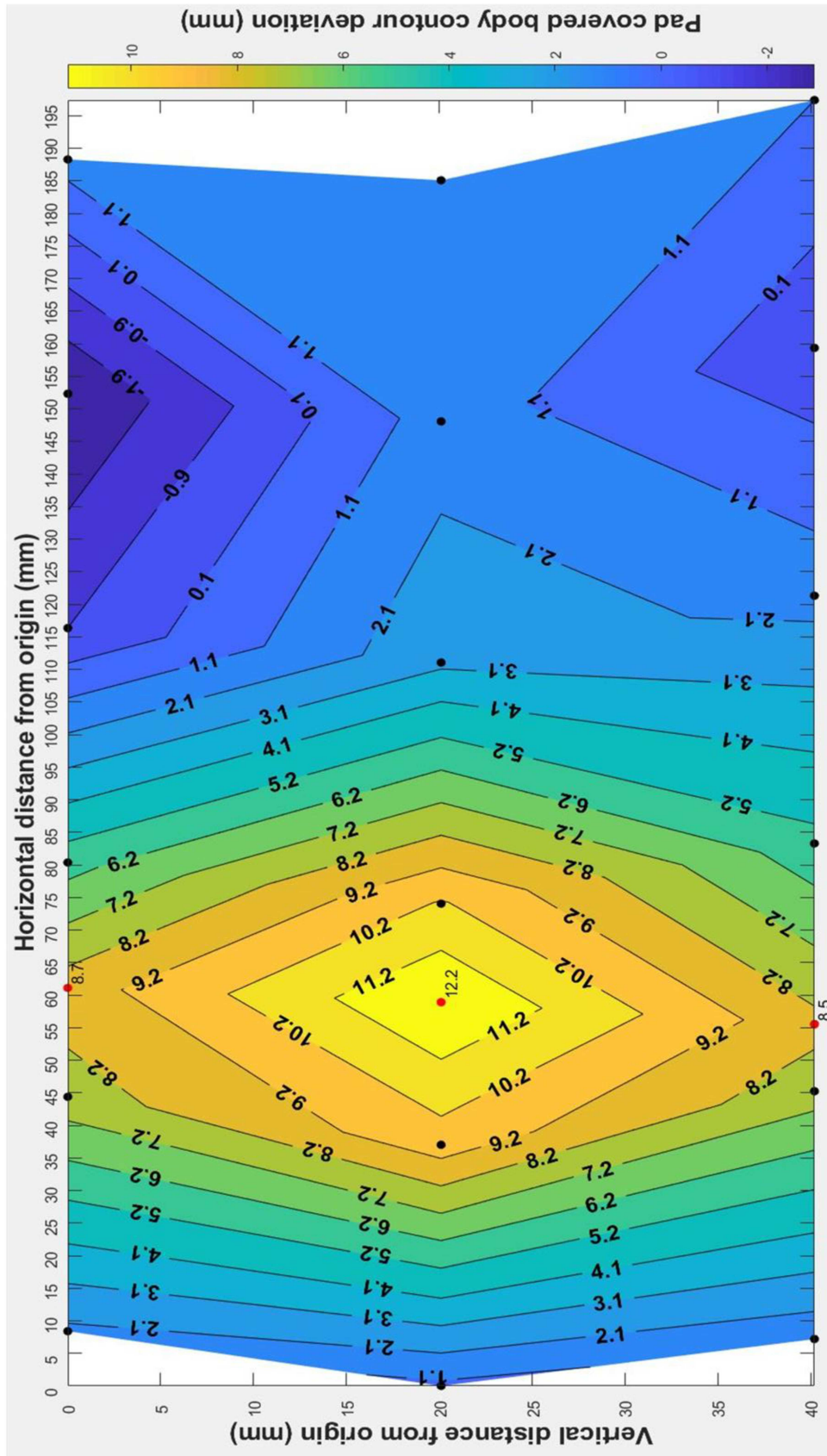
Figure 5 - 14 Reconstruction accuracy contour plot at lumbar pad region for foam mold 1.
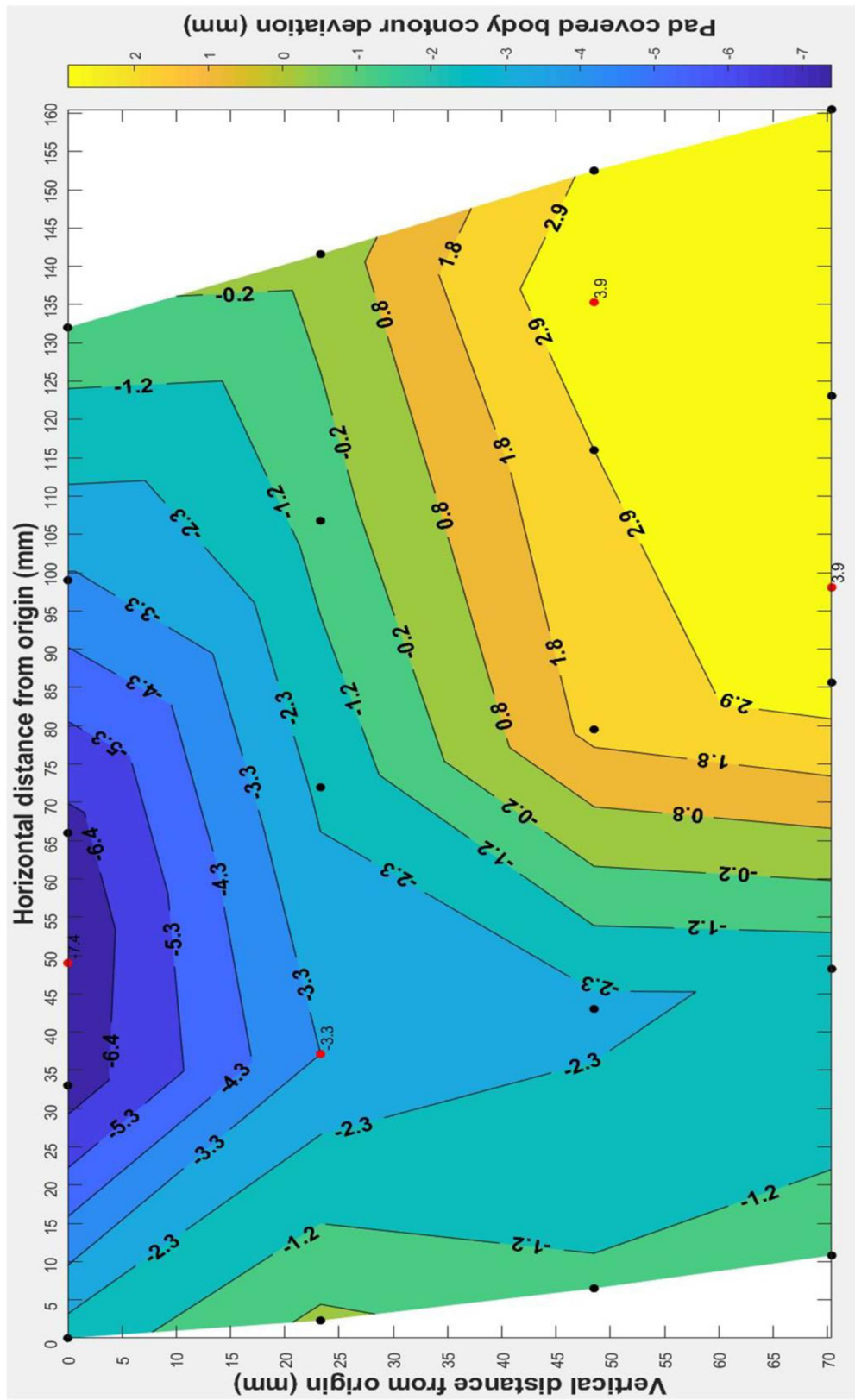
Figure 5 - 15 Reconstruction accuracy contour plot at trochanter pad region for foam mold 1.
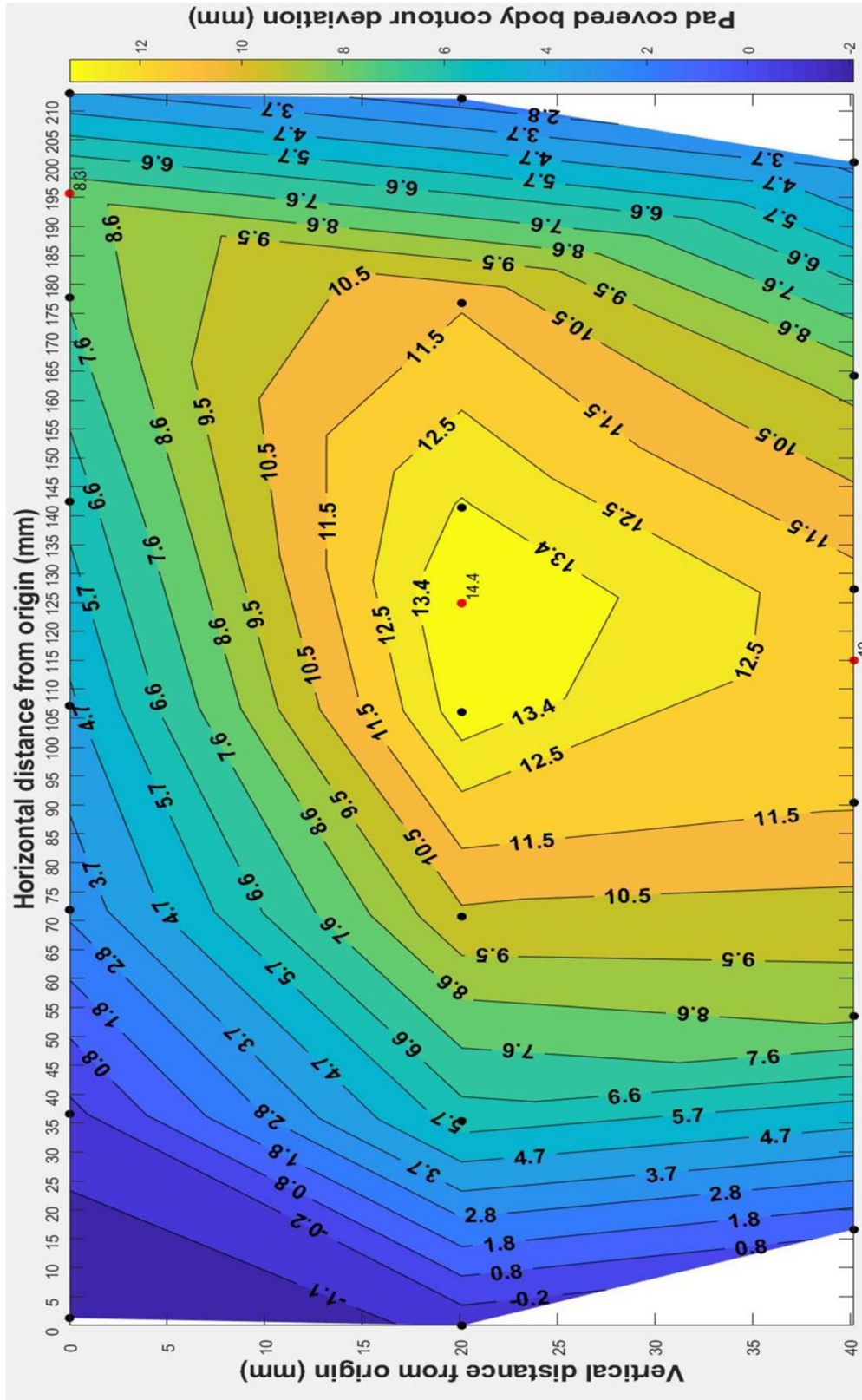
Figure 5 - 16 Reconstruction accuracy contour plot at lumbar pad region for foam mold 2.
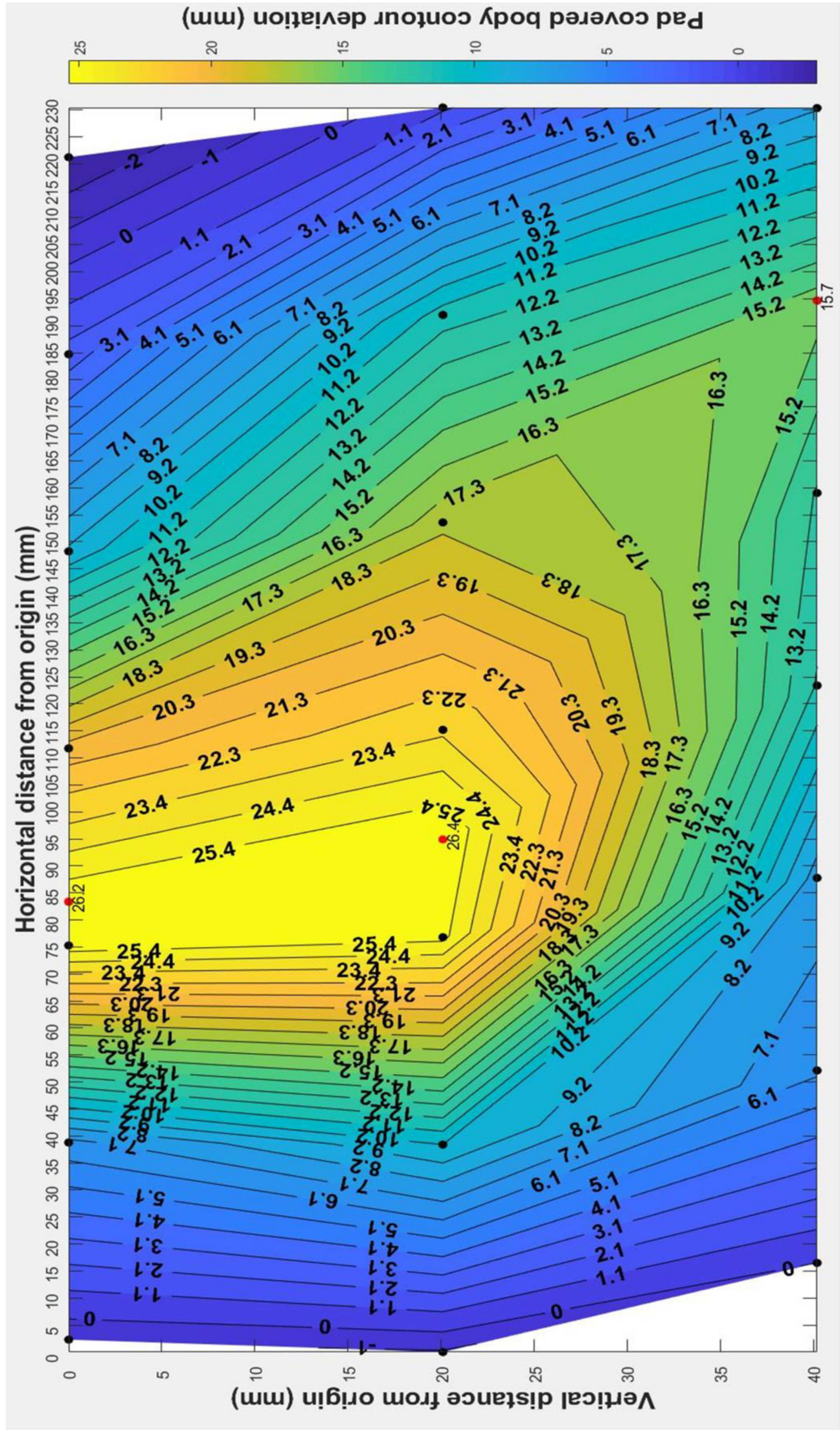
Figure 5 - 17 Reconstruction accuracy contour plot at lumbar pad region for foam mold 3.

5.4. Interpretation of 3D Scanned Torso Evaluation Results[*]

Higher accuracy and precision were found for shorter dimensions on the scanned torso except for dimension B that will be explained in section 5.5. This demonstrated shorter dimensions on a scanned torso were captured with more accuracy and precision compared to longer dimensions. No statistically significant difference was found for mean accuracy and precision between different scan distances ranges. This demonstrated that scanned torso had adequate accuracy outside of recommended scan distances ranges, which allowed more flexibility in the scanning process.

Different reconstruction accuracies were found between different torso molds and pad covered regions illustrated in the accuracy contour plots. Nevertheless, there was a general pattern among the three scanned torso molds, where the poorest accuracy of lumbar pads was at the most concave center region. This demonstrated poorer reconstruction accuracy for torso shapes with greater concave curvatures. It was also found that reconstructed body contour at lumbar region showed high percentage of outward bulge ($85 \pm 2\%$). This was also illustrated on Figure 5 - 14, Figure 5 - 16 and Figure 5 - 17 with mostly positive deviation indicating outward bulge with reconstruction at lumbar region. This result could help orthotists in modification of brace shape at concave lumbar region by inward compression with region tool in the CanFit^{TM} software.

Scanned torso accuracy and precision along different dimensions and scan distances were within 1 cm which is within the clinical accepted range. Similarly, the accuracy of the torso cross section width and thickness were also within clinical accepted range. However, reconstruction accuracy for axilla, lumbar, and trochanter regions of mold 2 as well as lumbar and trochanter regions of mold 3 exceeded the 1 cm clinical accepted range. Mold 2 and 3 had worse reconstruction accuracy than mold 1 at axilla, lumbar, and trochanter regions. Based on observation of the surface contour of the three torso molds, mold 2 and 3 had surface contour with more curvature at brace pad regions. This might suggest that

reconstruction accuracy was dependent on surface contour curvature, with greater curvature resulting in worse accuracy.

5.5. Limitations of Study[*]

A limitation of this study was the placement of reflective markers on curved torso surface as shown in Figure 5 - 18. In Figure 5 - 18, pairs of reflective markers were placed on three different torso surfaces. A large tilt angle of reflective marker on curved torso surface (Figure 5 - 18 (c)) could be a source of error. That's because the reflective markers were spherical, and the motion capture cameras measured the center to center distance of the 3D spherical marker. On the other hand, only a 2D flatten spherical markers surface could be captured by the 3D scanner and the measurements were between the center to center distance of the flatten marker surface on the torso mold. Even though offset values had been applied on the motion capture measurements for comparison with 3D scanner measurements, a larger angle would introduce a larger error. This could explain the poorer accuracy value for a short dimension B, which had the largest total tilt angle of 49 degrees compared to all the other dimensions evaluated. Another limitation of this study included the use of body molds instead of human subjects. The phantom study did not account for the motion effects of human subjects including breathing moments and swaying of the body. In particular, for the evaluation of reconstruction accuracy at pad covered regions, a torso mold had minimal contour change with brace pad applied compared to a human subject which would affect results.
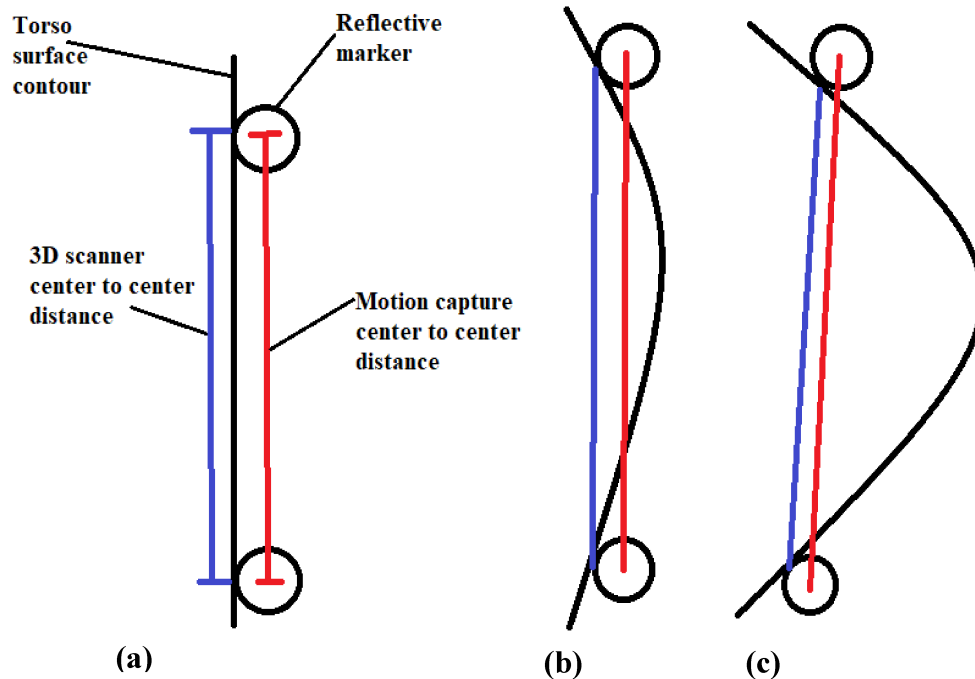
Figure 5 - 18 Different orientations of reflective marker placement on torso surface. (a) Vertical surface contour (zero marker tilt angle). (b) Curved surface contour (small marker tilt angle) (c) Significantly curved surface contour (large marker tilt angle)

5.6. Design of a New 3D Printed Brace Casting and Manufacturing Process

5.6.1. Casting and Manufacturing Process Components

Following evaluation of the 3D scanner, determination of 3D printing parameters, the development of brace casting frame and dynamic brace pads, a new brace casting and manufacturing process was proposed. Brace casting process is defined as the procedures required to obtain the patient body contour. Brace manufacturing process refers to the procedures required to create a brace from the acquired patient body contour as well as fitting and measurement of in-brace corrections. The proposed novel brace casting and manufacturing process involves various existing and new components. In this section, key components are highlighted for better understanding of the casting and manufacturing steps described in the next section. Existing components that had been previously used and tested in the research group include a medical ultrasound (U/S) system, custom U/S measurement software (MIAS), four pump/valve pressure monitors that are wirelessly controlled by an iPad, and a 3D EOS radiography unit as shown in Figure 5 - 19. New components

developed for the manufacturing process include four providence shaped 3D printed dynamic brace pads and a brace casting frame with four brace pad mounts included. Other new components used include a 3D scanner, the CanFit^{TM} brace shape modification software and a FORTUS 900mc production type 3D printer as shown in Figure 5 - 20.

(a)

(b)

(c)

(d)

(e)
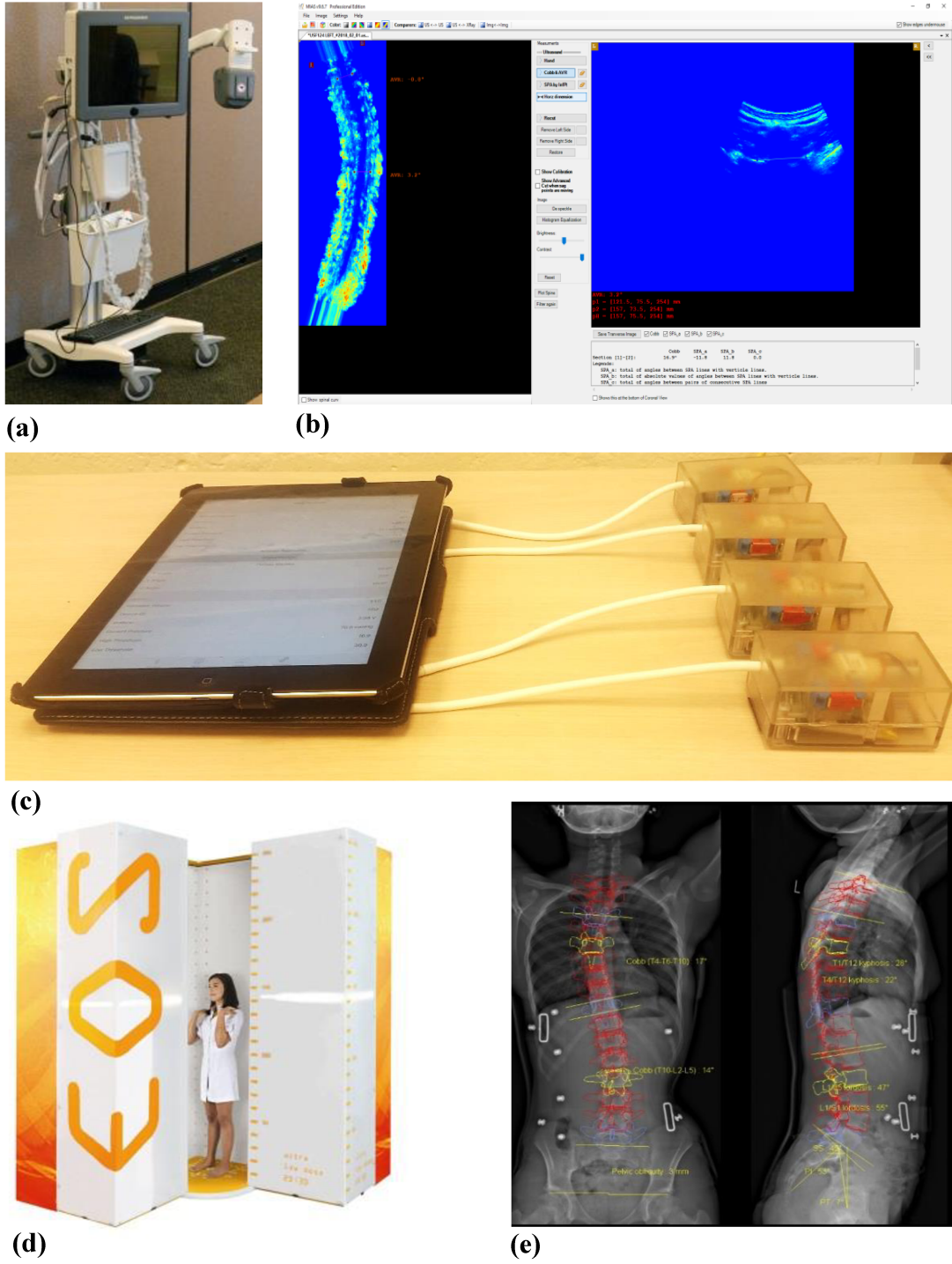
Figure 5 - 19 Existing components of 3D printed brace casting and manufacturing process. (a) Medical ultrasound (U/S) system [66]. (b) Custom U/S measurement software (MIAS). (c) Pump/valve pressure monitors controlled by an iPad. (d) 3D EOS radiography unit [145]. (e) 3D EOS measurement software.
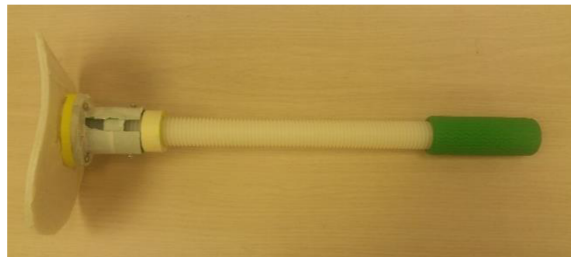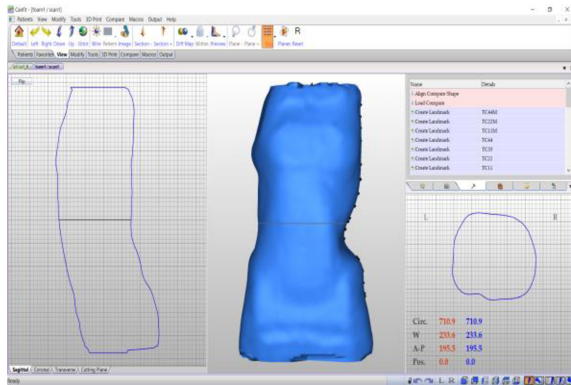
Figure 5 - 20 New components of 3D printed brace casting and manufacturing process. (a) 3D printed dynamic brace pads. (b) Brace casting frame. (c) Brace pad mount. (d) Vorum Spectra 3D scanner. (e) Brace shape modification software (CanFit™). (f) Production 3D printer (FORTUS 900mc) [146].

5.6.2. 3D Printed Brace Casting and Manufacturing Process

Figure 5 - 21 shows a developed clinical protocol for 3D printed brace casting and manufacturing processes. The proposed brace casting process includes ultrasound measurement of spinal curves for guiding optimal placement and applied force of dynamic brace pads with steps 1 to 8. Dynamic brace pads are used in measurement and maintaining pressure level during the casting process in step 5b) and step 7b). Lastly, the casting process includes acquiring patient body contour at the optimal pad configuration with a 3D scanner. The estimated time for the brace casting process during the brace casting clinic with the new procedure is about 45 minutes, similar to the traditional brace casting clinic of 1 hour.

The proposed brace manufacturing process (step 10 to 13 in Figure 5 - 21) includes brace shape modification with software, 3D printing the brace with brace shape file, brace fitting and measurement of in-brace corrections. A 3D printed brace will be created within 1 month after the brace casting clinic. This is similar to the traditional brace deliver time for patient fitting. Attaching accessories and brace adjustments in step 11 are estimated to be done in about 30 minutes at the brace fitting clinic similar to the traditional brace. After that, in-brace radiography will be taken about 4- 6 weeks following the brace fitting clinic. This new casting and manufacturing process in creating a 3D printed brace will be evaluated in the next chapter.
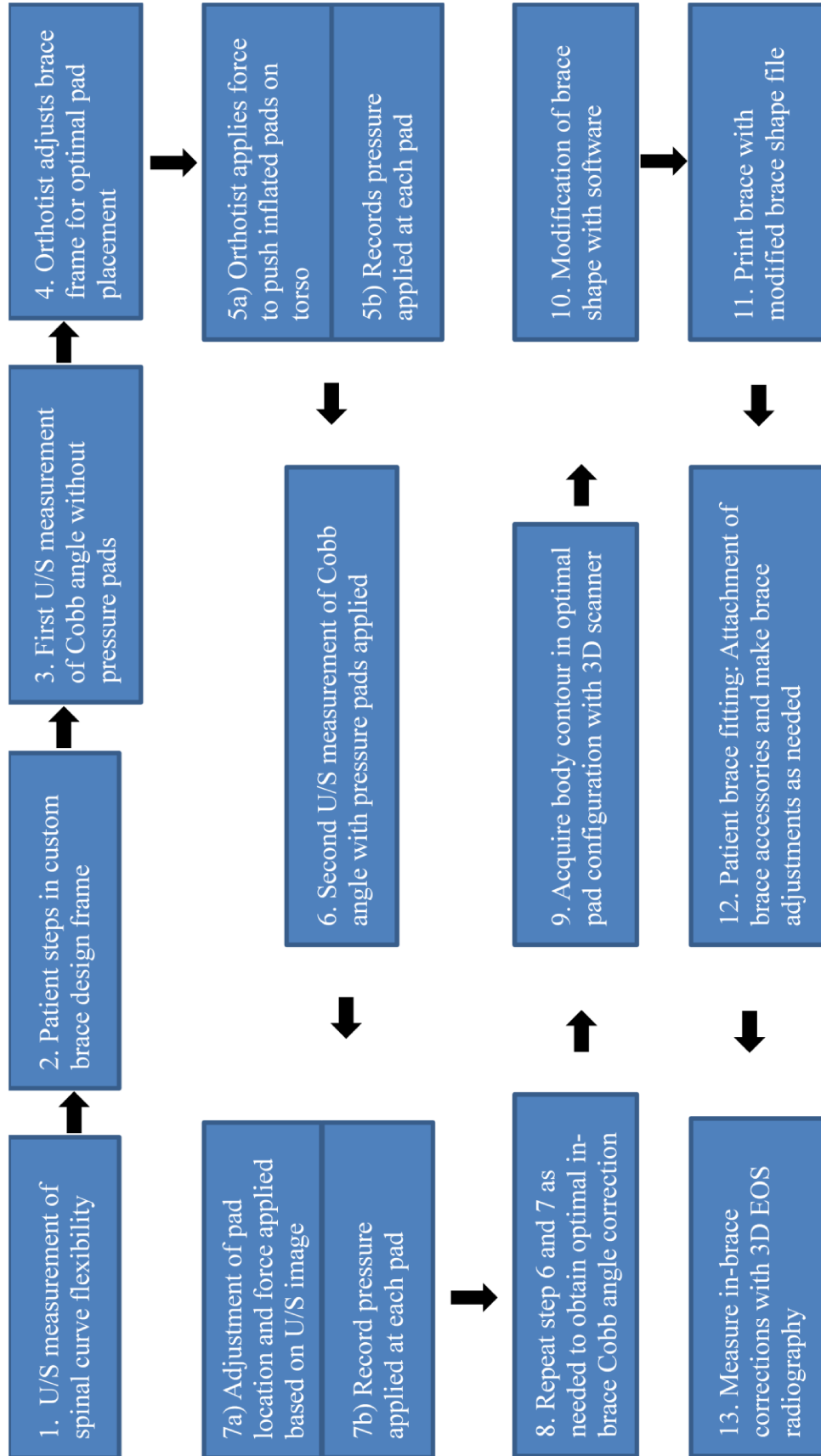
Figure 5 - 21 Work flow of 3D printed brace casting and manufacturing process.

1. U/S measurement of spinal curve flexibility

2. Patient steps in custom brace design frame

3. First U/S measurement of Cobb angle without pressure pads

4. Orthotist adjusts brace frame for optimal pad placement

5a) Orthotist applies force to push inflated pads on torso
5b) Records pressure applied at each pad

6. Second U/S measurement of Cobb angle with pressure pads applied

7a) Adjustment of pad location and force applied based on U/S image
7b) Record pressure applied at each pad

8. Repeat step 6 and 7 as needed to obtain optimal in-brace Cobb angle correction

9. Acquire body contour in optimal pad configuration with 3D scanner

10. Modification of brace shape with software

11. Print brace with modified brace shape file

12. Patient brace fitting: Attachment of brace accessories and make brace adjustments as needed

13. Measure in-brace corrections with 3D EOS radiography

Chapter 6: Investigation of 3D Printed Brace Effectiveness and Manufacturing Process Outcome

This chapter reports the background, objectives, methodologies and study design of a randomized controlled trial (RCT) to investigate 3D printed brace effectiveness and the evaluation of the brace manufacturing process in section 6.1. Section 6.2. reports the preliminary results of the RCT which includes pre-brace patient demographics, in-brace corrections of treated curves, wear time compliance, manufacturing time, cost, and brace design parameters of the intervention and control groups. Section 6.3. discusses the limitations of the study; section 6.4. reports the challenges encountered with the manufacturing of 3D printed brace. Section 6.5. summarizes the preliminary results from the RCT.

6.1. A RCT to Investigate the Effectiveness of 3D Printed Brace and Brace Manufacturing Process Evaluation

Following chapters 3, 4, and 5, a RCT was designed and conducted to a) validate the effectiveness of the 3D printed brace and b) evaluate the new 3D brace manufacturing process. Regarding to the brace effectiveness, the immediate in-brace corrections and the patients' brace wear time were compared between the intervention and control groups from the RCT. Regarding to the brace manufacturing process, the entire manufacturing time, both labor and material costs and brace design parameters between the 3D printed and traditional braces were compared.

6.1.1. RCT Inclusion Criteria

The inclusion criteria of this study are based on the guidelines recommended by the Scoliosis Research Society Committee on bracing management for standardizing AIS brace studies [9]. Recruited patients were a) diagnosed with adolescent idiopathic scoliosis (AIS), b) prescribed with a full time TLSO (23 hours), c) between 10-16 years old, d) pre-menarchal or < 1 year post-menarchal for female, and had e) Cobb angle between 20-45°, f) Risser sign< 3. Risser sign is determined from posterior-anterior radiography for classifying the skeletally maturity of scoliosis patient by the degree of ossification or fusion at the iliac crest as shown Figure 6 - 1. Figure 6 - 1 demonstrates a patient with Risser 2.

Risser 0 and 2 demonstrates patient during rapid growth spurt while Risser 4 and 5 demonstrates patient who have stopped growing. At Risser 5, there will no longer be visible gap at the iliac crest shown on the radiograph indicating fusion at iliac crest has occurred. According to the guidelines, a complete study to evaluate brace effectiveness includes percentage of patients with ≤ 5 degrees Cobb angle at skeletally maturity, percentage of patients with spinal curves not exceeding 45 degrees Cobb angle at skeletally maturity, percentage of patients who have not undergo surgery two years following treatment and brace wear compliance of all patients.

Figure 6 - 1 Posterior-anterior radiograph for determining Risser sign (1-5) based on ossification or fusion at the iliac crest where this radiography demonstrates patient with Risser 2 [147].

6.1.2. Study Design: Traditional TLSO and 3D Printed Brace Groups

Patients who met the inclusion criteria and consented to participate in the study were randomly assigned by drawing between the traditional TLSO (control) group and the 3D printed brace (intervention) group from the research coordinator. During the brace casting clinic for obtaining body contour, patients from both groups received standing ultrasound (U/S) scans as a baseline measurement and prone bending positions' scans to determine spinal flexibility as shown in Figure 6 - 2. Figure 6 - 2 (a) shows the baseline standing U/S scan with a right, main thoracic curve of 20 degrees Cobb angle. Figure 6 - 2 (b) shows the prone bending to the right U/S scan which resulted in a left spinal curve of 22 degrees Cobb

angle. Prone bending position involved patient bending in the curve direction as far as possible to produce maximum curve correction. Estimate maximum curve correction (EMCC) was used for measuring spinal flexibility similar to other studies [148], [149]. The EMCC was calculated as:

$$EMCC = \frac{US\ standing\ Cobb\ angle - Bending\ US\ Cobb\ angle}{US\ standing\ Cobb\ angle} * 100 \qquad [6\text{ - }1]$$

(a)   (b)
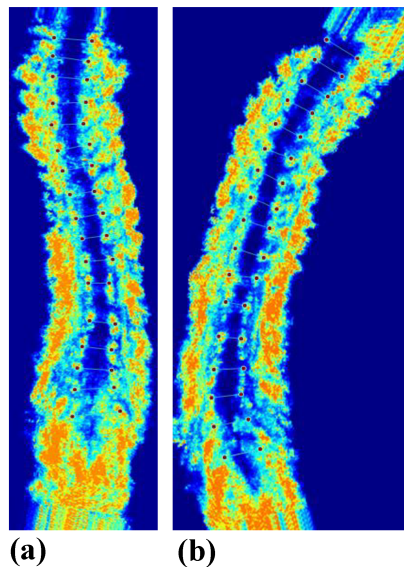
Figure 6 - 2 Ultrasound scans for spinal flexibility measurements. (a) Baseline standing ultrasound; (b) Prone bending ultrasound.

A novice rater was trained by an experience rater on measurement of spinal parameters on U/S images. The novice rater had 4 months experience on measurement of spinal parameters on U/S images. Also, the novice rater had measured 10 U/S images prior to this study and compared with clinic radiograph measurement with a high reliability of R = 0.81. The novice rater measured the baseline standing and prone bending U/S images once for this study while blinded to clinic radiograph measurements. Afterwards, the measurements were compared with clinical radiographic measurements to verify measurements reliability. The center of lamina method (COL) was used to measure the spinal curvatures. The prone bending measurements had used the same upper and lower end vertebrae as the baseline standing measurement. The baseline standing and prone bending U/S images were

measured using the Medical Image Analysis Software (MIAS), a custom software developed in-house. Once the baseline curvature and spinal flexibility information were obtained, the intervention subject was instructed to stand in the middle of the brace casting frame. Orthotist applied pressure pads with the standing brace casting frame to specific locations onto patient torso to correct the spinal curve in 3D based on the baseline curvature and spinal flexibility information. Pressure at thoracic, lumbar, axilla and trochanter regions were measured by the dynamic brace pad and pressure monitors as described in chapter 4. A U/S scan would be taken and the Cobb angle of spinal curve measured while the pads were applied on patient torso. After reviewing the U/S measurements and casting pad pressures, the orthotist would readjust the pad placement and applied pressure. Another new U/S scan would be taken, the Cobb angle of spinal curve would be measured, and the new casting pressure values recorded.

After the orthotist was satisfied with the curvature correction viewed from the ultrasound, the Vorum Spectra handheld scanner described in chapter 5 was used to obtain the body contour of the recruited patients with the latest pad configuration applied. The orthotist then modified the body contour files generated with custom CanFit^{TM} software (Vorum, Vancouver, Canada) using specific tools as shown in Figure 6 - 3. The software modifications worked with a raw scan file shown in Figure 6 - 3 (a), where the four brace pads applied to the torso remained on the scan body contour. The raw scan included the odd shape contours at the top and bottom ends that were automatically connected during scanning. The wrinkles of the stockinet worn by the patient could also be seen on the raw scan. Figure 6 - 3 (b) shows the body contour after using the cut ends tool to remove the connected contours from the top and bottom ends to create a hollow structure, lengthening tool was used to provide sufficient brace height after removal of top and bottom ends, and the defeature tool was used to remove the brace pads for revealing the body contour underneath. Figure 6 - 3 (c) shows the body contour after using the smoothing tool to remove wrinkles and sharp edges from the body contour. The region tool was used afterwards to add relieve and pressure regions on the brace shape for passive and active correction of spinal curve as mention in chapter 2. Figure 6 - 3 (d) shows the final brace shape after using the trim line tool for cutting out the brace shape at the proper height at the bottom end to avoid interference with patient seating. As well, the trim line tool was

used to add the top flap for correction of a thoracic spinal curve from the patient. The thickness tool was used to generate uniform 3D printing thickness of 3 mm for the entire brace shell and a variable 5 mm 3D printing thickness at the bottom of the top flap for extra stiffness at the region. The raw body contour (red outline) and the final modified brace shape (blue outline) in the coronal and sagittal plane are shown in Figure 6 - 4.
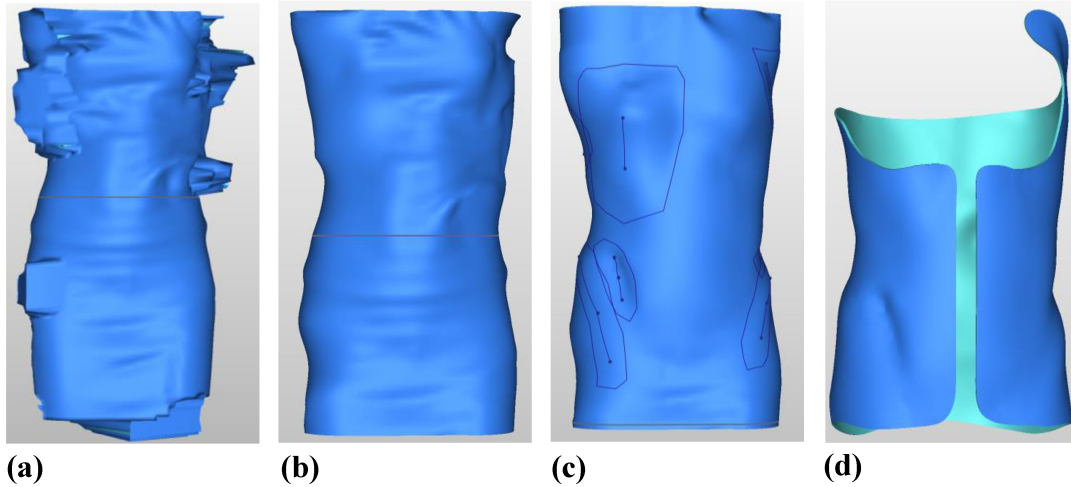
(a)　　　　　　　　**(b)**　　　　　　　　**(c)**　　　　　　　　**(d)**

Figure 6 - 3 Software modification from body contour file to brace shape file. (a) Raw body contour file. (b) After cut ends, lengthening and defeature tool. (c) After smoothing and region tool. (d) After trim line and thickness tool.

<div align="center">(a)   (b)</div>
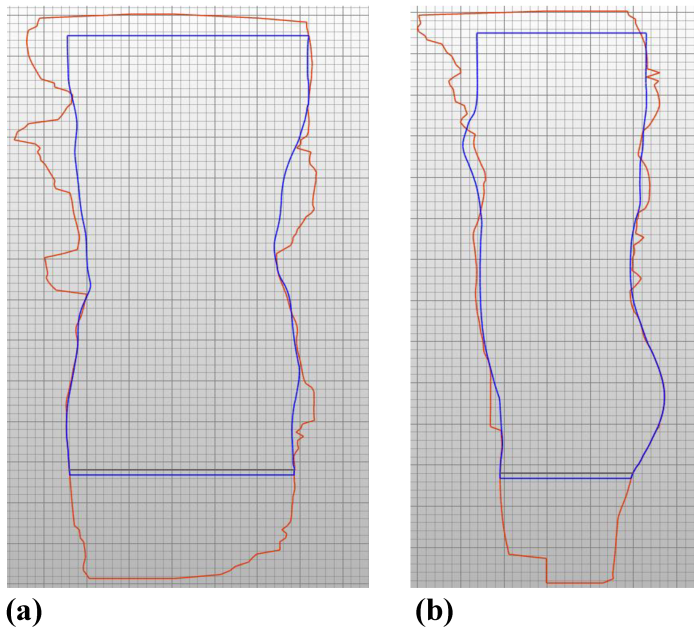
Figure 6 - 4 Coronal and sagittal plane body contours in modification software. (a) Coronal plane body contour. (b) Sagittal plane body contour.

The final brace shape file in STL format outputted from the CanFit^{TM} software was uploaded to Insight software (Stratasys Ltd., Minnesota, USA) for modifying print settings and generating toolpaths for 3D printing as shown in Figure 6 - 5. Figure 6 - 5 (a) shows the toolpath of a layer in the middle of a printed brace. Some custom print settings used for the brace are shown in Table 6 - 1. The part interior fill style listed on Table 6 - 1 refers to the infill pattern of a layer of the brace as shown in Figure 6 - 5 (b). The number of perimeters from Table 6 - 1 refers to the number of outer boundaries of a layer of the brace as shown in Figure 6 - 5 (b). Figure 6 - 5 (b) shows that the brace shell print setting has solid interior fill style with close to 100% crisscross infill pattern, and the edge of the brace shell always have 2 lines of outer perimeters. Figure 6 - 5 (a) shows the support material required of that layer as slated lines on the right of the figure. The spikes with arrows are additional support structure along the height of the brace for preventing swaying of the brace for a tall print. The brace shape print setting and toolpath files in specialize file formats were sent to Forge Labs Inc. (Vancouver, Canada) for 3D printing the brace using a FORTUS 450mc machine. After printing, the brace was submerged in a solution which

consists of heated water mixed with cleaning agent for dissolving support materials. The 3D printed brace was created after the removal of support material.

(a)

(b)
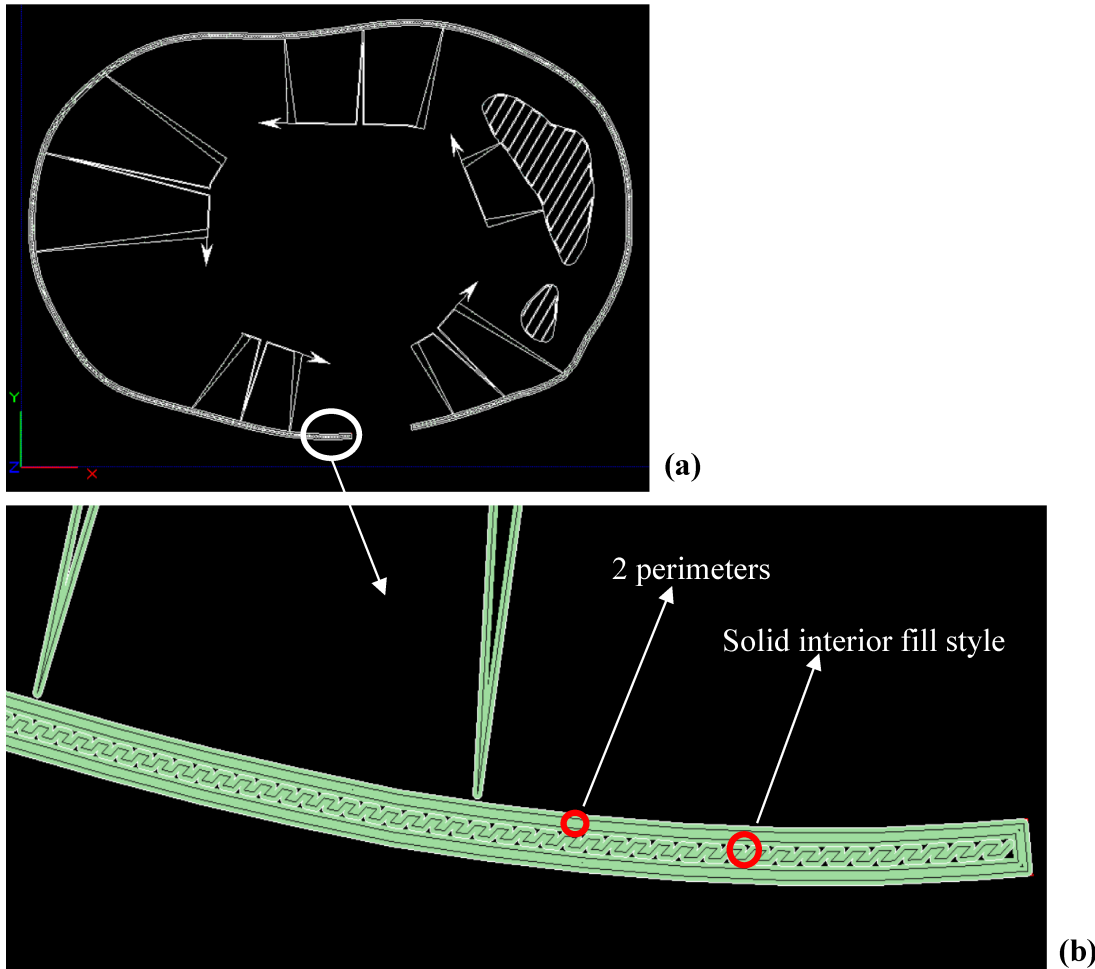
Figure 6 - 5 Snapshots of Insight software using a FORTUS 450mc machine with brace shape uploaded. (a) Toolpath for printing a layer of the brace. (b) Zoom in view of the toolpath of a layer of the brace.

Table 6 - 1 Print settings on Insight software for 3D printing a brace

Part interior fill style	Solid
Number of perimeters	2
Perimeter width	0.5 mm
Part infill width	0.5 mm
Layer height	0.25 mm
Model material	Nylon12
Support material	SR-110

On the other hand, patients from the traditional TLSO group used the Providence casting system to obtain body contour after the spinal flexibility evaluation. The Providence casting system shown in Figure 6 - 6 allows mainly 2D correction of spinal curvatures with patient in supine position. The spinal curve severity could also be underestimated during the casting process with reduction in curve severity lying down compared to standing due to change of gravitational effect on the spine. Plaster wraps were applied around the patient torso and the orthotist applied casting pads on the plaster wrap. The plaster wrap mold was hardened to patient body contour and cut off from the patient. After that, reflective stickers were placed on plaster mold for 3D scanning. A handheld scanner was used to obtain the plaster mold shape file. The file was used for the carving machine to create a positive foam mold. Polypropylene sheet was thermo-vacuum formed around the foam mold to form a cylindrical brace tube. Orthotist then trimmed the polypropylene brace tube to form a TLSO.
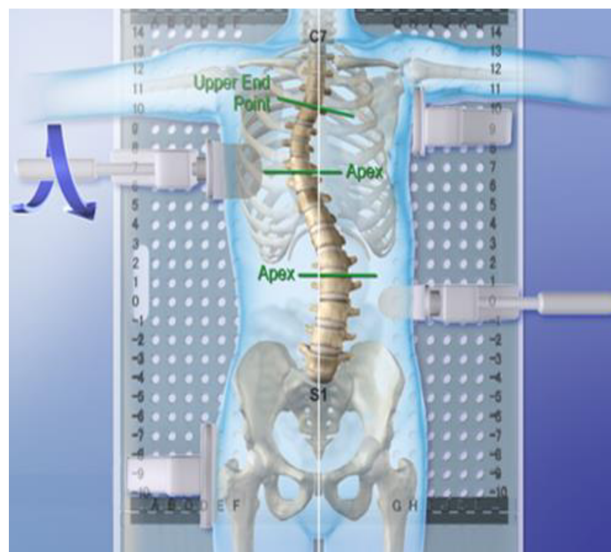
Figure 6 - 6 Providence brace casting system [150].

All spinal braces in this study were designed by two experience orthotists based on similar design concepts. Patients attended the brace fitting clinic 1 month after the brace casting clinic. During the brace fitting clinic, accessories such as straps, buckles, polyethylene flap for the abdomen region, and foam brace pads were attached on the brace. Patients were fitted with the traditional TLSO or the 3D printed brace. Orthotists made brace adjustments at the fitting clinic for patient to comfortably wear their braces at different postures while

standing, sitting and lying down. Patients were then requested to wear their braces starting with 4-6 hours per day and increasing 3-4 hours per week until full-time brace wear (23 hours per day). In-brace assessment clinic is usually set for 2 months after the brace prescription clinic.

6.1.3. Assessment of Spinal Curve Parameters and Wear Time Compliance

Pre-brace and in-brace PA and lateral radiographs were obtained at the brace prescription and in-brace assessment clinics, respectively. All radiographies were obtained using EOS radiography system (EOS Imaging S.A., Paris, France). The assessed spinal parameters included a) Cobb angle on the coronal plane, b) AVR at the apical vertebra based on the Stokes' method on the transverse plane, c) the kyphotic angle between T1 to T12 based on the Cobb method on the sagittal plane, and d) the lordotic angle between L1 to S1 based on the Cobb method on the sagittal plane. MIAS was used to measure the assessed parameters. A trained rater with 2 years of experience measured the radiographs. The trained rater measured the Cobb angle of all curves once and compared only the Cobb angle of spinal curves in which the orthotist intended to treat (treated curves) with clinical records. The same rater also measured the apical AVR, kyphotic and lordotic angles twice with three days apart to minimize memory bias and to determine the rater measurement reliability. Apical AVR of all spinal curves were measured, but only the apical AVR of the treated curves were reported. In-brace corrections of Cobb angle and apical AVR were calculated as a percent difference from pre-brace and in-brace measurements. In-brace kyphosis and lordosis angles of the patients in degrees were also reported. Lastly, the self-reported average wear time per day of full time brace wear was recorded 4-6 weeks after brace fitting clinic.

6.1.4. Evaluation of Manufacturing Process Parameters

Manufacturing time, cost, and design parameters of the traditional TLSO (Figure 6 - 7a) were compared with those of the 3D printed brace (Figure 6 - 7b). More specifically, manufacturing time was divided into casting & fitting time, labour time, and machine time. Casting & fitting time are the clinic time where both patient and orthotist are involved in the manufacturing process. Casting time is when the orthotist obtained patient body contour for the brace design. Fitting time is when the orthotist fits the brace on the patient for the

first time and makes adjustment accordingly to maximize comfort. Labour time is the manufacturing time where the orthotist and supporting technicians required to create the brace. Machine time includes the set up and the automated manufacturing time of using either the carving or the 3D printing machine. Cost analysis included material and labour costs of a brace. Lastly, the brace design parameters include thickness, and weight ratio. Weight ratio between the Nylon12 (W_N) brace versus the polypropylene (W_{pp}) brace was calculated assuming a rectangular volume for a plastic sheet, it was calculated with the following formula:

$$\frac{W_N}{W_{pp}} = \frac{m_N \cdot g}{m_{pp} \cdot g} = \frac{\rho_N}{\rho_{pp}} \cdot \frac{t_N}{t_{pp}} \cdot \frac{H_N \cdot L_N}{H_{pp} \cdot L_{pp}}$$

[6 - 2]

Derive from density formula, where W is weight, m is mass, g is gravity, ρ is density, t is thickness of plastic sheet, H is height of plastic sheet, L is length of plastic sheet and the subscript N represents Nylon12 brace and the subscript pp represents polypropylene brace.

(a)   **(b)**
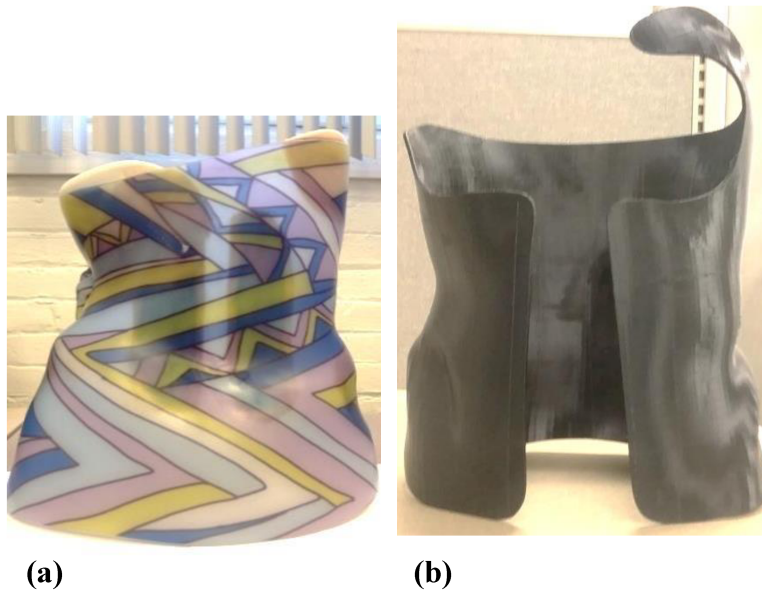
Figure 6 - 7 Scoliosis brace. (a) Traditional TLSO. (b) 3D printed brace.

6.2. Preliminary Results of RCT Study and Manufacturing Process Evaluation

6.2.1. Pre-Brace Patient Demographics and Spinal Curve Characteristics

Table 6 - 2 summarizes the preliminary results of current study which includes the pre-brace patient demographics such as age, height, weight, and Risser grade. As well, treatment information such as assigned brace group, treated curves, and lateral radiographs acquired were reported. As reported in Table 6 - 2, four patients who met the inclusion criteria participated in the study. Two patients were randomly assigned to 3D printed brace intervention group (P1, P4) and two patients were randomly assigned to traditional brace control group (P2, P3). A total of 9 spinal curves were identified, but only 6 were treated curves. That's because the other curves were either at the upper thoracic region unable to be treated with TLSO design or it was a secondary curve with a comparably smaller magnitude. Also, one recruited patient (P3) did not have a pre-brace lateral radiograph. Three of the braces were designed by one experienced orthotist (P1, P3, P4), and one brace designed by another experienced orthotist (P2). All patients report in Table 6 - 2 are female. Figure 6 - 8 shows patient 1 wearing a 3D printed brace at the brace fitting clinic.

Table 6 - 2 Pre-brace patient demographics and treatment information

Patient ID	Age (years)	Height (cm)	Weight (kg)	Risser grade	Assigned brace group	Treated curves
P1	12.2	147.1	34.6	0	3D printed	2
P2	12.8	161.7	49.4	2	Traditional	1
P3	12.6	150.6	44.9	1	Traditional	1
P4	11.4	144.9	43.5	0	3D printed	2
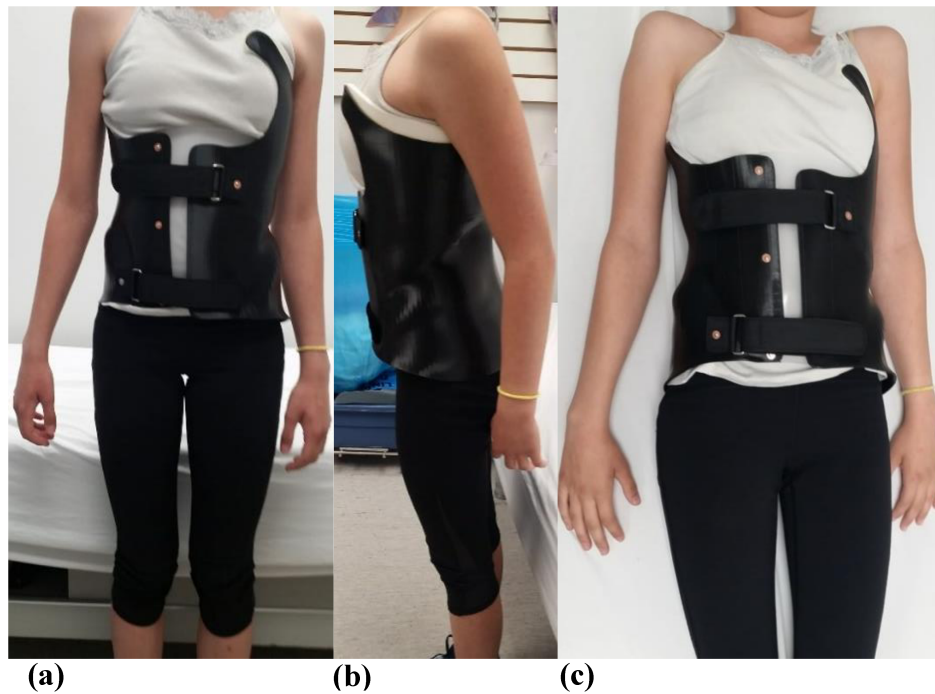
Figure 6 - 8 3D printed brace fitting of patient 1 at the clinic. (a) Standing frontal view. (b) Standing side view. (c) Supine frontal view.

Table 6 - 3 illustrates the pre-brace spinal characteristics of patients. Treated curves were included and an upper thoracic curve for patient 3. Even though the orthotist was unable to treat the upper thoracic curve of patient 3, the patient was included because of a smaller secondary curve in the main thoracic region. All patients had over 100% estimate maximum curve correction (EMCC) indicating overcorrection and flexible spinal curves. T1/T12 kyphosis of patients were within normal value of 20-40 degrees [151]. L1/S1 lordosis were within normal value of 47-67 degrees for 10-12 years age group [152]. The reliability of rater measurements of the treated curve was determined by comparison with clinic database radiographic measurements or with repeated measurements. The maximum deviation between ultrasound and clinic radiographic measurements for standing Cobb angle was 3 degrees. The maximum deviation between the rater's radiographic measurements with clinic measurements for Cobb angle was also 3 degrees which was within the clinical accepted error. The maximum deviation between two measurement sessions of apical AVR, kyphotic angle and lordotic angle were 5 degrees, 6 degrees and 15 degrees respectively. The kyphotic and lordotic angles had more deviation because of

the blurry radiographs at T1 and S1 vertebrae. Rater reliability in ultrasound and radiographic measurements reached acceptable deviation of 3 degrees for Cobb angle measurements and 5 degrees for AVR measurements.

Table 6 - 3 Pre-brace spinal characteristics of patients

Patient ID	Curve type	Number of vertebrae within the curve	Estimate maximum curve correction (%)	Cobb angle (°)
P1	R, MT	7	118	29
	L, L	5	134	30
P2	R, MT	8	192	30
P3	L, UT	5	N/A	24
	R, MT	9	210	16
P4	R, MT	6	N/A	28
	L, L	5		20
Patient ID	Apical AVR (°)	T1/T12 Kyphosis (°)	L1/S1 Lordosis (°)	
P1	4	29	53	
	-7			
P2	-7	23	55	
P3	3	N/A	N/A	
	2			
P4	7	34	59	
	-4			

N/A: Information not available

6.2.2. In-Brace Corrections of Treated Curves and Wear Time Compliance

The in-brace spinal parameters for the treated curves are summarized in Table 6 - 4. For traditional TLSO group, patient 2 had an excellent Cobb angle correction close to 100% and patient 3 had a lower Cobb angle correction. Both patients had flexible spinal curve with over 100% estimate maximum curve correction shown in Table 6 - 3. However, patient 3 had a smaller pre-brace curve magnitude compared with patient 2. For the 3D printed brace group, the Cobb angle correction for 3 out of 4 treated curves reached clinically aimed threshold of 50%. Any small in-brace AVR overcorrection or correction are considered good. In-brace kyphosis and lordosis remained the same or decrease from pre-brace measurements. All in-brace T1/T12 kyphosis of patients were within normal value of 20-40 degrees [151]. All in-brace L1/S1 lordosis were within normal value of 47-67 degrees for 10-12 years age group [152] except for patient 3.

Table 6 - 4 In-brace spinal parameters of treated curves for traditional TLSO and 3D printed brace groups

Patient ID	Brace type	Cobb angle correction (%)	Apical AVR correction (%)	In-brace T1/T12 Kyphosis (º)	In-brace L1/S1 Lordosis (º)
P2	Traditional TLSO	91	13	23	41
P3		34	-200	35	71
P1	3D printed TLSO	54	82	24	53
		57	111		
P4		39	113	25	57
		50	-26		

All patients were prescribed with 23 hours of full time brace wear. The self-reported average wear time/day before in-brace radiographic assessment clinic are recorded in Table 6 - 5. The wear time compliance of 3D printed brace patients were similar or better than the average 67% wear time compliance from previous multicenter RCT study of traditional TLSO (116 patients) [8]. The casting pressure at different pad regions are also reported on Table 6 - 5. Lumbar pad pressure for patient 1 and trochanter pad pressure for patient 2 were not available due to component malfunction at the time.

Table 6 - 5 Self-reported wear time and brace pad casting pressures of patients

Patient ID	Brace type	Wear time/ day (hrs)	Wear time/ day (%)	Axilla pressure (mmHg)	Thoracic pressure (mmHg)	Lumbar pressure (mmHg)	Trochanter pressure (mmHg)
P2	Traditional	16	70%	8	45	110	N/A
P3	TLSO	N/A	N/A	39	53	96	18
P1	3D printed	23	100%	66	50	N/A	20
P4	TLSO	14	61%	41	57	94	26

N/A Information not available or applicable

6.2.3. Manufacturing Time, Cost and Brace Design Parameters

The estimate brace manufacturing time for traditional TLSO and 3D printed braces in this RCT is summarized in Table 6 - 6 from researcher and orthotist inputs. Initially, the 3D printed brace casting time took longer time, but the casting time was shortened with adjustments of the casting frame as well as improvement of 3D scanning techniques. This results in similar casting/fitting time of about an hour for both traditional TLSO and 3D printed brace. Labour time for traditional TLSO was 4.5 hours compared with 1 hour for the latest 3D printed brace (P4). Machine time for brace manufacturing depends on patient body size. The average machine time for traditional TLSO was 0.75 hours compared to 40.1 hours for 3D printed brace. The average total brace manufacturing times for traditional TLSO and 3D printed brace were 6.0 hours and 42.4 hours, respectively.

Each patient participated in the study undergone the 3D printed brace casting process regardless of test group assigned for reducing manufacturing time by identifying and fixing unexpected challenges as well as improving manufacturing techniques with practice. Also, each patient had a traditional TLSO made regardless of test group assigned for creating a backup brace in case 3D printed brace manufactured was not suitable.

Table 6 - 6 Brace manufacturing time of traditional TLSO and 3D printed braces of clinical study

	Traditional TLSO		3D printed brace		
	Components	Time (hrs)	Components	Time (hrs)	
		P2, P3		P1	P4
Casting & fitting time	1. Casting time: Generate body cast with traditional providence system	0.5	1. Casting time: Generate body shape file with custom brace frame and 3D scanner	1.25	0.75
	2. Follow-up fitting clinic for brace adjustment	0.25	2. Follow-up fitting clinic for brace adjustment	0.25	0.25
	Subtotal	0.75	Subtotal	1.5	1.0
Labour time	1. 3D scanning body mold	0.5	1. 3D model modification	0.75	0.75
	2. 3D model modification	0.5	2. Surface finish, addition of accessories	0.25	0.25
	3. Thermoform and trim brace, addition of accessories	3.5			
	Subtotal	4.5		1.0	1.0
Machine time	1. Set up carver machine	0.75	1. Set up print setting	0.5	0.25
	2. Craving positive mold		2. 3D printing brace	38.8	40.7
	Subtotal	0.75	Subtotal	39.3	40.9
Total time		6.0	Total time	41.8	42.9

N/A represents not applicable items

The design parameters and cost of traditional TLSO and 3D printed brace are reported in Table 6 - 7. 3D printed braces were about 30% thinner and 26% lighter when compared with traditional TLSO. However, 3D printed brace material cost was two times higher and direct cost 27% higher than traditional TLSO. The direct cost was higher as it was printed by a company while the traditional TLSO was manufactured in-house.

Table 6 - 7 Design parameters and cost of traditional TLSO and 3D printed brace

Design parameter and cost		Traditional TLSO	3D printed brace
Thickness (mm)		4.5	3.0
Weight ratio		1	0.74
Cost (CAD)	Material Cost	100	200
	Direct Cost (Material and labour)	1100	1400

6.3. Limitations of Study

Initially, the new manufacturing process intended to have a few ultrasound scans between the brace pad adjustments during the casting clinic to guide orthotist in optimal placement and applied force of pads on patient. However, only ultrasound scans for measuring spinal flexibility were obtained due to limited clinic time with longer than expected 3D scanning time at the beginning.

Another limitation is that the in-brace correction to predict the brace effectiveness was assessed 4-6 weeks after brace fitting clinic. However, a 2 year follow up study after weaning of the brace is necessary to verify the final treatment outcome of a 3D printed brace. Furthermore, the Cobb angle correction of the scoliotic curve depends on factors other than the brace type used. A larger sample size of patients with different characteristics are necessary for making a conclusive statement on the effectiveness of 3D printed brace.

6.4. Challenges with Initial 3D Printed Brace Manufacturing

One of the challenges included the need for extensive training and practice to scan the patient torso within the brace casting frame. The scanning process for the first 3D printed brace patient took too long due to difficulty in avoiding the casting frame structure while scanning. The patient reported dizziness due to prolong standing. This concern was addressed with significant reduction in 3D scan and brace pad adjustment time after improvement in scanning and frame adjustment techniques for the last 3D printed brace patient. Following the first 3D printed brace patient, patients were also instructed to move their feet slightly to improve blood circulation and to take breaks as needed. The scanned torso for the last 3D printed brace patient had adequate scan quality. However, the axilla

region was missed during the scan, which resulted in scanning of patient mold for 3D printing.

Another challenge was orthotist buy-in with using the new custom brace modification software lacking traditional modification tools. This resulted in additional time required for orthotist in learning the new software modification tools. Due to time constraint, the last 3D printed brace was modified using a combination of traditional and new brace modification software. Additional training and new software updates on brace modification toolbox are expected to reduce modification time and improve orthotist acceptance. Lastly, the 3D printed braces exceeded manufacturer's printer height and they were reduced in height to fit the build volume. This was due to unexpected additional of top flap as shown in Figure 6 - 7 (b) compared to the traditional brace shown in Figure 6 - 7 (a). The top flap was added for patient with scoliotic curve at the thoracic region. The decrease of 3D printed brace height leads to reduction of the life of the brace with rapid growth of adolescent.

6.5. Conclusions

In conclusion, the in-brace Cobb angle correction for 3 out of 4 treated curves of the 3D printed brace group met clinical aimed threshold of 50%. Furthermore, in-brace apical AVR correction or overcorrection were found for 3 out of 4 treated curves in the 3D printed brace group. In-brace T1/T12 kyphosis and L1/S1 lordosis had minimal change. These are promising results for predicting that 3D printed brace effectiveness might be equivalent or better than traditional TLSO. However, a larger sample size of patients and a 2 year follow up study after weaning are needed to make a conclusive statement on the effectiveness of 3D printed brace compared with traditional TLSO treatment.

3D printed brace was found to be about 30% thinner and 26% lighter weight than traditional TLSO. Also, labour time was reduced 4.5 times compared to traditional TLSO. However, 3D printed brace required significantly longer machine time. Also, 3D printed brace material cost was two times higher and direct cost 27% higher than traditional TLSO. That's because the 3D printed brace was printed by a company rather than created in-house as the traditional TLSO.

Chapter 7: Conclusions and Recommendations

In this final chapter, the major findings from the investigation of the 3D printed brace manufacturing process and 3D printed brace effectiveness are highlighted in section 7.1, while future works in expanding the current study are recommended in section 7.2.

7.1. Conclusions

The hypothesis of the overall research project was that scoliosis patients wearing a 3D printed brace would have better treatment outcome than a traditional TLSO. That was because a 3D printed brace could be created thinner, more lightweight, and with varying thicknesses at different brace sections. Therefore, full time brace wear would be more comfortable for scoliosis patients which would improve wear time compliance and treatment effectiveness. Furthermore, the new brace manufacturing process using a 3D scanner to obtain patient body contour would require less manufacturing steps, less labour-intensive and reduce cost.

Through comparison of different 3D printing methods, FDM printing method was recommended for printing a brace. To investigate the appropriate material and thickness for a 3D printed brace, mechanical testing of specimens and evaluation of 3D printed prototype braces were conducted. It was found that Nylon12, 2.5-3.25mm as the appropriate material and thickness for a 3D printed brace.

The final dynamic brace pads design for pressure measurements during brace casting process had minimal leakage and met design specifications. The brace casting frame for simulating in-brace body shape with optimal curve correction also met design specifications after testing on a healthy volunteer before implementation at the clinic.

To evaluate whether a 3D scanned torso has adequate accuracy and precision for creating a brace that is clinically acceptable, 3D scanned torso mold measurements were compared with motion capture camera measurements. It was found that accuracy and precision of 3D scanned torso were within clinically accepted range. After that, torso molds were scanned inside the brace casting frame with pad applied to evaluate the reconstruction accuracy of 3D scanned torso pad covered regions. It was found that reconstruction accuracy at pad covered regions exceeded clinical accepted range and required additional software

modifications from the orthotist. A new 3D printed brace casting and manufacturing process was designed. It involved optimal brace pad placement on patient torso which was guided by real time ultrasound and pressure measurements inside a custom brace casting frame, 3D scanning in-frame body contour, software modification of brace shape, 3D printing, manual adjustment at brace fitting clinic and 3D radiographic assessment of in-brace corrections.

A randomized controlled trial was started to investigate the effectiveness of 3D printed brace compared to the traditional TLSO. The in-brace corrections in the coronal, transverse and sagittal plane were examined. Preliminary results of four patients with two patients in each arm showed that the coronal plane Cobb angle correction reached clinical aimed threshold for 3 out of 4 treated curves. In-brace apical AVR for 3 out of 4 treated curves showed correction or overcorrection for the intervention group. Minimal changes were found for kyphotic and lordotic angle in brace. Kyphotic and lordotic angles were within normal range in brace.

3D printed braces were found to be 30% thinner and 26% lighter than traditional TLSO. As well, labour time required was reduced 4.5 times. However, the direct cost including material and labour cost were 40% higher for the 3D printed brace due to manufacturing from a commercial 3D printing company. 3D printed brace direct cost could be reduced significantly with the set up of a lower cost in-house 3D printer. Another challenge with 3D printed brace manufacturing was the long machine time compared to traditional TLSO. This could be justified with 3D printer running continuously with minimal labour requirement and the optimization of printing parameters in reducing machine time.

7.2. Future Work Recommendations

A recommended future work of this research project includes investigating whether pattern cut outs on a 3D printed brace will improve breathability compared with the traditional TLSO. This can be evaluated by examining the effective thermal conductivity of 3D printed brace with pattern cut outs and traditional TLSO at different brace regions. Another future work will be improving the current dynamic brace pad design for ease of manufacturing. Another recommended future work will be correlating the final casting

pressures with spinal flexibility of patient and curve magnitude while brace pads are applied. Subgroup analysis of correlation based on curve type can also be included when a larger sample size is obtained. Understanding the correlation might help orthotist in applying optimal casting pressure on patient without multiple brace pad adjustments during casting process. Another suggested future work will be varying 3D printed brace region thickness for further weight reduction based on stress-distribution of brace during donning and doffing from finite element models. In addition, brace shell thickness at pad regions can be increased with a deformable printed material to reinforce pressure regions and replace the need for attaching the current foam pads. After that, the treatment outcome of variable thickness 3D printed brace can be compared with the uniformed thickness 3D printed brace. Also, it is suggested to design a machine for systematically testing the donning and doffing of a 3D printed brace for validating the structural integrity of each customized 3D printed brace with varying brace thickness and geometry. In the future, the randomized controlled trial clinical study should be continued with larger number of test subjects for determining the final treatment outcome of 3D printed brace compared with traditional TLSO with 2 years follow-up of patients after weaning of the brace. Lastly, Nylon12 material before printing is known to have high moisture absorption. Investigation on whether there is any long-term strength loss with moisture absorption of Nylon12 printed brace can be conducted.

References

[1] S. L. Weinstein, L. A. Dolan, J. C. Y. Cheng, A. Danielsson, and J. A. Morcuende, "Adolescent idiopathic scoliosis," *Lancet Lond. Engl.*, vol. 371, no. 9623, pp. 1527–1537, May 2008.

[2] M. Neuwirth and K. Osborn, *The Scoliosis Handbook*. Henry Holt and Company, Inc., 1996.

[3] M. A. Asher and D. C. Burton, "Adolescent idiopathic scoliosis: natural history and long term treatment effects," *Scoliosis*, vol. 1, no. 1, Dec. 2006.

[4] R. D. Rao and M. Smuck, *Orthopaedic Knowledge Update: Spine 4*, 4th ed. American Academy of Orthopaedic Surgeons, 2012.

[5] J. W. Wiley, J. D. Thomson, T. M. Mitchell, B. G. Smith, and J. V. Banta, "Effectiveness of the boston brace in treatment of large curves in adolescent idiopathic scoliosis," *Spine*, vol. 25, no. 18, pp. 2326–2332, Sep. 2000.

[6] E. Ascani *et al.*, "Natural history of untreated idiopathic scoliosis after skeletal maturity," *Spine*, vol. 11, no. 8, pp. 784–789, Oct. 1986.

[7] M. R. Konieczny, H. Senyurt, and R. Krauspe, "Epidemiology of adolescent idiopathic scoliosis," *J. Child. Orthop.*, vol. 7, no. 1, pp. 3–9, Feb. 2013.

[8] S. L. Weinstein, L. A. Dolan, J. G. Wright, and M. B. Dobbs, "Effects of Bracing in Adolescents with Idiopathic Scoliosis," *N. Engl. J. Med.*, vol. 369, no. 16, pp. 1512–1521, Oct. 2013.

[9] B. S. Richards, R. M. Bernstein, C. R. D'Amato, and G. H. Thompson, "Standardization of criteria for adolescent idiopathic scoliosis brace studies: SRS Committee on Bracing and Nonoperative Management," *Spine*, vol. 30, no. 18, pp. 2068–2075, 2005.

[10] E. Lou, D. Hill, J. Raso, and T. B. Grivas, "Brace Treatment for Adolescent Idiopathic Scoliosis," in *The Conservative Scoliosis Treatment: 1st SOSORT Instructional Course Lectures Book*, vol. Section VIII Braces, 2008, pp. 265–273.

[11] K.-J. Tan, M. M. Moe, R. Vaithinathan, and H.-K. Wong, "Curve progression in idiopathic scoliosis: follow-up study to skeletal maturity," *Spine*, vol. 34, no. 7, pp. 697–700, Apr. 2009.

[12] M. S. Wong, A. F. T. Mak, K. D. K. Luk, J. H. Evans, and B. Brown, "Effectiveness and biomechanics of spinal orthoses in the treatment of adolescent idiopathic scoliosis (AIS)," *Prosthet. Orthot. Int.*, vol. 24, no. 2, pp. 148–162, Aug. 2000.

[13] E. H. M. Lou, D. L. Hill, J. V. Raso, M. Moreau, and D. Hedden, "How quantity and quality of brace wear affect the brace treatment outcomes for AIS," *Eur. Spine J.*, vol. 25, no. 2, pp. 495–499, Feb. 2016.

[14] A. Chan, E. Lou, and D. Hill, "Review of current technologies and methods supplementing brace treatment in adolescent idiopathic scoliosis," *J. Child. Orthop.*, vol. 7, no. 4, pp. 309–316, Oct. 2013.

[15] M. S. Wong, J. C. Y. Cheng, M. W. Wong, and S. F. So, "A work study of the CAD/CAM method and conventional manual method in the fabrication of spinal orthoses for patients with adolescent idiopathic scoliosis," *Prosthet. Orthot. Int.*, vol. 29, no. 1, pp. 93–104, Apr. 2005.

[16] T. Vrtovec, F. Pernuš, and B. Likar, "A review of methods for quantitative evaluation of axial vertebral rotation," *Eur. Spine J.*, vol. 18, no. 8, pp. 1079–1090, Aug. 2009.

[17] "Revised Glossary of Terms | Scoliosis Research Society." [Online]. Available: http://www.srs.org/professionals/online-education-and-resources/glossary/revised-glossary-of-terms. [Accessed: 06-Mar-2018].

[18] M. C. Cassella and J. E. Hall, "Current Treatment Approaches in the Nonoperative and Operative Management of Adolescent Idiopathic Scoliosis," *Phys. Ther.*, vol. 71, no. 12, pp. 897–909, Dec. 1991.

[19] E. J. Riseborough and J. H. Herndon, *Scoliosis and Other Deformities of the Axial Skeleton*. 1975.

[20] H. Kim *et al.*, "Scoliosis Imaging: What Radiologists Should Know," *RadioGraphics*, vol. 30, no. 7, pp. 1823–1842, Nov. 2010.

[21] A. Moreau *et al.*, "Melatonin signaling dysfunction in adolescent idiopathic scoliosis," *Spine*, vol. 29, no. 16, pp. 1772–1781, Aug. 2004.

[22] C. A. Wise, X. Gao, S. Shoemaker, D. Gordon, and J. A. Herring, "Understanding Genetic Factors in Idiopathic Scoliosis, a Complex Disease of Childhood," *Curr. Genomics*, vol. 9, no. 1, pp. 51–59, Mar. 2008.

[23] N. Ramirez, C. E. I. Johnston, and R. H. Browne, "The Prevalence of Back Pain in Children Who Have Idiopathic Scoliosis*," *JBJS*, vol. 79, no. 3, p. 364, Mar. 1997.

[24] "Scoliosis | Scoliosis Research Society." [Online]. Available: http://www.srs.org/patients-and-families/conditions-and-treatments/parents/scoliosis. [Accessed: 07-Mar-2018].

[25] J. Van Goethem, A. Van Campenhout, L. van den Hauwe, and P. M. Parizel, "Scoliosis," *Neuroimaging Clin. N. Am.*, vol. 17, no. 1, pp. 105–115, Feb. 2007.

[26] L. G. Lenke *et al.*, "Curve prevalence of a new classification of operative adolescent idiopathic scoliosis: does classification correlate with treatment?," *Spine*, vol. 27, no. 6, pp. 604–611, Mar. 2002.

[27] M. A. Asher and D. C. Burton, "Adolescent idiopathic scoliosis: natural history and long term treatment effects," *Scoliosis*, vol. 1, p. 2, Mar. 2006.

[28] W. P. Bunnell, "Selective screening for scoliosis," *Clin. Orthop.*, no. 434, pp. 40–45, May 2005.

[29] "Position Statements | Scoliosis Research Society." [Online]. Available: http://www.srs.org/about-srs/quality-and-safety/position-statements. [Accessed: 08-Mar-2018].

[30] G. C. Lam, D. L. Hill, L. H. Le, J. V. Raso, and E. H. Lou, "Vertebral rotation measurement: a summary and comparison of common radiographic and CT methods," *Scoliosis*, vol. 3, p. 16, Nov. 2008.

[31] I. A. Stokes, L. C. Bigalow, and M. S. Moreland, "Measurement of axial rotation of vertebrae in scoliosis," *Spine*, vol. 11, no. 3, pp. 213–218, Apr. 1986.

[32] S. Deschênes *et al.*, "Diagnostic imaging of spinal deformities: reducing patients radiation dose with a new slot-scanning X-ray imager," *Spine*, vol. 35, no. 9, pp. 989–994, Apr. 2010.

[33] C. J. Adam, M. T. Izatt, and G. N. Askin, "Design and evaluation of an MRI compatible axial compression device for 3D assessment of spinal deformity and flexibility," in *Faculty of Built Environment and Engineering; Institute of Health and Biomedical Innovation; School of Engineering Systems*, Christchurch Convention Centre, Christchurch, 2010.

[34] R. Zheng *et al.*, "Improvement on the Accuracy and Reliability of Ultrasound Coronal Curvature Measurement on Adolescent Idiopathic Scoliosis With the Aid of Previous Radiographs," *Spine*, vol. 41, no. 5, pp. 404–411, Mar. 2016.

[35] C.-W. J. Cheung and Y. Zheng, "Development of 3-D Ultrasound System for Assessment of Adolescent Idiopathic Scoliosis (AIS)," in *6th World Congress of Biomechanics (WCB 2010). August 1-6, 2010 Singapore*, Springer, Berlin, Heidelberg, 2010, pp. 584–587.

[36] T. Ungi *et al.*, "Spinal curvature measurement by tracked ultrasound snapshots," *Ultrasound Med. Biol.*, vol. 40, no. 2, pp. 447–454, Feb. 2014.

[37] W. Chen, L. H. Le, and E. H. M. Lou, "Reliability of the axial vertebral rotation measurements of adolescent idiopathic scoliosis using the center of lamina method on ultrasound images: in vitro and in vivo study," *Eur. Spine J. Off. Publ. Eur. Spine Soc. Eur. Spinal Deform. Soc. Eur. Sect. Cerv. Spine Res. Soc.*, vol. 25, no. 10, pp. 3265–3273, 2016.

[38] S. L. Weinstein and I. V. Ponseti, "Curve progression in idiopathic scoliosis," *J. Bone Joint Surg. Am.*, vol. 65, no. 4, pp. 447–455, Apr. 1983.

[39] M. Rigo, S. Negrini, H. Weiss, T. Grivas, T. Maruyama, and T. Kotwicki, "'SOSORT consensus paper on brace action: TLSO biomechanics of correction (investigating the rationale for force vector selection),'" *Scoliosis*, vol. 1, p. 11, 2006.

[40] M. D. Rigo, M. Villagrasa, and D. Gallo, "A specific scoliosis classification correlating with brace treatment: description and reliability," *Scoliosis*, vol. 5, p. 1, Jan. 2010.

[41] I. a. F. Stokes, "Mechanical effects on skeletal growth," *J. Musculoskelet. Neuronal Interact.*, vol. 2, no. 3, pp. 277–280, Mar. 2002.

[42] I. A. F. Stokes, "Heuter-Volkmann effect: State of the Art Reviews," in *Spine 14*, 2000, pp. 349–357.

[43] R. Roaf, "Vertebral growth and its mechanical control," *J. Bone Joint Surg. Br.*, vol. 42-B, pp. 40–59, Feb. 1960.

[44] T. B. Grivas, "Biomechanical and Clinical Perspectives on Nighttime Bracing for Adolescent Idiopathic Scoliosis," in *The Conservative Scoliosis Treatment: 1st*

SOSORT Instructional Course Lectures Book, vol. Section VIII Braces, 2008, pp. 274–290.

[45] S. L. Weinstein, *The Pediatric Spine: Principle and Practice*. 2001.

[46] F. Zaina *et al.*, "Bracing for scoliosis in 2014: state of the art," *Eur. J. Phys. Rehabil. Med.*, vol. 50, no. 1, pp. 93–110, Feb. 2014.

[47] T. Kotwicki and J. Cheneau, "Biomechanical action of a corrective brace on thoracic idiopathic scoliosis: Cheneau 2000 orthosis," *Disabil. Rehabil. Assist. Technol.*, vol. 3, no. 3, pp. 146–153, Jan. 2008.

[48] M. Rigo and H.-R. Weiss, "The Chêneau concept of bracing--biomechanical aspects," *Stud. Health Technol. Inform.*, vol. 135, pp. 303–319, 2008.

[49] T. Grivas, "European Braces for Conservative Scoliosis Treatment," in *Human Musculoskeletal Biomechanics*, T. Goswami, Ed. InTech, 2012.

[50] J. C. de Mauroy, C. Lecante, and F. Barral, "'Brace Technology' Thematic Series - The Lyon approach to the conservative treatment of scoliosis," *Scoliosis*, vol. 6, p. 4, 2011.

[51] J. C. de Mauroy, A. Journe, F. Gagaliano, C. Lecante, F. Barral, and S. Pourret, "The new Lyon ARTbrace versus the historical Lyon brace: a prospective case series of 148 consecutive scoliosis with short time results after 1 year compared with a historical retrospective case series of 100 consecutive scoliosis; SOSORT award 2015 winner," *Scoliosis*, vol. 10, p. 26, 2015.

[52] J. C. de Mauroy, *Reference Manual for the ARTbrace*. Lecante Group, 2016.

[53] K. Zaborowska-Sapeta, I. M. Kowalski, T. Kotwicki, H. Protasiewicz-Fałdowska, and W. Kiebzak, "Effectiveness of Chêneau brace treatment for idiopathic scoliosis: prospective study in 79 patients followed to skeletal maturity," *Scoliosis*, vol. 6, p. 2, Jan. 2011.

[54] H.-R. Weiss, M. Werkmann, and C. Stephan, "Correction effects of the ScoliOlogiC® „Chêneau light" brace in patients with scoliosis," *Scoliosis*, vol. 2, p. 2, Jan. 2007.

[55] H. Berdishevsky *et al.*, "Physiotherapy scoliosis-specific exercises - a comprehensive review of seven major schools," *Scoliosis Spinal Disord.*, vol. 11, p. 20, 2016.

[56] J. B. Emans, A. Kaelin, P. Bancel, J. E. Hall, and M. E. Miller, "The Boston bracing system for idiopathic scoliosis. Follow-up results in 295 patients," *Spine*, vol. 11, no. 8, pp. 792–801, Oct. 1986.

[57] H. Labelle, J. Dansereau, C. Bellefleur, and B. Poitras, "Three-dimensional effect of the Boston brace on the thoracic spine and rib cage," *Spine*, vol. 21, no. 1, pp. 59–64, Jan. 1996.

[58] J. Clin, C.-E. Aubin, S. Parent, and H. Labelle, "A biomechanical study of the Charleston brace for the treatment of scoliosis," *Spine*, vol. 35, no. 19, pp. E940-947, Sep. 2010.

[59] J. Galante, A. Schultz, R. L. Dewald, and R. D. Ray, "Forces Acting in the Milwaukee Brace on Patients Undergoing Treatment for Idiopathic Scoliosis," *J Bone Jt. Surg Am*, vol. 52, no. 3, pp. 498–506, Apr. 1970.

[60] J. E. Lonstein and B. G. Smith, *Milwaukee Brace Treatment of Scoliosis: SRS Bracing Manual*. 2003.

[61] M. S. Wong and J. H. Evans, "Biomechanical evaluation of the Milwaukee brace," *Prosthet. Orthot. Int.*, vol. 22, no. 1, pp. 54–67, Apr. 1998.

[62] C. d'Amato and B. McCoy, *The Providence Scoliosis System Manaul: SRS Bracing Manual*. 2003.

[63] C. H. Rivard, *SpineCor System: SRS Bracing Manual*. 2002.

[64] "CPO, Inc. » Providence Scoliosis TLSO." [Online]. Available: http://cpo.biz/providence-tlso/. [Accessed: 12-Mar-2018].

[65] M. S. Wong, J. T. C. Lee, K. D. K. Luk, and L. C. K. Chan, "Effect of different casting methods on adolescent idiopathic scoliosis," *Prosthet. Orthot. Int.*, vol. 27, no. 2, pp. 121–131, Aug. 2003.

[66] E. H. Lou, A. C. Chan, A. Donauer, M. Tilburn, and D. L. Hill, "Ultrasound-assisted brace casting for adolescent idiopathic scoliosis, IRSSD Best research paper 2014," *Scoliosis*, vol. 10, p. 13, Apr. 2015.

[67] E. H. Lou, D. L. Hill, A. Donauer, M. Tilburn, D. Hedden, and M. Moreau, "Results of ultrasound-assisted brace casting for adolescent idiopathic scoliosis," *Scoliosis Spinal Disord.*, vol. 12, no. 1, p. 23, Dec. 2017.

[68] R. S. Fayssoux, R. H. Cho, and M. J. Herman, "A History of Bracing for Idiopathic Scoliosis in North America," *Clin. Orthop.*, vol. 468, no. 3, pp. 654–664, Mar. 2010.

[69] H. Eldeeb, S. Asfour, and N. Boubekri, "CT/MR imaging: a design tool for custom orthosis," *Disabil. Rehabil.*, vol. 22, no. 13–14, pp. 583–590, Sep. 2000.

[70] D. Perie, J. S. De Gauzy, and M. C. Hobatho, "Biomechanical evaluation of Cheneau-Toulouse-Munster brace in the treatment of scoliosis using optimisation approach and finite element method," *Med. Biol. Eng. Comput.*, vol. 40, no. 3, pp. 296–301, 2002.

[71] T. B. Grivas *et al.*, "Brace Classification Study Group (BCSG): part one – definitions and atlas," *Scoliosis Spinal Disord.*, vol. 11, no. 1, Dec. 2016.

[72] L. W. van Rhijn, C. M. T. Plasmans, and B. E. E. M. J. Veraart, "Changes in curve pattern after brace treatment for idiopathic scoliosis," *Acta Orthop. Scand.*, vol. 73, no. 3, pp. 277–281, Jun. 2002.

[73] C. J. Goldberg, D. P. Moore, E. E. Fogarty, and F. E. Dowling, "Adolescent idiopathic scoliosis: the effect of brace treatment on the incidence of surgery," *Spine*, vol. 26, no. 1, pp. 42–47, Jan. 2001.

[74] A. J. Danielsson, R. Hasserius, A. Ohlin, and A. L. Nachemson, "A prospective study of brace treatment versus observation alone in adolescent idiopathic scoliosis: a follow-up mean of 16 years after maturity," *Spine*, vol. 32, no. 20, pp. 2198–2207, Sep. 2007.

[75] D. E. Rowe, S. M. Bernstein, M. F. Riddick, F. Adler, J. B. Emans, and D. Gardner-Bonneau, "A meta-analysis of the efficacy of non-operative treatments for idiopathic scoliosis," *J. Bone Joint Surg. Am.*, vol. 79, no. 5, pp. 664–674, May 1997.

[76] D. G. Little, K. M. Song, D. Katz, and J. A. Herring, "Relationship of peak height velocity to other maturity indicators in idiopathic scoliosis in girls," *J. Bone Joint Surg. Am.*, vol. 82, no. 5, pp. 685–693, May 2000.

[77] F. Canavese and A. Kaelin, "Adolescent idiopathic scoliosis: Indications and efficacy of nonoperative treatment," *Indian J. Orthop.*, vol. 45, no. 1, p. 7, Jan. 2011.

[78] R. Havey *et al.*, "A reliable and accurate method for measuring orthosis wearing time," *Spine*, vol. 27, no. 2, pp. 211–214, Jan. 2002.

[79] G. Nicholson and M. Ferguson-Pell, "Development of Instrumented spinal Brace for measuring compliance and skin microclimate in the conservative treatment of adolescent idiopathic scoliosis," 2001.

[80] H. Jiang, "Interface Pressures in the Boston Brace Treatment for Scoliosis," 1992.

[81] E. Lou, J. V. Raso, D. L. Hill, J. K. Mahood, and M. J. Moreau, "Correlation between quantity and quality of orthosis wear and treatment outcomes in adolescent idiopathic scoliosis," *Prosthet. Orthot. Int.*, vol. 28, no. 1, pp. 49–54, Apr. 2004.

[82] E. Lou, J. V. Raso, D. L. Hill, N. G. Durdle, J. K. Mahood, and M. J. Moreau, "The daily force pattern of spinal orthoses in subjects with adolescent idiopathic scoliosis," *Prosthet. Orthot. Int.*, vol. 26, no. 1, pp. 58–63, Apr. 2002.

[83] E. Lou, D. L. Hill, J. V. Raso, M. J. Moreau, and J. K. Mahood, "Smart orthosis for the treatment of adolescent idiopathic scoliosis," *Med. Biol. Eng. Comput.*, vol. 43, no. 6, pp. 746–750.

[84] T. Rahman, J. R. Bowen, M. Takemitsu, and C. Scott, "The association between brace compliance and outcome for patients with idiopathic scoliosis," *J. Pediatr. Orthop.*, vol. 25, no. 4, pp. 420–422, Aug. 2005.

[85] T. Yrjönen, M. Ylikoski, D. Schlenzka, R. Kinnunen, and M. Poussa, "Effectiveness of the Providence nighttime bracing in adolescent idiopathic scoliosis: a comparative study of 36 female patients," *Eur. Spine J.*, vol. 15, no. 7, pp. 1139–1143, Jul. 2006.

[86] "SRS Bracing Manual | Scoliosis Research Society." [Online]. Available: http://www.srs.org/professionals/online-education-and-resources/srs-bracing-manual. [Accessed: 16-Mar-2018].

[87] J. C. de Mauroy, C. Lecante, F. Barral, and S. Pourret, "Prospective study and new concepts based on scoliosis detorsion of the first 225 early in-brace radiological results with the new Lyon brace: ARTbrace," *Scoliosis*, vol. 9, p. 19, 2014.

[88] S. Negrini, G. Marchini, and F. Tessadri, "Brace technology thematic series - The Sforzesco and Sibilla braces, and the SPoRT (Symmetric, Patient oriented, Rigid, Three-dimensional, active) concept," *Scoliosis*, vol. 6, p. 8, 2011.

[89] J.-C. Bernard, C. Lecante, J. Deceuninck, G. Notin, L. Journoud, and F. Barral, "The carbon brace," *Scoliosis*, vol. 8, p. 3, 2013.

[90] "UNYQ-Align^{TM}-Product-Sheet." [Online]. Available: http://unyq.com/wp-content/uploads/2016/10/UNYQ-Align%E2%84%A2-Product-Sheet.pdf. [Accessed: 12-Nov-2016].

[91] J.-P. Kruth, M. C. Leu, and T. Nakagawa, "Progress in Additive Manufacturing and Rapid Prototyping," *CIRP Ann. - Manuf. Technol.*, vol. 47, no. 2, pp. 525–540, Jan. 1998.

[92] K. V. Wong and A. Hernandez, "A Review of Additive Manufacturing," *ISRN Mech. Eng.*, vol. 2012, pp. 1–10, 2012.

[93] R. Hague, S. Mansour, N. Saleh, and R. Harris, "Materials analysis of stereolithography resins for use in Rapid Manufacturing," *J. Mater. Sci.*, vol. 39, no. 7, pp. 2457–2464, Apr. 2004.

[94] H.-C. Kim and S.-H. Lee, "Reduction of post-processing for stereolithography systems by fabrication-direction optimization," *Comput.-Aided Des.*, vol. 37, no. 7, pp. 711–725, Jun. 2005.

[95] F. Rengier *et al.*, "3D printing based on imaging data: review of medical applications," *Int. J. Comput. Assist. Radiol. Surg.*, vol. 5, no. 4, pp. 335–341, Jul. 2010.

[96] S. Ahn, M. Montero, D. Odell, S. Roundy, and P. K. Wright, "Anisotropic material properties of fused deposition modeling ABS," *Rapid Prototyp. J.*, vol. 8, no. 4, pp. 248–257, Oct. 2002.

[97] Lindsey Bass, Nicholas Alexander Meisel, and Christopher B. Williams, "Exploring variability of orientation and aging effects in material properties of multi-material jetting parts," *Rapid Prototyp. J.*, vol. 22, no. 5, pp. 826–834, Aug. 2016.

[98] D. L. Bourell, T. J. Watt, D. K. Leigh, and B. Fulcher, "Performance Limitations in Polymer Laser Sintering," *Phys. Procedia*, vol. 56, pp. 147–156, 2014.

[99] I. Gibson and D. Shi, "Material properties and fabrication parameters in selective laser sintering process," *Rapid Prototyp. J.*, vol. 3, no. 4, pp. 129–136, Dec. 1997.

[100] B. Jackson, "Stuck on SLA 3D Printing? New research holds promise for big area additive manufacturing," *3D Printing Industry*. [Online]. Available: https://3dprintingindustry.com/news/stuck-sla-3d-printing-new-research-holds-promise-big-area-additive-manufacturing-106606/. [Accessed: 22-Jun-2017].

[101] 3D korbot, *Korbot 3D printer FDM #2.* .

[102] AdditiveTechnologies, *3D Printing - PolyJet - Additive Technologies.* .

[103] "SLS 3D Printing," *Obsessively Geek.* [Online]. Available: http://www.og3dprinting.com/sls/. [Accessed: 13-Jul-2018].

[104] ytec3d, *Plan B overview, Open source 3DP printer.* .

[105] W. Cooke, R. A. Tomlinson, R. Burguete, D. Johns, and G. Vanard, "Anisotropy, homogeneity and ageing in an SLS polymer," *Rapid Prototyp. J.*, vol. 17, no. 4, pp. 269–279, Jun. 2011.

[106] C. L. Ventola, "Medical Applications for 3D Printing: Current and Projected Uses," *Pharm. Ther.*, vol. 39, no. 10, pp. 704–711, Oct. 2014.

[107] S. Bose, S. Vahabzadeh, and A. Bandyopadhyay, "Bone tissue engineering using 3D printing," *Mater. Today*, vol. 16, no. 12, pp. 496–504, Dec. 2013.

[108] I. D. Ursan, L. Chiu, and A. Pierce, "Three-dimensional drug printing: A structured review," *J. Am. Pharm. Assoc.*, vol. 53, no. 2, pp. 136–144, Mar. 2013.

[109] G. T. Klein, Y. Lu, and M. Y. Wang, "3D Printing and Neurosurgery—Ready for Prime Time?," *World Neurosurg.*, vol. 80, no. 3, pp. 233–235, Sep. 2013.

[110] J. Banks, "Adding Value in Additive Manufacturing : Researchers in the United Kingdom and Europe Look to 3D Printing for Customization," *IEEE Pulse*, vol. 4, no. 6, pp. 22–26, Nov. 2013.

[111] C. Mavroidis *et al.*, "Patient specific ankle-foot orthoses using rapid prototyping," *J. NeuroEngineering Rehabil.*, vol. 8, p. 1, 2011.

[112] C. E. Dombroski, M. E. Balsdon, and A. Froats, "The use of a low cost 3D scanning and printing tool in the manufacture of custom-made foot orthoses: a preliminary study," *BMC Res. Notes*, vol. 7, p. 443, Jul. 2014.

[113] "UNYQ Showcases 3D Printed Scoliosis Brace with Embedded Wearable Technology at White House Event Celebrating Inclusive Design, Assistive Technology & Prosthetics | Business Wire." [Online]. Available: https://www.businesswire.com/news/home/20160915006398/en/UNYQ-Showcases-3D-Printed-Scoliosis-Brace-Embedded. [Accessed: 18-Sep-2018].

[114] R. Kuiper, "A Finite Element Method Approach to Brace Treatment for Scoliotic Spine," Delft University of Technology, 2017.

[115] C. Scott, "Dr. Lelio Leoncini and WASPmedical Create Better Spinal Care Through 3D Printing," *3DPrint.com | The Voice of 3D Printing / Additive Manufacturing*, 11-Nov-2016. .

[116] J. Cottalorda, R. Kohler, C. Garin, P. Genevois, C. Lecante, and B. Berge, "Orthoses for Mild Scoliosis: A Prospective Study Comparing Traditional Plaster Mold Manufacturing With Fast, Noncontact, 3-dimensional Acquisition," *Spine*, vol. 30, no. 4, pp. 399–405, Feb. 2005.

[117] F. Blais, "Review of 20 years of range sensor development," *J. Electron. Imaging*, vol. 13, no. 1, pp. 231–244, Jan. 2004.

[118] Z. Zhang, "Microsoft Kinect Sensor and Its Effect," *IEEE Multimed.*, vol. 19, no. 2, pp. 4–10, Feb. 2012.

[119] K. Khoshelham and S. O. Elberink, "Accuracy and Resolution of Kinect Depth Data for Indoor Mapping Applications," *Sensors*, vol. 12, no. 2, pp. 1437–1454, Feb. 2012.

[120] H. Mousavi Hondori and M. Khademi, "A Review on Technical and Clinical Impact of Microsoft Kinect on Physical Therapy and Rehabilitation," *J. Med. Eng.*, vol. 2014, pp. 1–16, 2014.

[121] "Structure Sensor - Rodin4D." [Online]. Available: http://rodin4d.com/en/Products/acquisition/structure-sensor. [Accessed: 26-Sep-2017].

[122] C. A. A. Beaumont *et al.*, "Three-dimensional surface scanners compared with standard anthropometric measurements for head shape," *J. Cranio-Maxillofac. Surg.*, vol. 45, no. 6, pp. 921–927, Jun. 2017.

[123] "Precise 3D vision for embedded applications - Uses - Structure Sensor." [Online]. Available: https://structure.io/embedded. [Accessed: 06-Apr-2018].

[124] "Uses for Structure Sensor." [Online]. Available: https://structure.io/uses. [Accessed: 06-Apr-2018].

[125] R. M. Sabiston, J. D. Chang, and C. Saunders, "Method and system for generating a three-dimensional scan of an object," US20160331278A1, 17-Nov-2016.

[126] "3D Handheld Spectra[TM] Scanner - Vorum." .

[127] "Buy Xbox One with Kinect Bundle - Microsoft Store en-CA," *Microsoft Store*. [Online]. Available: https://www.microsoft.com/en-ca/store/d/xbox-one-with-kinect-bundle/92cxftggvl5x. [Accessed: 04-Apr-2018].

[128] A. Dai, A. X. Chang, M. Savva, M. Halber, T. Funkhouser, and M. NieBner, "ScanNet: Richly-Annotated 3D Reconstructions of Indoor Scenes," 2017, pp. 2432–2443.

[129] "Buy Structure Sensor - Give your iPad 3D Vision." [Online]. Available: https://store.structure.io/store. [Accessed: 06-Apr-2018].

[130] "Tech specs | 3D Systems." [Online]. Available: https://www.3dsystems.com/materials/visijet-pxl/tech-specs?_ga=2.191980716.762823391.1537313442-635638337.1537313442. [Accessed: 18-Sep-2018].

[131] "How Much Do 3D Printer Materials Cost in 2018?," *All3DP*, 03-Oct-2018. [Online]. Available: https://all3dp.com/2/how-much-do-3d-printer-materials-cost/. [Accessed: 10-Nov-2018].

[132] A. Graves, L. A. M. Engineer, and S. D. Manufacturing, "Stereolithography vs. PolyJet: Photopolymer 3D Printing Materials & Applications," *Research & Development*, 24-Feb-2016. [Online]. Available: https://www.rdmag.com/article/2016/02/stereolithography-vs-polyjet-photopolymer-3d-printing-materials-applications. [Accessed: 10-Nov-2018].

[133] "ULTEM 1010 Material Data Sheet." Stratasys, 23-Apr-2018.

[134] "ASTM D638-14: Standard Test Method for Tensile Properties of Plastics." ASTM International, 2014.

[135] "Materials for 3D Printing | Stratasys." [Online]. Available: http://www.stratasys.com/materials/search?properties=5f9a756c493541f69a5260ac41fea595&sortIndex=0. [Accessed: 18-Apr-2018].

[136] "International Standard ISO 527-1: Plastics- Determination of tensile properties." International Standard (ISO), 2012.

[137] D. Roylance, "STRESS-STRAIN CURVES." Department of Materials Science and Engineering Massachusetts Institute of Technology, 2001.

[138] H. Jiang and J. V. Raso, "Interface pressures in the boston brace treatment for scoliosis," *Proc. Intl Symp. 3- Scoliotic Deform.*, 1992.

[139] T. L. Starr, T. J. Gornet, and J. S. Usher, "The effect of process conditions on mechanical properties of laser-sintered nylon," *Rapid Prototyp. J.*, vol. 17, no. 6, pp. 418–423, Oct. 2011.

[140] G. W. Melenka, J. S. Schofield, M. R. Dawson, and J. P. Carey, "Evaluation of dimensional accuracy and material properties of the MakerBot 3D desktop printer," *Rapid Prototyp. J.*, vol. 21, no. 5, pp. 618–627, Aug. 2015.

[141] J. W. Roach, "ADOLESCENT IDIOPATHIC SCOLIOSIS," *Orthop. Clin. North Am.*, vol. 30, no. 3, pp. 353–365, Jul. 1999.

[142] F. Landauer, C. Wimmer, and H. Behensky, "Estimating the final outcome of brace treatment for idiopathic thoracic scoliosis at 6-month follow-up," *Pediatr. Rehabil.*, vol. 6, no. 3–4, pp. 201–207, Dec. 2003.

[143] S. Negrini *et al.*, "2011 SOSORT guidelines: Orthopaedic and Rehabilitation treatment of idiopathic scoliosis during growth," *Scoliosis*, vol. 7, p. 3, 2012.

[144] "Growth Charts - Data Table of Stature-for-age Charts." [Online]. Available: https://www.cdc.gov/growthcharts/html_charts/statage.htm. [Accessed: 01-Aug-2018].

[145] "Home | CONNECTING IMAGING TO CARE | EOS imaging." [Online]. Available: http://www.eos-imaging.com/us. [Accessed: 24-Apr-2018].

[146] "F900 & F900 PRO 3D Printers for Large Build Manufacturing | Stratasys." [Online]. Available: http://www.stratasys.com/3d-printers/stratasys-f900. [Accessed: 25-Oct-2018].

[147] "Adolescent Idiopathic Scoliosis | Scoliosis Research Society." [Online]. Available: https://www.srs.org/professionals/online-education-and-resources/conditions-and-treatments/adolescent-idiopathic-scoliosis. [Accessed: 17-Oct-2018].

[148] R. Zheng *et al.*, "Assessment of Curve Flexibility on Scoliotic Surgical Candidates Using Ultrasound Imaging Method," *Ultrasound Med. Biol.*, vol. 43, no. 5, pp. 934–942, 2017.

[149] M. Khodaei, D. Hill, R. Zheng, L. H. Le, and E. H. M. Lou, "Intra- and inter-rater reliability of spinal flexibility measurements using ultrasonic (US) images for non-surgical candidates with adolescent idiopathic scoliosis: a pilot study," *Eur. Spine J. Off. Publ. Eur. Spine Soc. Eur. Spinal Deform. Soc. Eur. Sect. Cerv. Spine Res. Soc.*, vol. 27, no. 9, pp. 2156–2164, Sep. 2018.

[150] "The Providence Nocturnal Scoliosis System," *Spinal Technology Inc. .*

[151] G. Fon, M. Pitt, and A. Thies, "Thoracic kyphosis: range in normal subjects," *Am. J. Roentgenol.*, vol. 134, no. 5, pp. 979–983, May 1980.

[152] A. Cil *et al.*, "The Evolution of Sagittal Segmental Alignment of the Spine During Childhood:," *Spine*, vol. 30, no. 1, pp. 93–100, Jan. 2005.

[153] D. Page, A. Koschan, S. Voisin, N. Ali, and M. Abidi, "3D CAD model generation of mechanical parts using coded-pattern projection and laser triangulation systems," *Assem. Autom.*, vol. 25, pp. 230–238, Sep. 2005.

[154] M. A.-B. EBRAHIM, "3D Laser Scanners' Techniques Overview," vol. 4, no. 10, p. 9, 2013.

[155] W. E. Lorensen and H. E. Cline, "Marching Cubes: A High Resolution 3D Surface Construction Algorithm," in *Proceedings of the 14th Annual Conference on Computer Graphics and Interactive Techniques*, New York, NY, USA, 1987, pp. 163–169.

Appendix A

A.1. Classification of Technologies for 3D Contour Acquisition

There are various technologies for acquiring 3D surface contour. Classification of different 3D data acquisition technologies are shown in Figure A - 1. Contact method such as coordinate measuring machine (CMM) is often used in manufacturing setting. It has better accuracy than image based systems, however CMM has low scan speed with path planning for probe placement required [153]. Furthermore, contact scanning affects body surface geometry. Non-contact methods include passive and active techniques. Active techniques emit radiation or visible light and detect its reflection for measurement or probing of 3D object [153], [154]. Passive techniques do not emit radiation or visible light, but rely on detection of reflected ambient radiation (typically visible light) for 3D object measurement [153], [154]. Stereo vision is an example of passive technique which uses two cameras to capture two slightly different images of the same object. Analysis of the discrepancies between the images of the 3D object generates the depth information of every point of the 3D object similar to human stereoscopic vision [153], [154].

Active techniques include both volumetric and 3D scanner. Examples of volumetric scanner include magnetic resonance imaging (MRI) and ultrasound. However, volumetric scanners are designed for imaging internal features of the body, even though surface contour can also be acquired [155]. Classifications are focused on 3D scanner techniques as shown in Figure A - 1, because many existing 3D body contour acquisition systems are based on 3D scanner techniques. Triangulation, phase difference and time of flight are three main techniques involve for different 3D scanners [117], [153], [154]. Many 3D scanners use a combination of different techniques for 3D surface acquisition [128]. The main 3D scanner types explored are structure light scanner, modulated light scanner and conoscopic holography scanner [117], [153], [154].
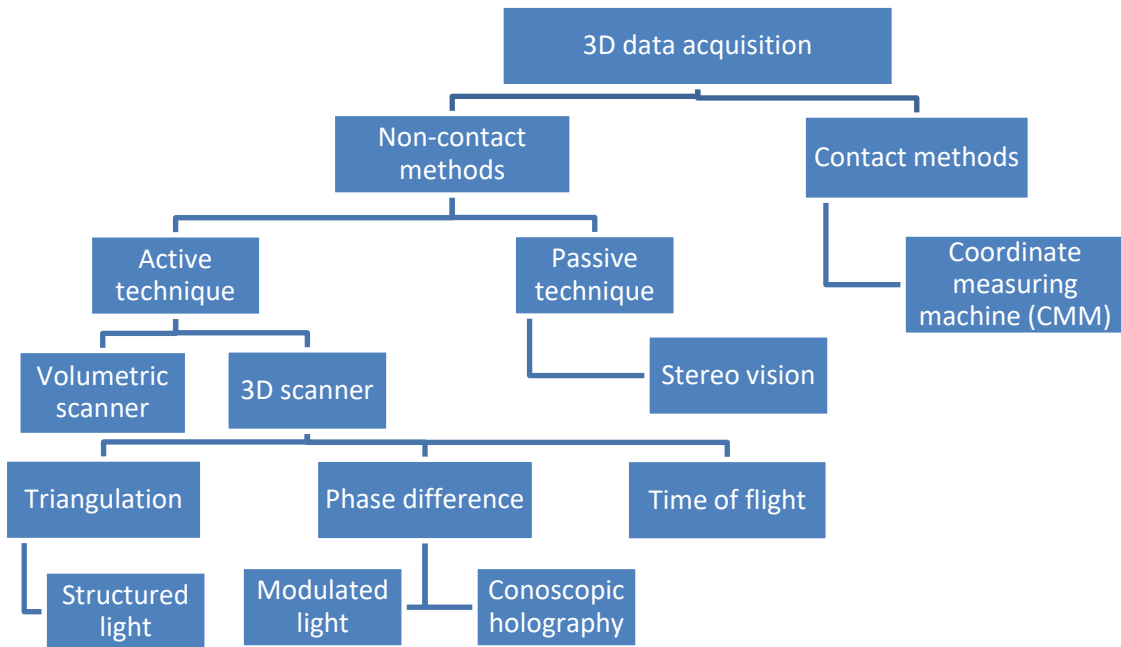
Figure A - 1 Classification of 3D data acquisition technology with specific focus on 3D scanner technologies [153], [154]

A.2. Manufacturing Steps of Dynamic Brace Pads

The following dynamic brace pad manufacturing procedure was developed after testing and evaluating the manufacturing techniques from previous design concepts:

1. 3D printed top ring and pad base with a matte finish using RGD450 with an ObJet30Pro 3D printer, then remove support material with water jet
2. Print out a 1-1 scale drawing of pad base in wireframe and cut out the drawing around the outer edge of cross section
3. Tape the cut-out pad base drawing on the 0.79 mm thick silicon sheet and cut out silicon cover sheet by tracing around drawing closely with an utility knife

(Additional step 5-6 for curved thoracic and lumbar brace pads)

4. Mount top ring and pad base together with #2-56 thread, 0.5 inches long nylon screw and nut around the rim of the pad
5. Heat the clamped top ring and pad base with heat gun and bend to providence brace pad shapes, then remove screws and nuts

6. Apply silicon adhesive with small nozzle and custom spreading fork (Figure 4 - 10(a)) forming a silicon ring around the rim of the pad base at the teeth segment, then take off excess adhesive with a custom glue wipe (Figure 4 - 10 (b))

7. Glue the cut-out of silicon cover sheet on pad base as precisely as possible to avoid additional adjustment and to ensure no opening between the cut-out cover and pad base

8. Apply silicon adhesive as step 7 on the teeth segment of top ring, then apply epoxy with spreading fork around the outer edge of top ring (Figure 4 - 6) as quickly and precisely as possible due to epoxy curing within 5-10 minutes

9. Press down the top ring gently and evenly on the pad base as precisely as possible to avoid position adjustments

10. Add additional silicon adhesive on the inner edge between cover sheet and top ring with a rounded edge object to fill remaining gap

11. Maintain clamping force with clips for curing of glue

12. Clean residual glue by wiping cover sheet with isopropyl alcohol then wait for 24 hours for the silicon glue to cure before test pumping the brace pad